92-10

to Bob Gowan - Keep - publicize?
Chuck
Joss

A Review of Instrumentation Technology for the Minnesota Road Research Project

ROAD
sota Road
rch Project

REPORT DOCUMENTATION PAGE	1. Report No. FHWA/MN/RC - 92/10	2.	3. Recipient's Accession No.

4. Title and Subtitle

A Review of Instrumentation Technology for the Minnesota Road Research Project

5. Report Date: April, 1992

6.

7. Author(s): David A. Van Deusen, Research Assistant, David E. Newcomb, Assistant Professor, Joseph F. Labuz, Assistant Professor

8. Performing Organization Rept. No. 9RD0004

9. Performing Organization Name and Address
University of Minnesota
Dept. of Civil and Mineral Engineering
122 Civil and Mineral Engineering Bldg.
500 Pillsbury Drive S.E.
Minneapolis, MN 55455-0220

10. Project/Task/Work Unit No.

11. Contract(C) or Grant(G) No.
(C) 66063
(G)

12. Sponsoring Organization Name and Address
Minnesota Department of Transportation
Office of Research Administration
117 University 2nd Floor
St. Paul, MN 55155

13. Type of Report & Period Covered
Final Report
1989 - 1992

14.

15. Supplementary Notes

16. Abstract (Limit: 200 words)

This report presents a literature review of instrumentation practices for the measurement of stresses, strains, and deflections in pavement structures. Various types of instruments that are commonly employed in pavement instrumentation projects are discussed, as well as the factors that influence their performance. In a series of laboratory experiments, the performance of three different types of embedment strain gages, two LVDTs, and one soil stress cell are investigated. These experiments are designed to evaluate the accuracy and durability of commercially available transducers. For strain gages, the selection of an appropriate transducer must balance compliance and measurement sensitivity. All of the strain gages tested in concrete gave reasonable results. It was found that hermetically sealed LVDTs should be sufficient enough for robust installations. Experiments with soil stress cells embedded in sand indicate the variability that may be expected in the field due to installation procedures, and emphasize the need for in-soil calibrations. A set of recommendations are provided with respect tot the sensor procurement and installation specifications for Mn/ROAD.

17. Document Analysis a.Descriptors

pavement instrumentation
pavement sensors
stress cells
LVDTs
strain gages
H-gages
embedment gages
pavement response
pavement performance
pavement stress
pavement strain
pavement deflection

b.Identifiers/Open-Ended Terms

18. Availability Statement
No restrictions. This document is available through the National Technical Information Services, Springfield, VA 22161

19. Security Class (This Report) Unclassified

20. Security Class (This Page) Unclassified

21. No. of Pages 140

22. Price

A REVIEW OF INSTRUMENTATION TECHNOLOGY FOR THE MINNESOTA ROAD RESEARCH PROJECT

Final Report

Prepared by

David A. Van Deusen
Research Assistant

David E. Newcomb
Assistant Professor

and

Joseph F. Labuz
Assistant Professor

University of Minnesota
Department of Civil and Mineral Engineering

Submitted to

Research Administration and Development Section
Office of Materials and Research
Minnesota Department of Transportation

April 1992

CONTENTS

LIST OF TABLES

LIST OF FIGURES

LIST OF SYMBOLS

P	Load
H	Height
D	Diameter of stress cell
t	Time, thickness of stress cell or disk
q	Uniform pressure
σ_c	Stress indicated by stress cell, stress acting on disk
σ_s	Soil stress
σ_e	Stress registration error
σ_z	Vertical stress
σ_x, σ_y, σ_h	Horizontal stress
σ_{ij}	Stress
K	Ratio of lateral to vertical stresses
R_s	Soil indentation ratio
N_s	Soil indentation coefficient
τ	Shear stress
δ, u_i	Displacements
ϵ_i, ϵ_s	Strain
E	Young's modulus
G	Shear modulus
ν	Poisson's ratio
ϕ	Soil/steel contact friction angle
β	Angle of inclination

CHAPTER 1
INTRODUCTION

BACKGROUND

The goal of pavement design is to provide a structure capable of carrying the expected traffic loads over a period of time that will resist environmental degradation at the lowest life-cycle cost. Many factors affect the structural design of a pavement; some of these include the number and magnitude of loads, the materials in the pavement layers, the nature of subgrade soils, drainage conditions, the amount and timing of precipitation, and air temperature. A purely empirical approach to pavement design is based upon observations of performance without theoretically reconciling the contributions of various factors. On the other hand, a purely mechanical approach would specifically define the individual factors mathematically concluding in a precise time and mode of failure. Empirical approaches are constrained to the conditions for which they are developed, and any excursion beyond these boundaries may result in gross errors. Analytical and numerical models are usually confined to one specific problem such as responses to load or heat and mass transfer, and combinations of these models to completely explain pavement behavior become intractable. One method of resolving these differences is to construct full-scale, instrumented pavement sections to measure the critical responses and parameters and use these to rationally explain the pavement performance.

The Minnesota Department of Transportation is currently constructing the Minnesota Road Research Project (Mn/ROAD). Mn/ROAD is an unique endeavor in the field of full-scale pavement testing. The three-mile long test facility will be instrumented with nearly 3,000 transducers that will monitor pavement responses due to live traffic loads and environmental conditions. Data collected at Mn/ROAD will be used to evaluate current pavement design techniques and mechanistic models as well as develop new methods for analyzing and designing pavement structures. This research effort will make it possible to observe the changing behavior of each response over short time periods (e.g., seasonal variations) in addition to long-term pavement performance over the course of the design period. Because the success of Mn/ROAD is dependent on the performance of pavement response transducers, it is important to have a sound understanding of the principles of operation of these transducers and their measurement limitations.

OBJECTIVES

The focus of this report is on instrumentation for pavements and is essentially a review of current methodologies. The various transducers employed in pavement instrumentation are discussed, as well as the factors that influence their performance. The overall objectives of this study are to: (1) examine current pavement instrumentation methodologies, (2) procure a limited number of transducers and test them under extreme loading and environmental conditions in the laboratory, and (3) provide a set of final recommendations of which types of transducers would best serve the purposes of Mn/ROAD. Separate sections on strain and displacement measurement and in situ soil stress determination are given. The discussion will be generalized where it is deemed necessary in order to present topics important in instrumentation, yet not directly related to pavements.

SCOPE

The work presented and discussed in this report was prepared for Task Order Contract No. 43 to Agreement No. 64408M, "Assessment of Pavement-Response-Instrumentation." In the early planning stages of Mn/ROAD there was considerable question as to the applicability, durability, and veracity of various types of electronic instrumentation used in the measurement of mechanical and environmental responses in pavement systems. The report reveals some of this information in Chapters 2 through 4 by presenting a literature review of strain, displacement, and pressure instrumentation techniques and how these techniques are applied to pavement systems. Chapter 5 of the report presents results of laboratory experiments that were performed on selected instruments. Chapter 6 is devoted to experimental studies conducted on soil-stress cells. The volume of data generated for this work was significantly greater than the experimental data for strain and displacement data such that a seperate chapter is warranted.

CHAPTER 2
STRAIN MEASUREMENT

Strains within an asphalt concrete or portland cement concrete layer are usually measured by strain gages embedded within the pavement layer. In most mechanistic design procedures the long-term performance of a pavement system (in terms of fatigue durability) is assumed to be related to the strain at a critical point in the system due to a heavy wheel load. The measurement of strains are important because they can be used to verify the assumptions made in mechanistic design procedures.

The following discussion begins with a brief overview of the principles involved with strain gages and strain measurements. Various types of gages are also reviewed. Specific considerations and problems relating to pavement instrumentation are discussed. Finally, several case histories are examined.

PRINCIPLES OF OPERATION

The resistance to electrical current provided by a conductor of uniform cross-section is given by the equation

$$R=\rho\frac{L}{A} \tag{2.1}$$

where R is the resistance in ohms, ρ is the resistivity of the material, and L and A are the length and cross-sectional area of the conductor, respectively. If the conductor is stretched the length will increase and the cross-sectional area will decrease due to the Poisson effect. An expression that relates the initial conductor resistance to changes in resistance is given by

$$\frac{\Delta R}{R_0}=F_G\frac{\Delta L}{L_0} \tag{2.2}$$

The term F_G is commonly referred to as the gage factor, or strain sensitivity factor, and is a function of the alloy characteristics.

TYPES OF STRAIN GAGES

Most strain gages can be placed in one of the following categories: mechanical extensometer, optical, or electrical. Detailed discussions of strain gage types are given by Sebaaly et al. [1] and Dunnicliff [2]. There are basically four different operation mechanisms for electrical strain gages:

1. Unbonded Metallic Filament

This particular style of gage is also called the wire strain gage. Several resistance wires are stretched taut between two supporting insulators. Due to the fragility of these gages they are not commonly used.

2. Bonded Metallic-foil

This is perhaps the most popular variety of strain gage. These types of gages are composed of a strain-sensing alloy grid bonded to a backing material. Although the principle of operation is identical to metallic-filament gages the backing provides several advantages [3]:

- Ease of handling of the gage,
- Better bonding to the specimen material, and
- Electrical insulation between the foil filaments and the test specimen.

3. Piezo-resistive

Piezo-resistive strain gages operate under the same principles as metallic strain gages with the exception that the element is composed of silicon semiconductor material. These types of strain gages will perform under static loading conditions and are more suitable for the measurement of high frequency dynamic strains than are bonded foil strain gages. Piezo-resistive gages possess increased sensitivity; the gage factor for these types of gages are 10 to 50 times greater than metallic-type resistance type gages. Disadvantages are cost, temperature sensitivity, and fragility.

4. Vibrating Wire

These types of strain gages are based on the principle that the frequency of a vibrating wire will change as the wire is stretched or loosened. Vibrating wire strain gages have proven

to be extremely durable in field instrumentation programs [4]. However, they are not suitable for determination of dynamic strains.

Strain gages most suitable for pavement instrumentation are electrical resistance types and are the only ones considered in this discussion.

STRAIN GAGES FOR PAVEMENT LAYERS

Transducers used in pavement instrumentation are usually of the bonded-foil resistance variety. However, most commercially available strain gages are not suitable for immediate installation in a pavement, and must subsequently be modified. Three different methods for preparing an electrical resistance gage for strain measurements in bound layers are discussed and reviewed:

1. H-gages or strip gages,
2. Strain gages adhered to or embedded in carrier blocks prepared in the laboratory, and
3. Strain gages adhered to cores removed from the pavement.

H-gages are composed of a strip of material onto which a metallic-foil strain gage is bonded. Metal bars are attached to the ends of the strip to provide anchorage in the pavement material. These types of transducers may be embedded in both asphalt concrete and portland cement concrete layers. They have commonly been installed at the bottom of asphalt concrete layers to investigate the development of horizontal tensile strains due to heavy wheel loads [5].

An example of an H-gage is shown in Figure 2.1. This particular gage was used to measure horizontal tensile strains in an asphalt pavement during full scale testing at the Nardo Test Site in Nardo, Italy. Elements of this research effort will be discussed in a later section.

An important aspect of transducer design is the relative conformance of the gage with respect to the embedment material. With H-gage configurations the most important consideration is the longitudinal gage stiffness. Ideally, the stiffness of the gage should be similar to that of the material in which it is embedded. If the strip is too stiff it will reinforce the pavement material and the gage will tend to under-register. This may also result in debonding between the anchor bars and surrounding material [5].

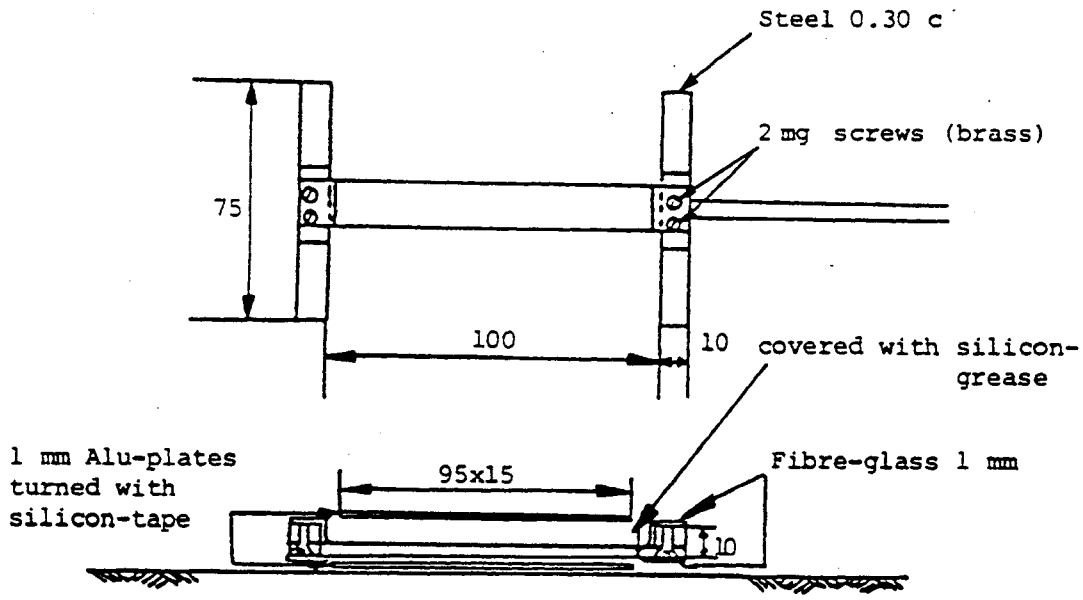

Figure 2.1. Schematic of the H-gage transducer used by the Danish research team at Nardo [5].

The Dynatest PAST series strain gages are a brand of commercially available H-gages (Figure 2.2). These particular embedment gages have been developed by the Technical University of Denmark for the specific purpose of measuring in-situ strains in pavements and as such are capable of enduring extreme environments for extended periods of time. Gages tested in the laboratory under varying adverse conditions have proven very durable [5]. The PAST gage may be installed in any orientation. Details of the construction can be obtained from the manufacturer [6] and are discussed briefly here.

The active transducer is embedded in a fiberglass reinforced epoxy extrusion. This material has a relatively low stiffness, and thus, it does not interfere with, or impose constraints upon, the deformation of the pavement material. The transducer is also protected by a series of coatings and layers. These provide protection from failure due to mechanical and water infiltration effects as well as chemical deterioration. A schematic view of the gage construction is shown in Figure 2.2. Fatigue life of the transducer is estimated at over 10^6 cycles at moderate strain levels. Connections to the transducer are completely sealed and the lead-wires are Teflon insulated. This strain transducer has a grid resistance of 120 Ω, a gage factor of 2.0 , and may

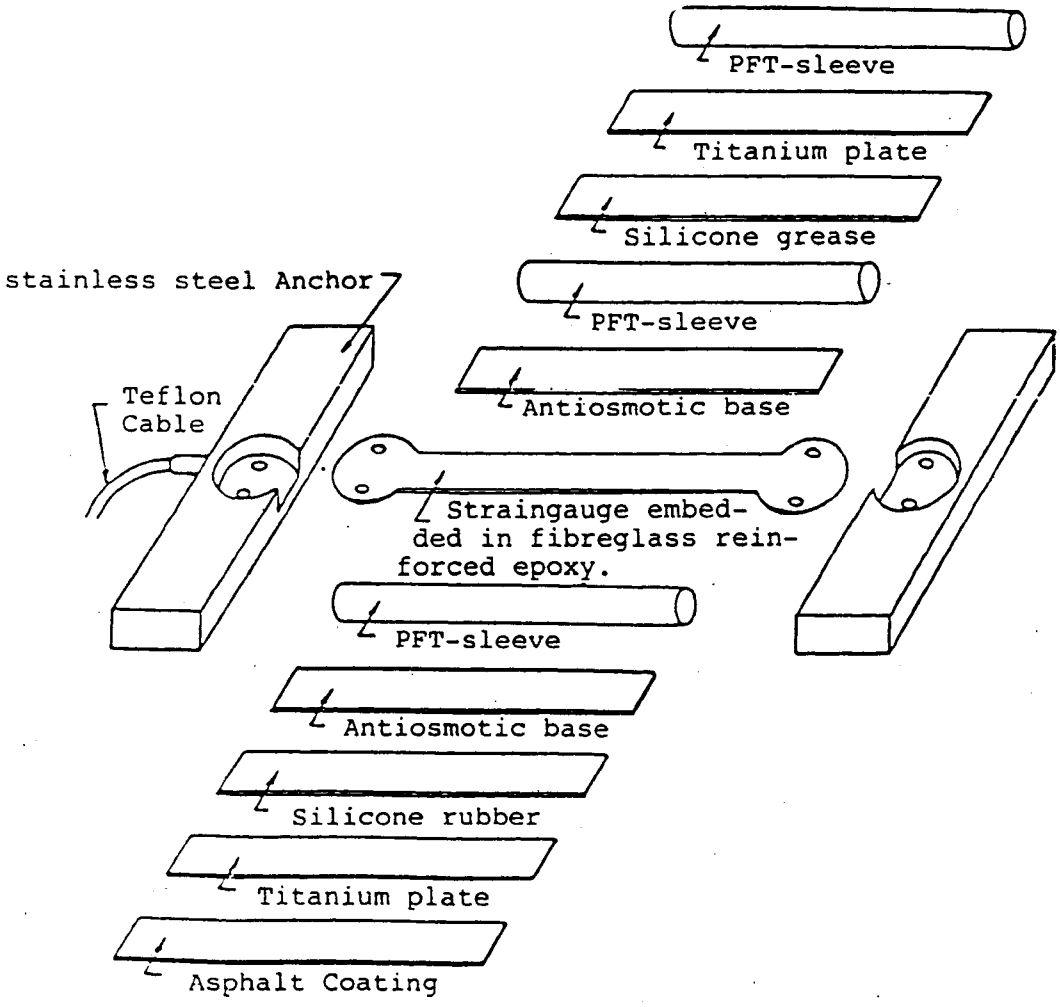

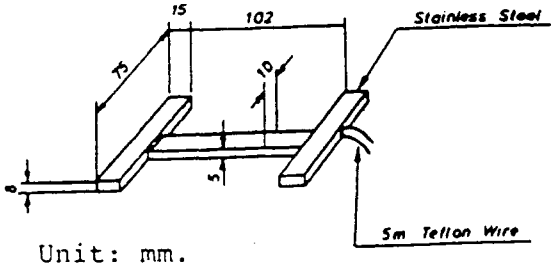

Unit: mm.

Specifications

Type	**PAST-2AC**	**PAST-2PCC**
Range	*up to 1500 µst.*	
Cell-material	*Epoxy - Fibreglass*	
Coating	*Epoxy - Silicone - PFT - Titanium*	
Temperature	*- 30 ~ 150° C*	*-2[illegible] 302° F*
Resistance	*120 Ω ±10%; GF=2,0*	
Exiting Voltage	*up to 12 V (full bridge)*	
ΣE - modulus	*≈ 22000 kp/cm²*	
Sq - area	*≈ 0,5 cm²*	
Fatique - life	*Theoretical up to 10^6 cycles*	
Service - life	*Typical > 36 months*	
Strain force	*≈ 11* $\frac{kp}{1000\ \mu m/m}$	

Figure 2.2. Dynatest PAST 2AC strain transducer [6].

be incorporated into a full bridge setup. Maximum excitation voltage for the gage is 12 VDC. The gage is temperature compensated within the range -22°F to 300°F (-30°C to 150°C).

Various researchers have experimented with strain gage installations in which the transducer is bonded to a material specimen, or the so-called retrofit method. These specimens may either be cores removed from the pavement or laboratory prepared specimens. Examples of both approaches are shown in Figures 2.3 through 2.5. These particular gage designs were

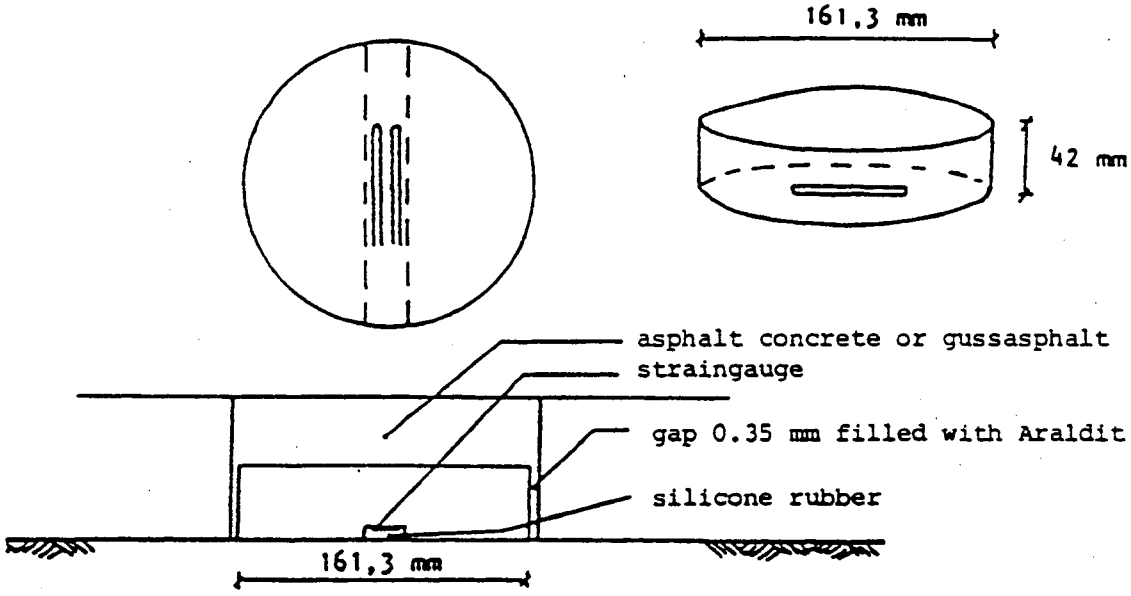

Figure 2.3. Embedment gage configuration utilized by the Finnish research team at Nardo [5].

used by the Finnish, German, and Canadian teams, respectively, at the Nardo Road Test in Italy [5].

The primary type of strain gage configuration used by Finnish researchers is a strain gage bonded to the bottom of a 6-inch diameter by 1-inch thick cylindrical specimen that is prepared in the laboratory. A hole is cored in the pavement for the placement of the finished assembly; the tolerance is reportedly less than 0.04 inches [7]. The cylinder is glued into the hole and the remaining portion is filled with asphalt concrete or gussasphalt. Retrofit or carrier block strain gage configurations may exhibit less stiffness dependent effects than H-gages. This is due to the fact that H-gages have a different temperature-stiffness relationship than retro-fit or carrier block types.

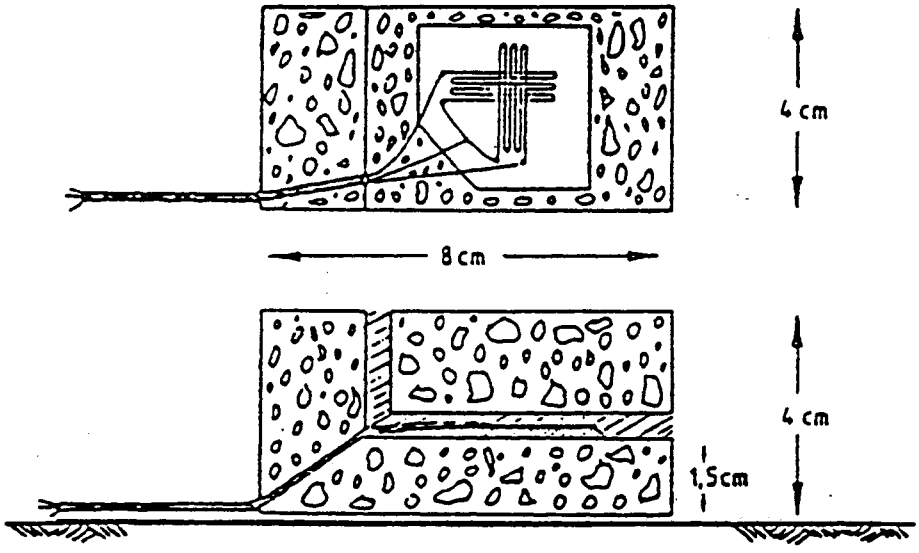

Figure 2.4. Embedment gage configuration utilized by the German research team at Nardo [5].

STRAIN GAGE CIRCUITRY

When a resistance type strain gage is deformed, the change in resistance is very small. The corresponding output change is much too low to be detected in multi-meter circuits. A common means of detecting small resistance changes in strain gage systems is through the Wheatstone bridge (see Figure 2.6) which converts the change in resistance to a voltage change. Bridge excitation voltage is provided by the constant voltage, E. The bridge output e_o is given by

$$e_0 = E\{\frac{R_1}{R_1+R_2} - \frac{R_4}{R_4+R_3}\} \tag{2.3}$$

and depends only on the ratios $R_1/R_2 = R_4/R_3$. The bridge is "balanced" when the output e_0 is zero and the resistance ratios are equal. In Figure 2.7, the resistor R_1 has been replaced by a strain gage having resistance R_G. When the gage is deformed, that particular arm of the bridge changes in resistance and the bridge becomes "unbalanced". Often all four arms of the bridge circuit have the same (nominal) resistance.

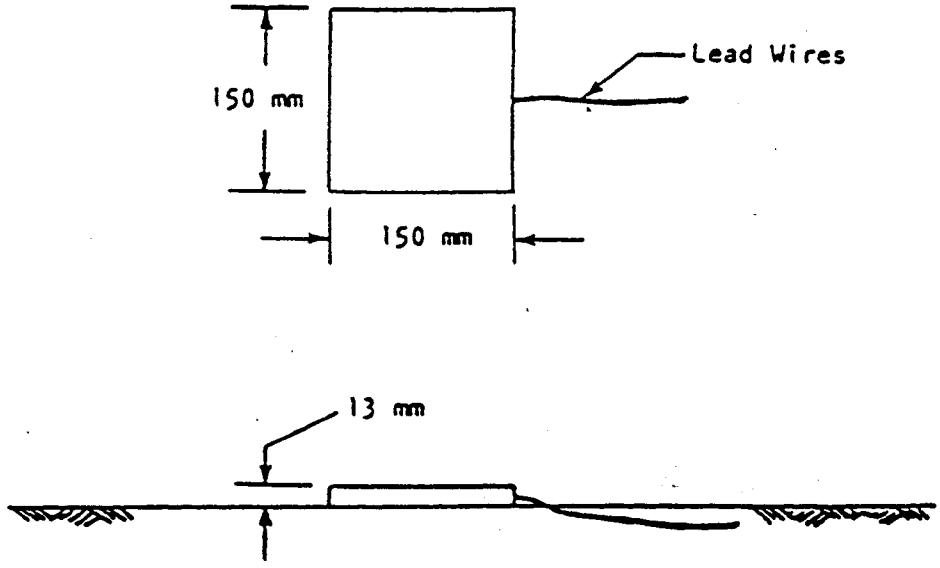

Figure 2.5. Embedment gage configuration utilized by the Canadian research team at Nardo [5].

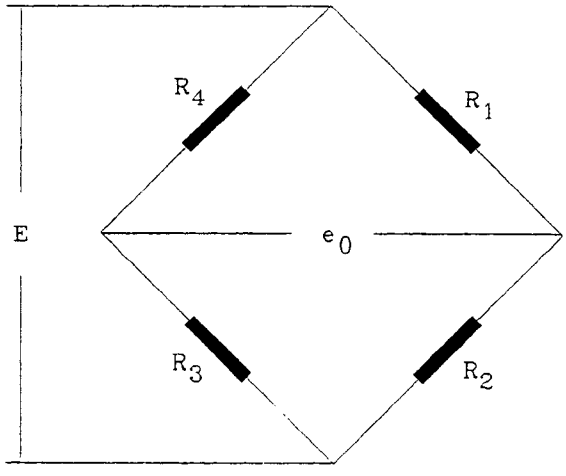

Figure 2.6. Schematic diagram of the basic Wheatstone bridge circuit.

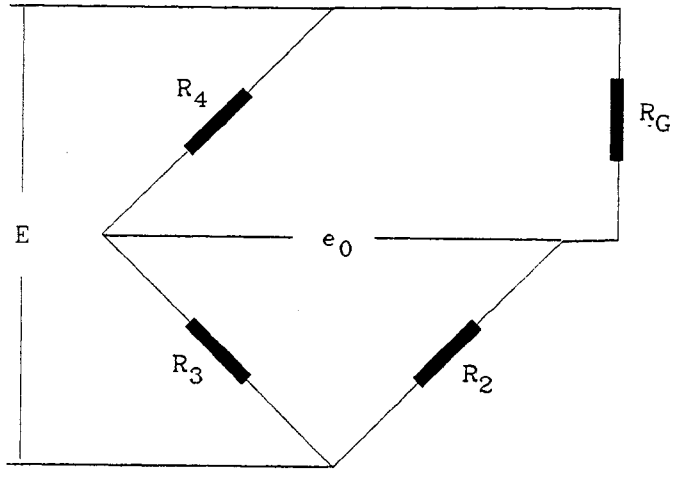

Figure 2.7. Bridge circuit with single active strain gage.

Calibration of a strain gage bridge network is accomplished by performing a shunt calibration. The procedure is relatively simple and involves the simulation of a strain at one or more of the bridge arms to produce a corresponding output, e_0, as shown in Figure 2.8. The shunt resistor, R_c, is connected in parallel with R_1 and the resistance of that arm of the bridge becomes $R_1R_c/(R_1+R_c)$. The change in resistance ΔR is $R_1-R_1R_c/(R_1+R_c)$ or $\Delta R/R_1=-R_1/(R_1+R_c)$. The resistance R_c required to simulate a strain ϵ_s may be computed from the following expression:

$$R_C=\frac{R_G\times 10^6}{F_G\epsilon_S}-R_G \tag{2.4}$$

where R_G, the nominal resistance of the strain gage, has been substituted for the value R_1. It should be noted that the above procedure simulates a down-scale (compressive) strain. Tensile (upscale) strains may be simulated by shunting across an adjacent bridge arm, e.g., R_2.

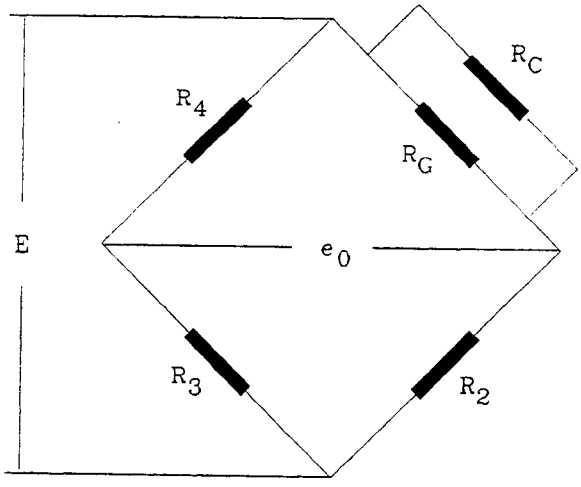

Figure 2.8. Shunt calibration of bridge circuit: single active gage.

Due to inherent non-linearities in the Wheatstone bridge circuit, a strain slightly different than the computed strain will be registered [9]. The error in the simulated tensile strain, in percent, is approximately equal to the gage factor times the strain, in percent. This is due to the fact that in the case of simulated tensile strain a two-fold simulation takes place: a strain simulated in R_2 is being used to interpret the output as due to a tensile strain in R_G. In the case of simulated compressive strain the nonlinearity error is approximately equal to the strain, expressed in percent. The nonlinearity error for simulated strains less than 2,000 $\mu\epsilon$ is negligible [9].

As described above, an excitation voltage is applied across opposite arms of the bridge network. Selection of the proper excitation level is crucial. With regards to the environment found in pavement structures, supplying a large voltage to the bridge circuit can result in increased galvanic corrosion, displacement of metal ions, and changes in the gage resistance [3]. It may also result in a shorter life due to increased power dissipation (in the form of heat) at the gage. An advantage of supplying relatively large excitation voltages is the higher signal-to-noise ratio that results [10]. Complete removal of excitation voltages from the system may increase

gage life. However, this may lead to a lack of accountability for the "zero" strain reading.

Lead-wire desensitization occurs when the lead-wires add a certain amount of resistance to the bridge arm. This can be corrected by adjusting the gage factor during shunt calibration of the circuit. A predetermined strain in the gage is simulated and the bridge balance control adjusted until the readout registers the same strain [9]. When using quarter-bridge arrangements, compensation for temperature effects on the lead wires can be achieved by using the three lead-wire system [2].

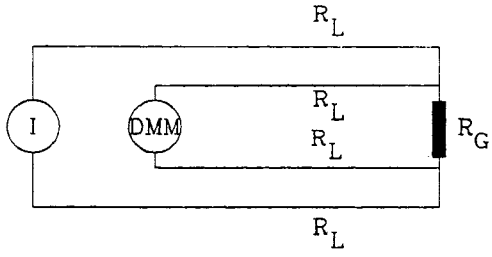

Figure 2.9. Schematic of 4-wire strain gage circuit.

Another method of measuring strains is the 4-wire Ohm method (Figure 2.9). This method enables the measurement of the absolute value of the gage resistance. If a high resolution (e.g. 10^{-3} Ω) digital multi-meter (DMM) is used this can be done very accurately [11]. Gage excitation is provided by means of a constant current source, I. The lead-wire resistances, R_L, do not affect the measurement accuracy since the voltage is read directly across the gage. Low current values may be used so that the power dissipated at the strain gage is low.

STRAIN GAGE SELECTION CRITERIA

A strain gage should be selected for a particular application based upon various factors. The three main factors influencing the general performance of strain gages are [1]: (1) long-term serviceability, (2) accuracy of measurements, and (3) repeatability of the results. Considerations in the selection of a strain gage for pavement instrumentation include the required accuracy and precision, fatigue durability, strain magnitude, gage length, construction survivability, and

environmental stability.

For pavement materials it is commonly believed that the gage length should be at least 4 to 5 times the maximum particle diameter. The strain indicated by a strain gage is the average strain over the length of the gage. Thus, utilizing a gage with a long length may induce unnecessary errors into the measurement. However, in nonhomogeneous materials such as asphalt concrete or portland cement concrete it is the average strain over an area that is usually sought, not local concentrations. Using a large gage has another advantage in that better heat dissipation can be achieved due to the larger gage surface area. This is an important factor in determining the long-term performance of the gage.

A potential strain gage for pavement instrumentation must not only be compliant and sensitive, it must also be durable in order to survive construction, the environment, and repeated heavy axle loads. The most common environmental elements that may cause failure of a strain gage embedded within a pavement structure are puncture due to sharp pieces of aggregate, water infiltration, and chemical reactions [5]. Because current flows through the gage, electrochemical reactions are possible at the grid. This will result in corrosion causing instability in the gage resistance.

Ingression of water may occur along two different paths: through lead-wires, and at the gage itself. The presence of water may have several long-term damaging effects on the gage response such as corrosion of the grid alloy, and swelling of the backing matrix and bonding adhesive [3]. The presence of water cannot be detected simply by measuring the insulation resistance between the grid and specimen. Water filtering through to the gage may be very pure and low in electrical conductivity when it reaches the grid [3]. Also, the backing matrix and bonding adhesive reach complete saturation when the water content reaches 1 to 2 percent, by weight [3]. This is not sufficient to increase electrical conductivity between the gage and specimen. However, such a level of saturation may be sufficient to cause swelling of the material, thereby inducing unwanted strain in the gage. Long-term effects may manifest themselves in the form of an apparent "zero-strain" shift.

INSTALLATION CONSIDERATIONS

The majority of commercially available strain gages are not suitable for direct embedment into pavement materials. As discussed above, there are three common methods for preparing strain transducers for installation in a pavement structure: (1) H-gages, (2) gages bonded to laboratory prepared specimens, and (3) gages bonded to material taken from the pavement. Final installation of the transducer arrangement into the pavement may be completed during construction or retro-fitted. The most common installation location is at the bottom of the AC layer, just above the base course or subgrade. While no source has revealed an ideal installation method, it appears that installation during construction may provide superior conformance over retrofitted gages. The introduction of a gage into the pavement structure disturbs the expected distribution of strains and as such the gage selected for use in a certain application should comply with the material as much as possible. Desirable characteristics are a gage that is rigid enough to provide durability yet flexible enough to deform with the material.

As far as laboratory instrumented carrier blocks are concerned the main issue is the compatibility of the carrier material with the surrounding pavement material. The two should be similar to the degree that a large discontinuity in material properties are not created. Bonding between the carrier block and surrounding material is also important.

With regards to retrofitted core installations there are several problems with conformance. When an instrumented core is reinserted into the pavement it must be bonded to the surrounding material. Bonding the core by whatever means, e.g., epoxy, will influence any measurements due to the fact that a discontinuity is created in the pavement. It is difficult to predict what the relative uncertainty in measurements are when this method is used. Advantages of the retro-fit method of installation are they are not prone to damage during construction, they can be used to replace gages damaged during construction, and can be used to instrument pavements the had not been planned as test sections.

It is necessary to seal the lead-wires at all locations from possible water ingression, e.g., connections at the transducer and signal conditioner. No splices should be made anywhere along the length of the lead-wires. In the specifications for contract, an attempt should be made to procure transducers with factory provided lead-wires long enough to reach from the gage to location of the first connection (e.g. junction box or signal conditioner). It may also be wise

to place all lead-wires within flexible conduit to protect them during construction.

STRAIN GAGE INSTRUMENTATION OF FLEXIBLE PAVEMENTS

Field Tests (T.H. 36)

The Minnesota Department of Transportation (Mn/DOT) has installed three Dynatest PAST 2AC strain transducers in the pavement of Trunk Highway 36 near Lake Elmo, Minnesota. The pavement is a full-depth bituminous section approximately 10 inches thick and is situated on a sand subgrade. The gages are located under the first lift of asphalt and were installed during construction in the summer of 1987. One of the gages was placed directly beneath the anticipated wheel path while the others were placed one foot to either side. This arrangement was utilized in an attempt to perform a load location analysis based on simultaneous strain readings from each gage.

In September, 1989, data were collected from one of the transducers at the site. A Measurements Group P 350-A strain indicator was used and bridge output was monitored using

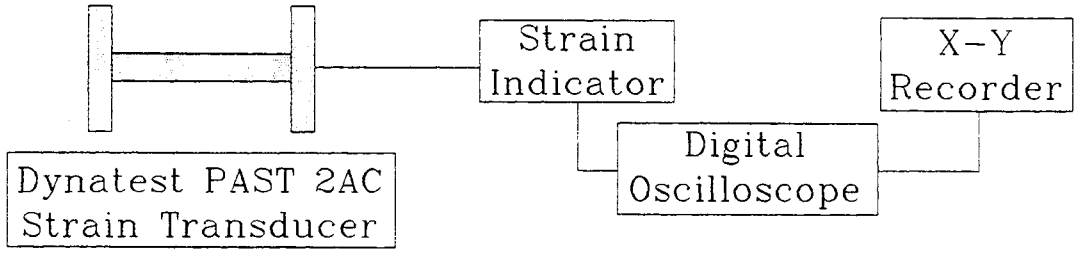

Figure 2.10. Strain measuring instrumentation used at T.H. 36.

a digital oscilloscope. See Figure 2.10 for a schematic diagram of the apparatus used. To determine if the gages were still operational, a preliminary check of the grid resistance was made using a DMM. It was found that the resistances of each gage fluctuated randomly between about 125 to 140 Ω. The nominal resistance of these gages, as reported by the manufacturer, should be 120 Ω $\pm$1 percent. These fluctuations are presumably due to environmental deterioration of the transducer such as grid corrosion due to water infiltration. They may also be due the effects

of temperature changes on the gage lead-wires. Rather drastic shifts in the zero strain balance reading occurred throughout the session due to the fluctuations in gage resistance.

Data were obtained for several multiple-axle trucks by triggering the scope manually just as the vehicle approached the site. Using the hold function on the oscilloscope, the transducer output trace was then displayed on the screen for analysis. When a satisfactory trace was obtained, the contents of the screen were dumped to an x-y recorder. Two representative plots are shown in Figure 2.11. Bridge output voltages on the vertical axis have been converted to strain units. The data were obtained from the transducer located directly beneath the anticipated wheel path. Due to the gage resistance fluctuations, a bridge balance and calibration check was performed between each reading. This was done primarily to insure a stable zero balance just prior to each of the readings.

Conclusions that can be drawn from this study are that the transducers (a) are still functional (they were not destroyed during construction), and (b) appear to yield reasonable results.

Nardo Road Test

Extensive strain gage instrumentation of a flexible pavement test section was carried out at the Nardo Test Site, Nardo, Italy in 1984 [5]. The test program, primarily concerned with strain measurement in bound layers, involved the research efforts of 10 different countries. Although the test was a cooperative effort, each team pursued its own objectives and utilized individual gage designs.

During construction of the asphalt concrete layer non-vibratory compaction and lowered asphalt mix temperatures were used in order to attain a high gage survivability. The post-construction mortality rate was about 13 percent (out of 200 transducers). Success varied from team to team as some of the groups paid greater attention to gage protection. Most of these gages were presumably lost to intrusion of aggregate into the gage. Significant losses of gages with aluminum strip protection occurred during construction. This protection method is presumably not sufficient. The pavement tests at Nardo do not seem to reflect true pavement loading due to the precautions taken during construction. No conclusions can be drawn concerning the long-term service of the gages due to the reduced number of loadings.

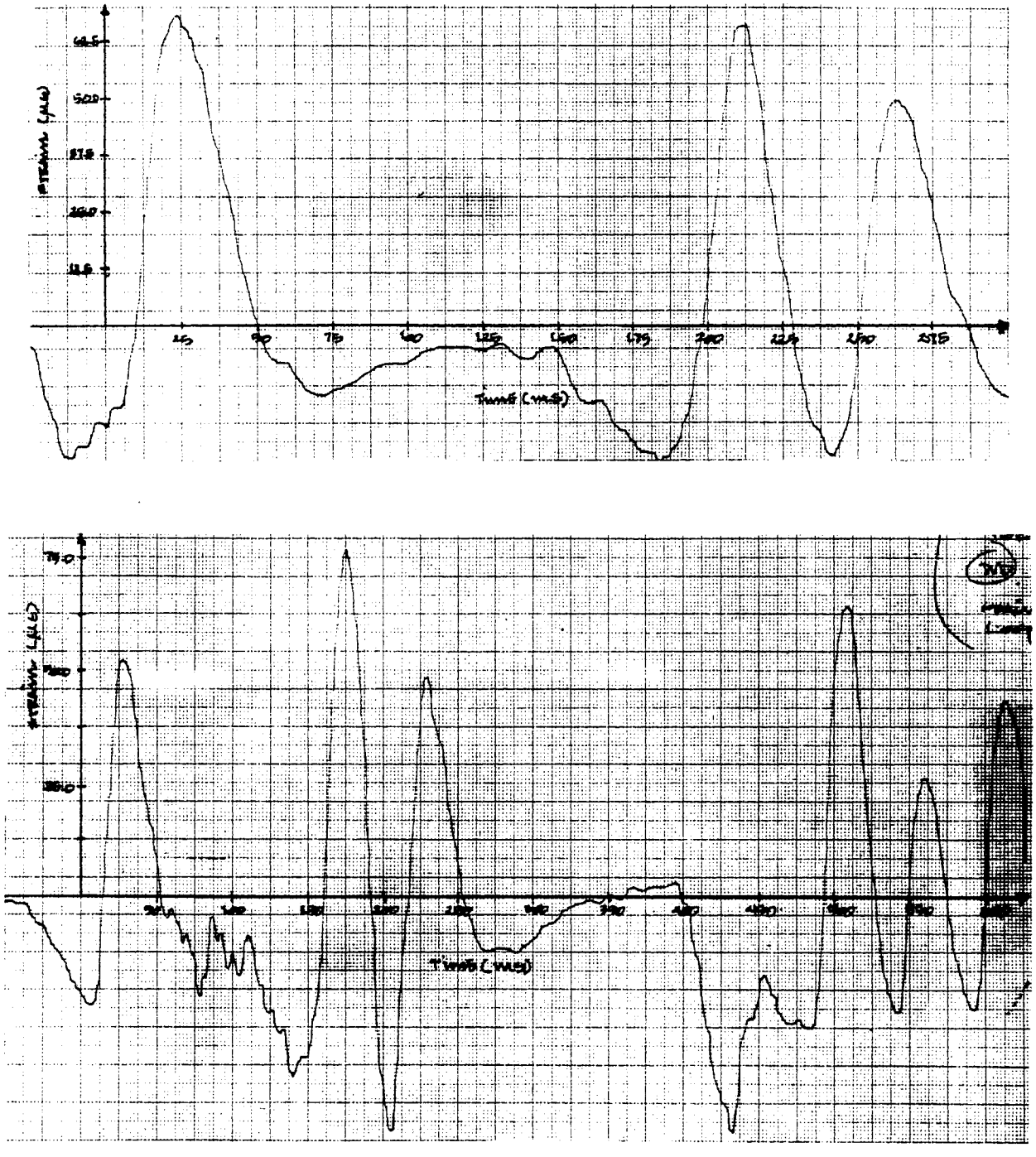

Figure 2.11. Transverse strains at the bottom of the asphalt concrete layer: T.H. 36.

The Danish team instrumented a test section with Kyowa model KM-120-H2-11L 100-3 embedment gages. Since the gage, as shipped from the distributor, is not suitable for direct installation, the gages were modified by attaching bars at the ends of the gage to provide better anchoring (Figure 2.1). Even then, the gage is not suitable for installation in pavements and is perhaps more suitable for controlled, short-term laboratory testing in portland cement concrete specimens. The active gage is situated between two acrylic resin wafers that are bonded together. The complete assembly measures $12 \times 15 \times 4.5$ mm. Its temperature range is 15°F to +160°F (-10°C to +70°C). The survival rate of these particular gages was quite high due to the reduced mix temperatures and non-vibratory compaction. It is believed that normal temperatures experienced during laying of asphalt lifts (280°F to 300°F) may cause failure of the gage due to its relatively lower operating temperature range. Also, at temperatures below freezing the acryl crystallizes and this may cause debonding between the acrylic wafers and gage, leaving the active gage open to moisture infiltration [5]. The manufacturer also indicates that the heat dissipation characteristics of the Kyowa KM series gages are not as efficient as other gages and they suggest that excitation levels be kept below 3 VDC.

Several of the teams instrumented test sections with gages adhered to cores or bituminous carrier blocks (Figures 2.3 through 2.5). Final installation occurred both before and during construction. The post-construction survival rate of these particular gages was relatively satisfactory (15 to 50 percent) but firm conclusions are difficult to make judging by the low number of installations.

At Nardo no efforts were made to protect lead-wires. Measurements of the grid resistance made during the tests indicated that many of the gages had failed (i.e., infinite gage resistance). After 9 months the rate loss was approximately 15 percent. It was also noted that some of the gages displayed instability in the form of altered grid resistances. It is thought that this was due to the effects of water infiltration at the lead-wire ends which were exposed at the pavement edge. Another possible explanation is temperature effects on the resistance of the lead-wires; a problem that can be alleviated by using a three lead-wire system as discussed above.

U.S. Army Corps of Engineers

During a recent experiment at the Army Corps of Engineers Waterways Experiment Station (WES) a test pavement was instrumented with strain gages [12]. Due to budget and resource constraints WES engineers opted for the retrofitted core method instead of gages installed during construction. The test section is an asphalt concrete pavement approximately 3 inches in thickness.

A major problem with retrofit approach is the inability to obtain satisfactory bonding between the retrofitted core and pavement. In an attempt to achieve better bonding around the periphery of the core WES engineers approached the problem in the following way. First, a barrel having a 4-inch outer diameter was used to bore a hole at the proposed strain gage location and then a second hole was drilled at an arbitrary location using a barrel with a 4 inch inner diameter. The larger of the two cores was used for the strain gage installation.

In order to bond the strain gage to the bottom of the core a smooth surface must be obtained (Figure 2.12). A groove approximately 0.5 inches deep and wide enough to place the gage was machined on the bottom of the core. It is suggested that just enough material be removed to provide a uniform bonding surface. Removing too much material will likely create large variances in the local strain field after the core has been placed back in the pavement. Another groove is machined along the edge of the core to provide a route for the lead-wires.

Due to the porous nature of asphalt concrete it is necessary to seal the area upon which the strain gage will be bonded. This was done by applying a thin layer (approximately 0.005 thick) of 3M 1838 B/A structural adhesive to the previously machined surface. It is important to apply just enough adhesive to fill all the voids on the surface; application of a layer that is too thick may affect the response of the strain gage.

Once the epoxy sealer coat has cured the surface must be prepared in accordance with usual strain gage installation procedures. After the gage has been installed, the steel block and Teflon should be placed on top of the gage while the adhesive is curing. Apply a load sufficiently large to provide a uniform stress of at least 10 psi over the area of coverage of the steel block.

When the adhesive has cured, the installation should be protected with a waterproof sealant. Technicians at the WES used an RTV sealant to fill the groove over the gage. It may

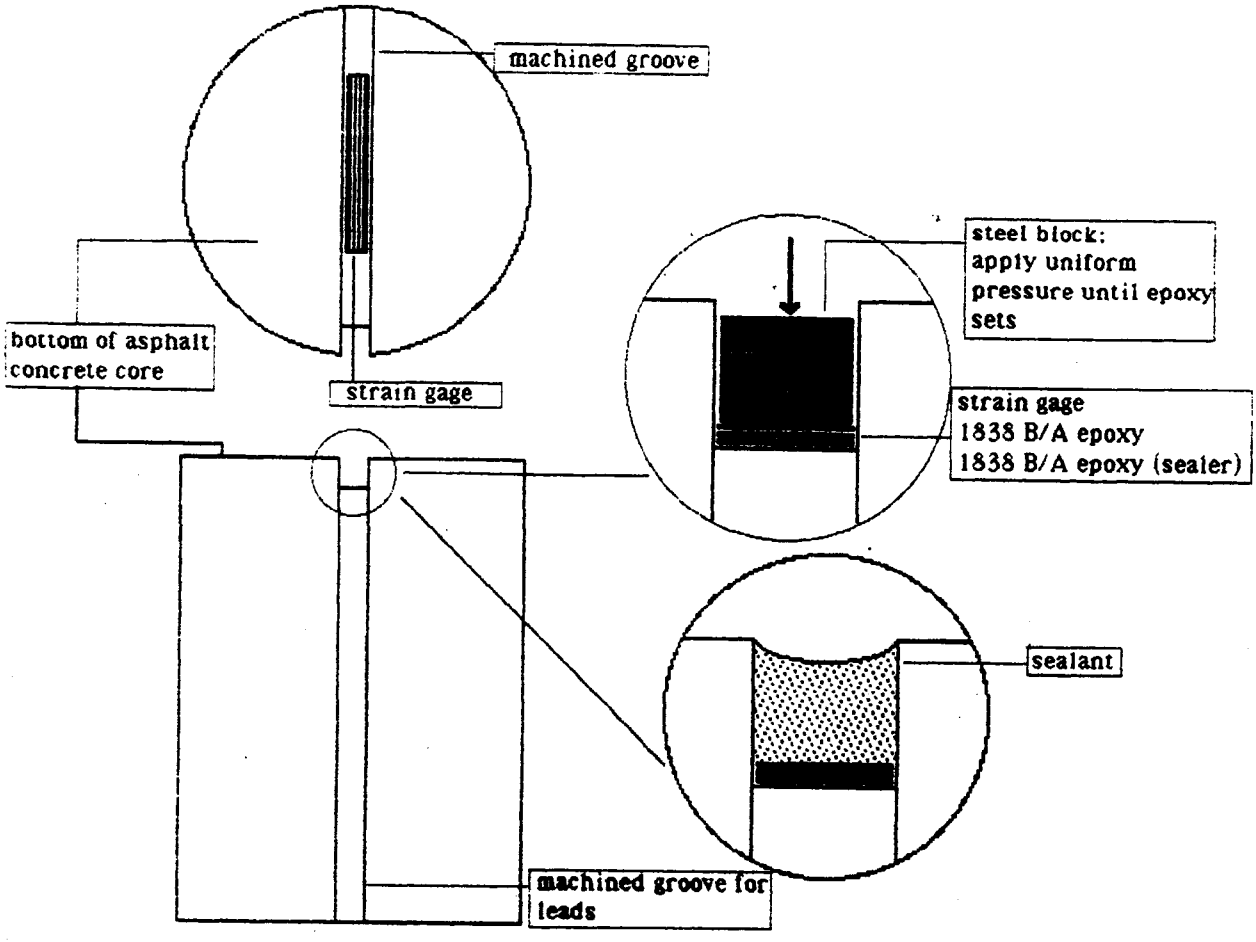

Figure 2.12. Installing a strain gage on an asphalt concrete core [12].

also be wise to place a thin strip of metal over the gage before applying the sealant to protect it from being pierced by sharp pieces of aggregate. The instrumented core is then ready for installation into the pavement.

The selection of adhesives for bonding both the gage and core is left to the practitioner. It would be useful to experiment with different methods in order to select one that works properly.

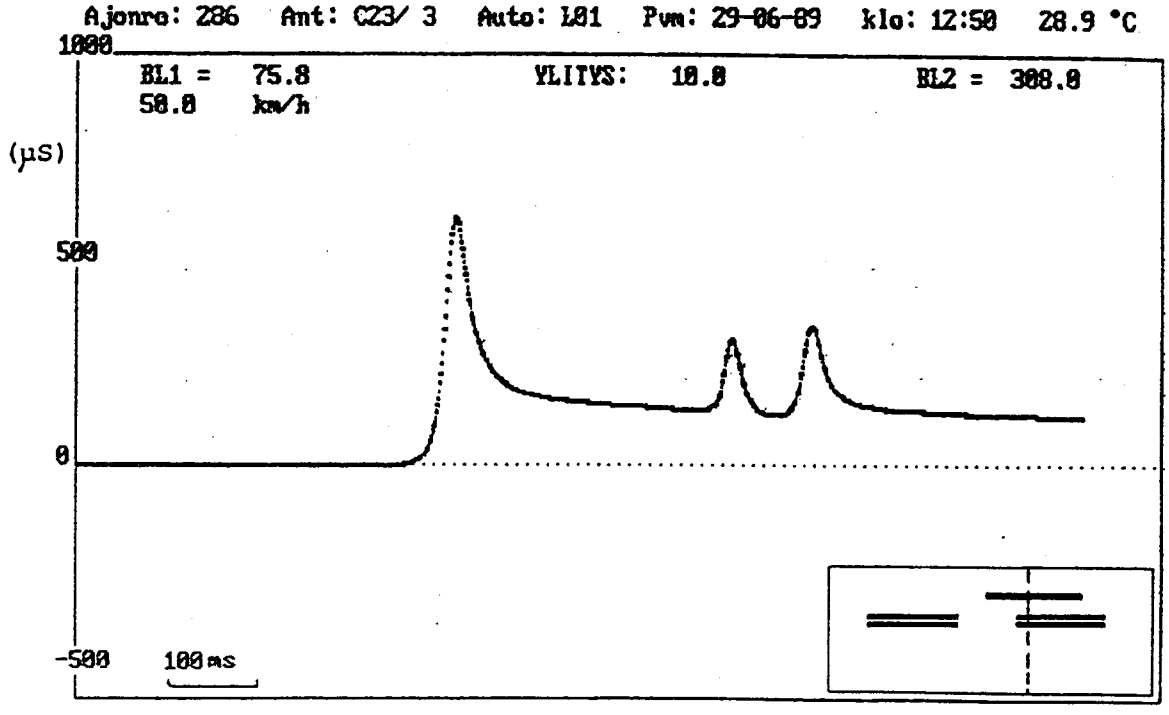

Figure 2.13. Transverse strain gage signal; front tire passes over gage, tandem passes near edge [7].

Virttaa Test Track

Results obtained by the Finnish researchers have confirmed the fact that alignment, or knowledge of position of the vehicle relative to the strain gage is extremely important [7]. In Figures 2.13 and 2.14 are shown strain gage signals obtained during testing at the Virttaa test track. Figure 2.13 shows the transverse strain due to the passage of a three-axle truck in which the drive axle has passed directly over the strain gage and the tandem axle passes just to the edge of the gage. Figure 2.14 shows the response from another passage of the same vehicle where the tandem axle has completely missed the gage. Thus, misalignment may yield responses that defy interpretation if the position of the loads are not known.

Alberta Research Council

Strain gages for embedment into bituminous layers used by the Alberta Research Council (ARC) are constructed in the following manner [8]. An electrical resistance strain gage is embedded between two sheets of a bituminous mixture. This material is actually gussasphalt,

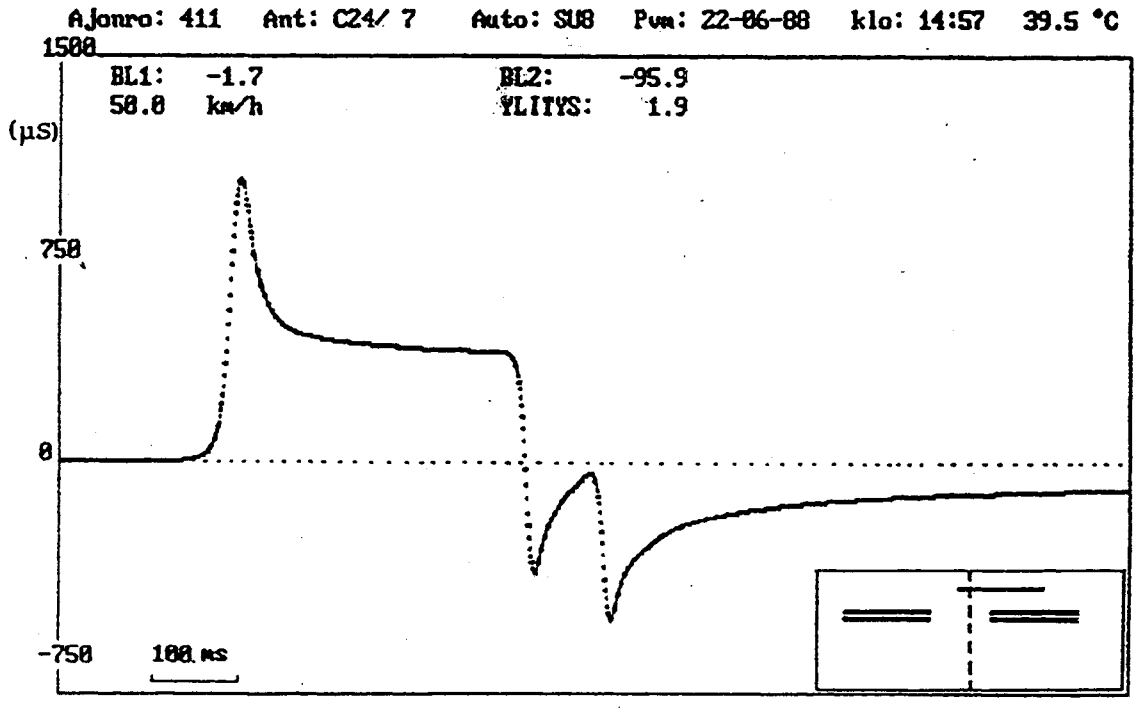

Figure 2.14. Transverse strain gage signal in which the front tire passes directly over the gage, rear dual completely misses [7].

a sand-asphalt mixture. Each 6-inch by 6-inch sheet is 0.25 inches thick. The sheets are formed using molds of the appropriate size; the strain gage, with lead-wires attached, is then placed between the two sheets. By placing the assembly at room temperature for a short period of time the individual sheets adhere to one another due to the rheological characteristics of the bitumen. The units should be stored in a freezer if they are not to be installed immediately since the bitumen will flow at elevated temperatures. Because the strain gage is not in direct contact with the bituminous mixture, smaller gage lengths may be used. This has the advantage of eliminating errors induced by using long gages.

Advantages of this particular gage configuration are that localized stiffening effects are essentially eliminated, that is, the strain gage is free to move with the surrounding material at any temperature or load level. However, the material immediately surrounding the strain gage may be much less stiff than the adjacent mix, thereby creating another sort of inclusion effect. During paving, the bitumen sheets will most likely flow around the gage and meld with the hot mixture. Thus, it may be possible for aggregate in the bituminous mixture to intrude into the

sheets and disrupt the orientation of the transducer. The only feasible solution for this problem is to minimize the thickness of the gussasphalt sheets such that adequate protection from aggregate intrusion is ensured. Also, a spare gage may be placed in the assembly and wired into the existing circuit should the original strain gage fail.

CHAPTER 3
DISPLACEMENT MEASUREMENT

Vertical displacements of a pavement due to a heavy wheel load are commonly used as an indication of the in situ stiffness of the pavement structure [13]. When a load is applied at the surface the pavement will deflect in a bowl shape commonly referred to as the deflection basin. Nondestructive testing techniques (NDT) involving the use of equipment such as falling-weight deflectometers (FWD) make it possible to measure the deflection basin due to dynamic impact loads. Displacement data from NDT results may then be used to backcalculate the effective layer moduli for the pavement structure [12,13,14]. The in situ effective layer moduli from such tests may be used to verify laboratory results and may also be incorporated into design procedures.

TYPES OF DISPLACEMENT MEASURING DEVICES

Dynamic displacements in pavements are commonly determined using the following devices:

- Linear Variable Differential Transformers (LVDTs)
- Velocity Transducers (geophones)
- Accelerometers

Of the above devices, the LVDT is the only one that measures displacement directly. Voltage output from a geophone or accelerometer is proportional to the velocity or acceleration of the sensor, respectively. Data obtained from these instruments must subsequently be numerically processed to obtain displacement. There is little data concerning the use of accelerometers in pavement instrumentation and is an area that needs further research. They will not be discussed in detail in this report.

Linear Variable Differential Transformers

A common means of accurately measuring displacements is the LVDT. LVDTs that are capable of measuring displacements of a few micro-inches to several feet are commercially available. Either AC or DC LVDTs are available. Advantages of LVDTs are that the

mechanical life, as well as the measurement resolution of displacements, are infinite. This is due to the fact that frictional forces are not involved in the operation of the instrument, the only limitations being the quality of the readout instrument or signal conditioning (demodulation) circuitry.

The principle of operation is simple. LVDTs are electro-mechanical devices and consist

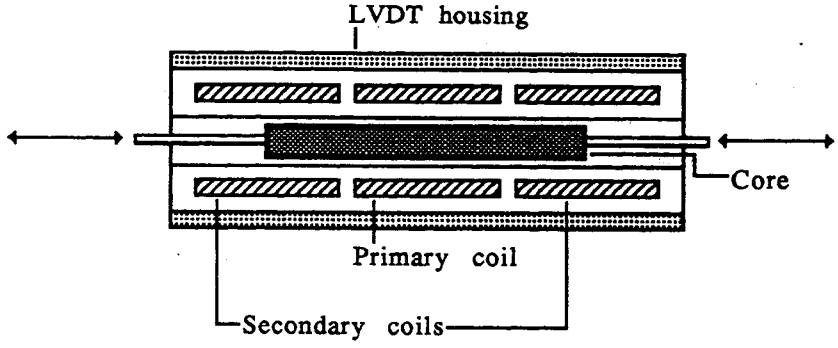

Figure 3.1. Components of an AC LVDT.

of three coils: one primary coil and two secondary coils (see Figure 3.1). The coils are symmetrically spaced on a cylindrical form. The primary coil is energized by an external AC source; a rod-shaped core is free to move inside the coils and the core provides a path for the magnetic flux linking the secondary coils. The two secondary coils are wired in series opposing so that the voltage in each coil is of the opposite polarity. Induced voltages in the secondary coils are directly proportional to the position of the core and the net output from the transducer is the difference between the two secondary coil voltages. The "null position" refers to zero transducer output when the core is centered. As the core is moved from null towards either side the induced voltage increases in the coil towards which the core moves, while the voltage in the other secondary coil decreases.

As mentioned above, AC and DC LVDTs are commercially available. The primary difference lies in the fact that output from the AC variety requires external signal conditioning equipment whereas output from DC LVDTs do not. Size is also a factor: DC units are larger than their AC counterparts owing to the electronic circuitry contained within the housing. Usual excitation levels for AC LVDTs are from 1 to 3 VAC (rms) at frequencies from 50 to 20 kHz.

The low-level output from the transducer requires amplification and this can be done before or after demodulation. Demodulation refers to the conversion of the AC output to a filtered DC signal.

One of the main advantages of AC LVDTs is that they are perhaps more durable with respect to environmental factors (e.g., moisture and temperature effects). With DC LVDTs the necessary electronic circuitry for conditioning the signal is contained within the LVDT housing itself and thus the unit is more susceptible to temperature and moisture effects. All circuitry for AC LVDTs is external and thus can be sheltered within an environmentally controlled surrounding. The operating temperature range for a typical AC LVDT is -65°F to +300°F whereas for the DC types it is 0°F to 160°F. Outside of these ranges the LVDT response will generally become non-linear and is a function of temperature.

The principles of operation for DC LVDTs are identical to AC types except that DC varieties are stand-alone units and require no external signal conditioning. Output from DC transducers is ready for readout on a multi-meter. Excitation levels for DC operated LVDTs are typically ± 15 VDC.

LVDTs are the primary component of in situ pavement deflection measuring devices and are commonly referred to as deflectometers. Deflectometers are simply a displacement transducer mounted down-hole. Deflectometers may be either single-layer (SLD) or multi-depth deflectometers (MDD). SLDs are commonly used to measure the pavement surface deflection whereas MDDs can have the capability of measuring displacements in each layer of the pavement structure. Researchers at the National Institute for Transport and Road Research (NITRR) have used data obtained from MDD instrumented bore-holes to determine the stress dependency of layer moduli during heavy vehicle simulation tests [14].

Velocity Transducers

Velocity transducers, commonly referred to as geophones, are another method of determining displacements in a pavement structure. A schematic diagram of the geophone is shown in Figure 3.2. As mentioned above, the output of a geophone is proportional to the velocity of the instrument. If the displacement time history is to be obtained the voltage output must be numerically integrated. Thus, a thorough understanding of the response of the geophone

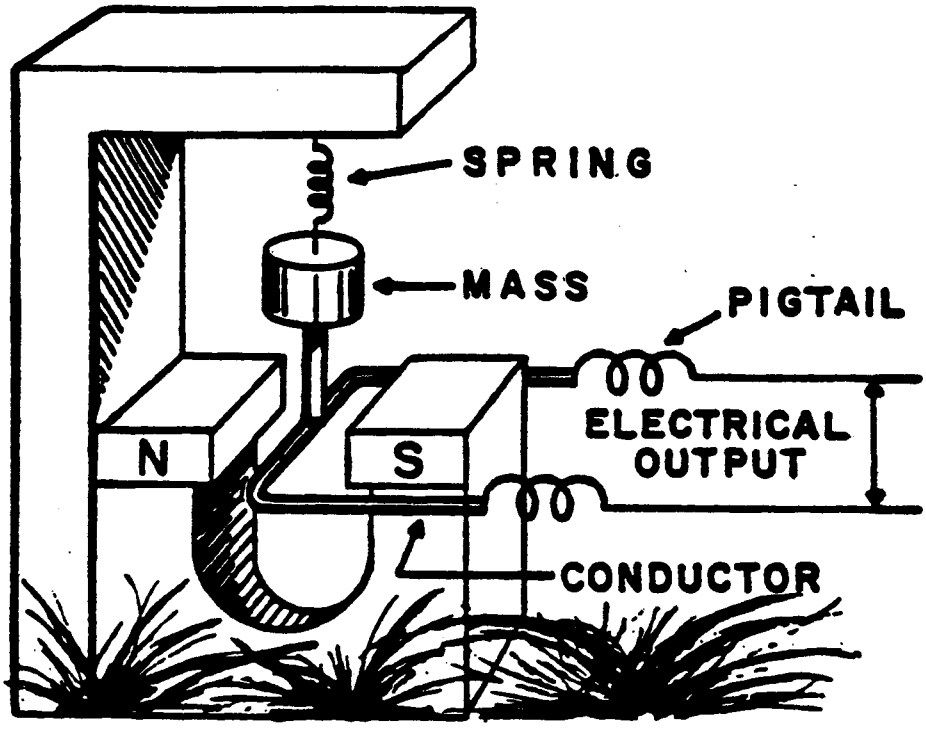

Figure 3.2. Idealized model of a velocity transducer [18].

to an impulse is necessary for interpretation of output. The mathematical derivation of the physical relationships for the geophone system are beyond the scope of this report and the reader should refer to Nazarian and Bush [16] for a discussion relevant to pavement instrumentation. Various numerical techniques are covered elsewhere [17].

A geophone consists essentially of a mass that is attached to a spring and coil. The coil is situated such that it crosses a magnetic field. Any impact sustained by the assembly causes it to move while the mass tends to remain stationary [16]. The physical properties of a geophone that need to be considered are the natural frequency, transductivity, and damping. The natural frequency is the undamped frequency of the system. Transductivity is the ratio of transducer output voltage to velocity of the geophone. Damping represents the time rate of attenuation of the motion.

It should be noted that the selection of a geophone for a particular application depends

on the expected amplitude and frequency of the phenomenon being studied. In general, geophones possessing lower natural frequencies are required to monitor low frequency displacements and the physical size of the geophone increases with decreasing natural frequency. In a pavement system, the frequency and amplitude of an impulse created by the passing of a heavy wheel load will be attenuated with depth. Thus, it is impractical to employ geophones for the purposes of determining displacements below a certain critical depth within the pavement structure for two reasons: (1) the physical size of the geophone would become unwieldy, and (2) noise will become a significant factor due to low impulse amplitudes [12].

In pavement instrumentation applications, the geophone will most likely be located either at the surface of the pavement or embedded at some depth beneath the surface. If an impulse is imparted to the pavement, and the geophone is securely secured in place, it will follow the motion of the surrounding material closely; the internal mass and spring tend to remain stationary. The motion of the transducer induces a voltage in the coil-magnet system. It is this voltage output that is recorded and processed to obtain the displacement. The voltage output from the geophone is not proportional to the motion of the layer in which it is embedded. In actuality, the output is proportional to the motion of the coil-magnet system, and must be transformed to the actual movement of the geophone. It should be noted that there is no absolute reference point for displacement data obtained from a geophone. Thus, it is not possible to obtain information concerning permanent deformation from displacements obtained with geophones.

The most common method of transforming the geophone output is numerically. There exists three approaches that are commonly used and they are (1) the time-domain solution or Duhamel integral method, (2) the Laplace transform method, and (3) the frequency-domain solution or Fourier transform method [16]. The Laplace transform method is perhaps more suitable for hand calculation whereas the time-domain and frequency-domain solutions are typically implemented in numerical approaches. Limitations of the time-domain solution are that only the maximum displacement may be determined whereas the frequency-domain solution can provide the entire time-displacement history. This approach is, however, computationally more time consuming.

Geophones are normally calibrated using a shake table. The procedure is performed by

attaching a reference accelerometer and the geophone to be calibrated to the shake table. The table is vibrated with an arbitrary waveform, generally a sine-shaped source. The response of the accelerometer and geophone are monitored simultaneously; the accelerometer output is integrated to obtain its response in terms of velocity. This procedure is performed at various frequencies. The ratio of the geophone output to integrated accelerometer output is plotted against the frequency to obtain the calibration curve.

IN SITU DISPLACEMENT MEASUREMENTS

Vertical Displacement

This section is divided into discussions on multiple depth and single layer deflection measurement. Multiple depth measurements refer to instrumentation systems where several transducers are located at various depths within a borehole in order to ascertain the deflection components contributed to the overall deflection by each individual layer. Single layer systems utilize a single transducer designed to measure the deflection of the surface only, usually relative to some fixed datum, such as a deep-set reference point, or the bottom of a particular layer. The Multi-Depth Deflectometer (MDD) was originally developed by the NITRR in South Africa. Evaluation of transient displacements due to passing wheel loads in several layers of the pavement system is possible.

Researchers at Texas A&M have installed up to six MDD modules in boreholes [13]. A typical MDD installation is shown below in Figure 3.3 and a schematic diagram of an individual LVDT module is shown in Figure 3.4. Such installations appear to be relatively durable. Instrumented boreholes at the WES were inundated with rainwater and after the boreholes were dried the modules appeared unaffected and gave valid results [12]. The LVDT modules were E-300 series LVDTs purchased from Schaevitz Engineering, Inc. This particular model is not hermetically sealed. Obviously, in climates where rainfall amounts are relatively high and flooding of the borehole is a possibility, procurement of hermetically sealed units would be wise.

Considerations for the design of an MDD system are given by Scullion et al. [13], and are summarized in Table 2.1. A vertical borehole approximately 8-feet deep is drilled for the installation of the MDD modules. To provide a reference datum for the measurements an

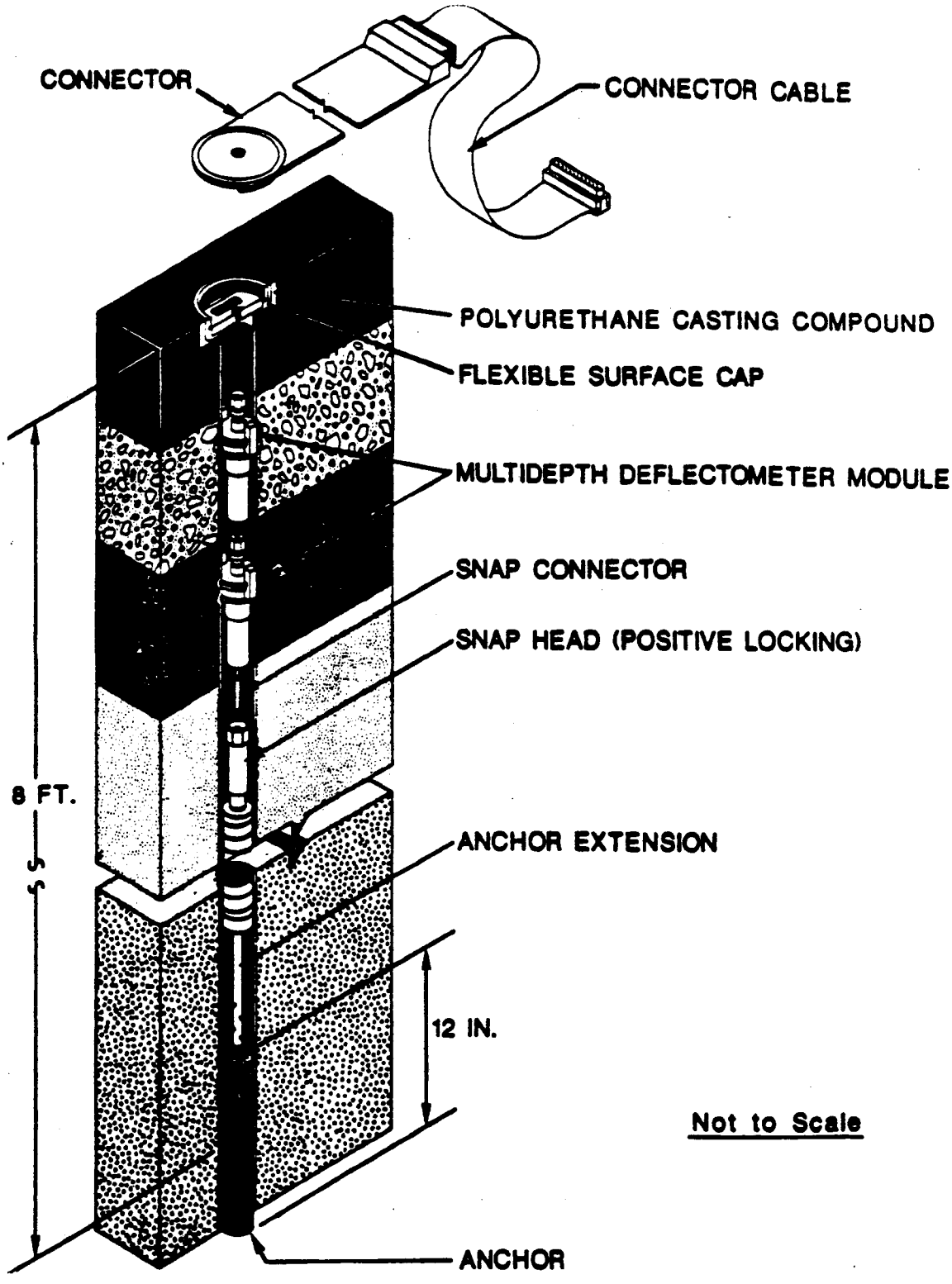

Figure 3.3. Schematic of an installed MDD system [13].

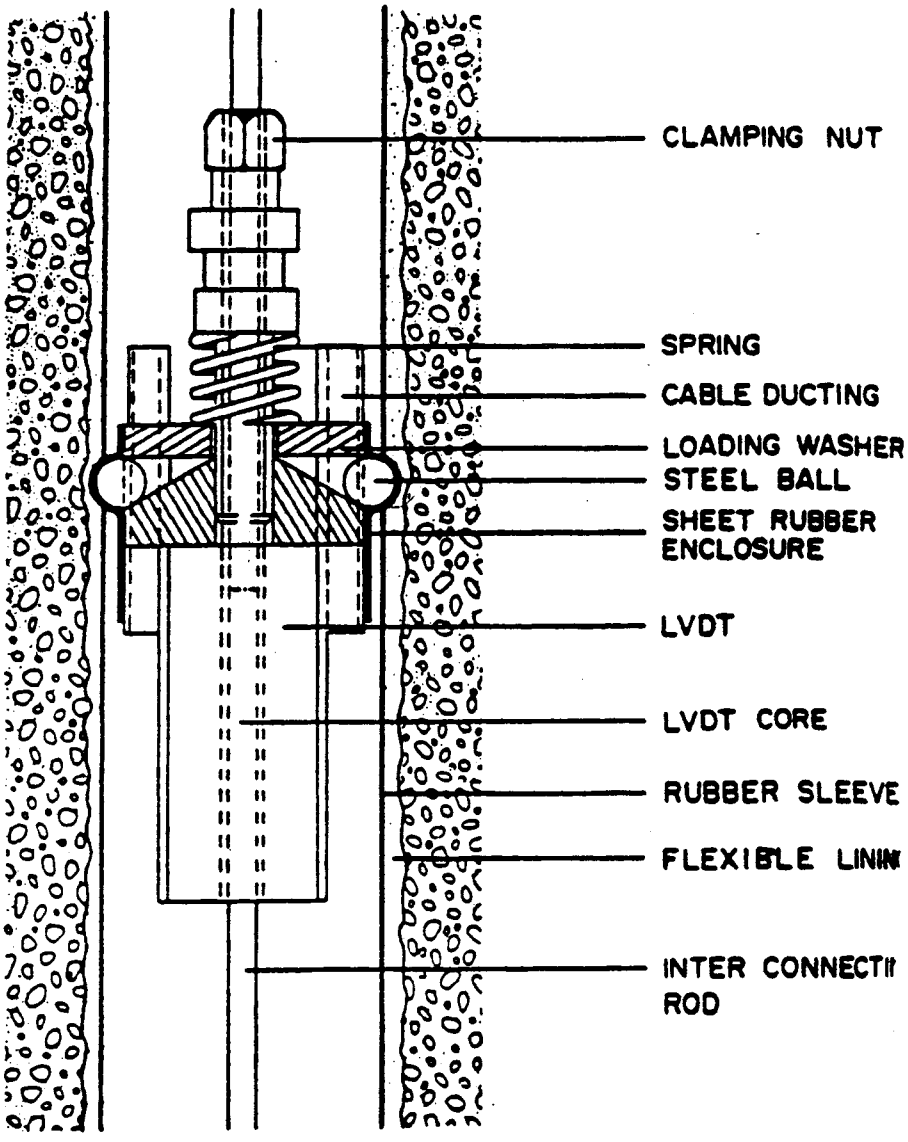

Figure 3.4. An individual MDD module [13].

anchor rod is placed in the hole and secured in place with a fast setting cement/sand grout. The LVDTs are housed in a custom designed module (see Figure 3.4) and the modules are linked by means of an interconnecting rod. A specially designed tool was developed for the installation of the module assembly. Individual modules are lowered into the hole and secured in place by turning the clamping nut at the top of the module. An extension attached to the lowest module joins the module assembly and anchor rod. Scullion reports that the complete installation takes

Table 3.1. Considerations for MDD installations, after [13].

Mechanical
o Diameter of the borehole should be about 1.5 inches
o Material adjacent to the borehole should remain undisturbed.
o Line the hole to prevent dislodging of any material during service life.
o Borehole should be sealed to avoid water infiltration.
Electrical
o LVDTs should be inert to environmental factors such as moisture and temperature.
o Protect leadwires and cables.
o Use shielded cable to minimize noise.

about 12 hours. On the first day the hole is drilled, lined, and the anchor is installed. The MDD modules are then installed and calibrated on the second day.

Conformance problems may arise with this particular installation. The borehole and accompanying instrumentation should not influence the response of the surrounding pavement structure. Scullion et al. have used tubes with a wall thickness of 0.1 inch to line the borehole. The material should be rigid enough to prevent caving-in of the soil surrounding the borehole yet compliant enough so that the installation does not strengthen the pavement structure locally.

Deflection data from a borehole instrumented with 5 MDD modules is shown below in Figure 3.5. The data were obtained during FWD testing at the Texas Transportation Institute Research Annex [13]. The pavement section consisted of a 5 inch asphalt concrete layer overlying a granular base and subbase, each 12 inches thick. During the testing it was noted that a high frequency noise was present in the signal. The noise was filtered by transforming the raw signal to the frequency-domain using a Fast Fourier Transform routine. After attenuating the noise frequencies an inverse transformation was performed to bring the signal back to the time-domain.

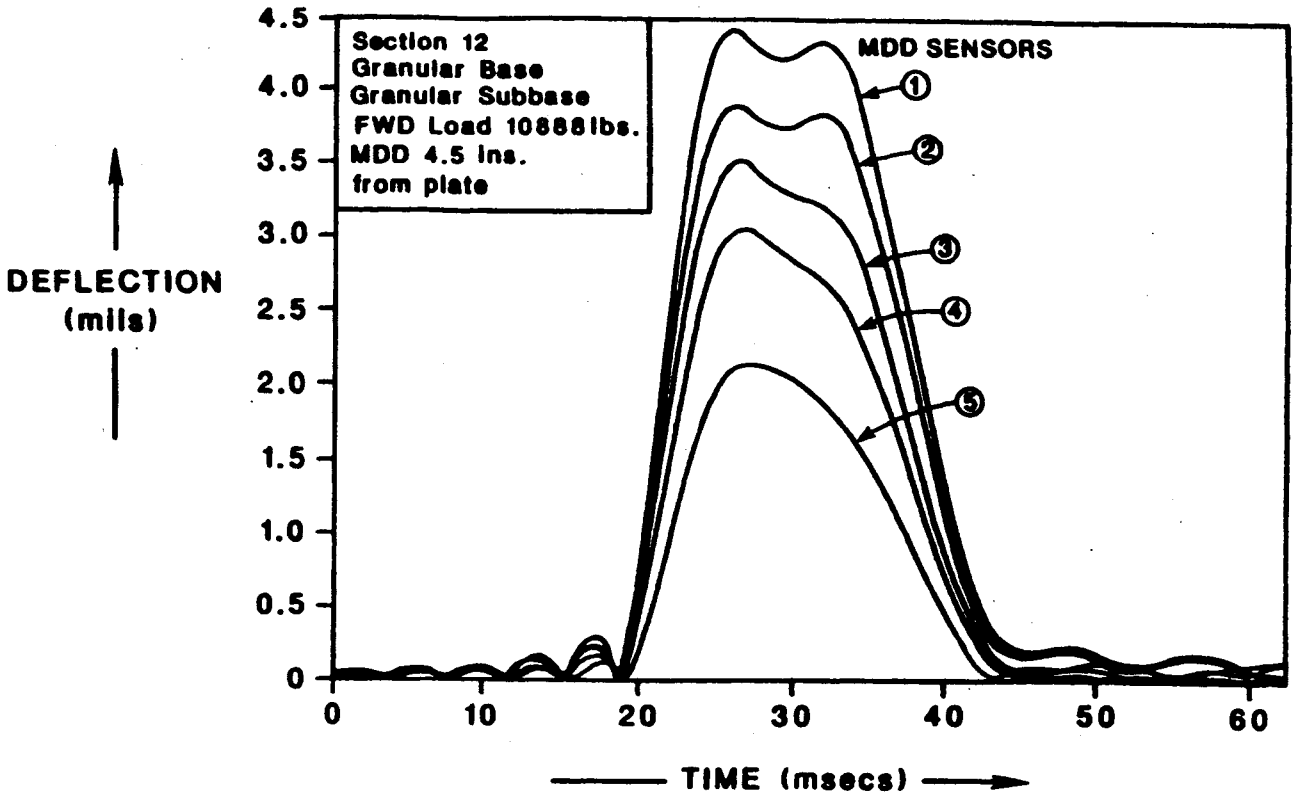

Figure 3.5. Deflection data from an instrumented borehole, FWD loading [13].

Single Layer Measurements

An alternative to MDDs are the use of single-layer deflectometers (SLD). These are built around displacement transducers such as LVDTs and are designed to measure the deflection of the pavement surface with respect to an immovable reference datum. SLDs are easier to install than MDDs and the signal processing costs are substantially lower. The disadvantage is that SLDs provide only one component of the pavement displacement.

A number of groups have installed SLDs successfully. However, the acquisition of meaningful results from such installations is hard to determine from the literature. An example of an SLD is shown above in Figure 3.6. This displacement measuring device was employed by the Corps of Engineers and was used to measure vertical surface displacements due to dynamic aircraft loads at an airfield in New Jersey [19]. Researchers at Iowa State University

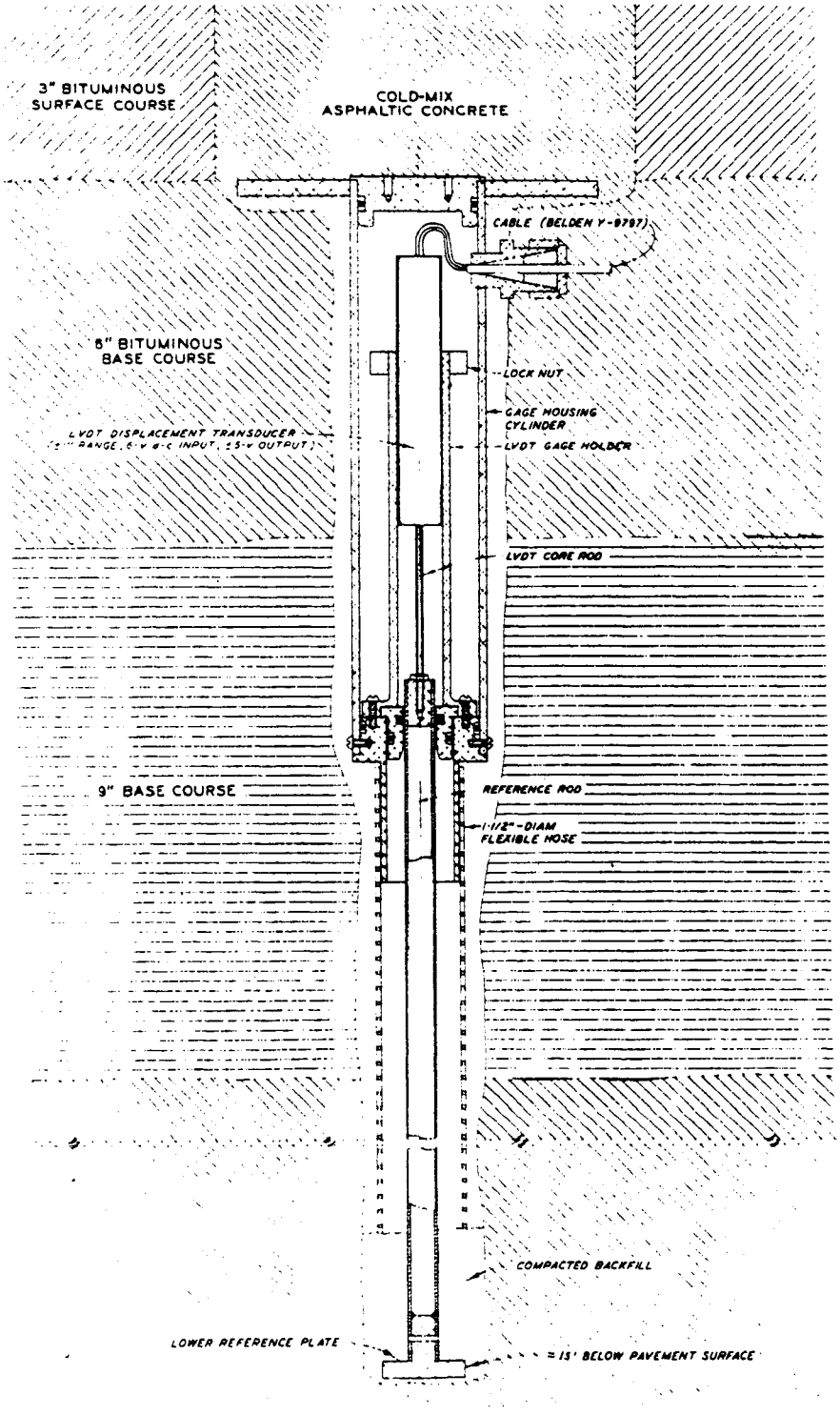

Figure 3.6. WES deflectometer installation details [19].

have instrumented a 40 foot section of rigid pavement on Interstate 80 in Iowa [20]. Among the sensors installed at this site are 16 SLDs. A schematic diagram is shown above in Figure 3.7. The SLD is built around a Trans-Tek DC LVDT.

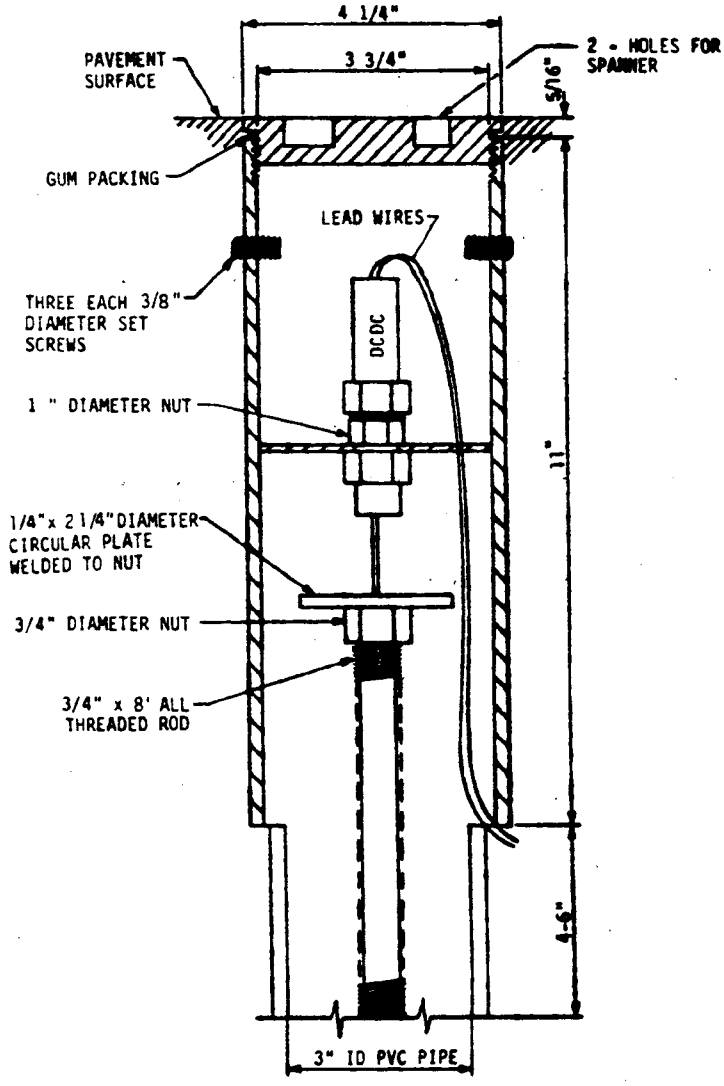

Figure 3.7. Single-layer deflectometer used at Iowa [20].

CHAPTER 4
TOTAL STRESS DETERMINATION

Instrumentation technology for the determination of stresses within soil has existed for decades, yet the measurement still remains one of the most uncertain parameters in geotechnical instrumentation. To understand the nature of the interaction between a stress cell and the surrounding soil a complete knowledge of the physical characteristics of the transducer and the soil must be obtained. In the following section the basic principles involved in the determination of total stress in soil are discussed. Various types of cell designs are reviewed as well as the primary factors that influence the determination of soil stresses. Laboratory calibration of stress cells is an important issue and will also be covered. An example of the development of theoretical correction factors will be given.

TYPES OF STRESS CELLS

There are basically two types of embedment stress cells: diaphragm cells and hydraulic cells. Diaphragm cells are constructed of a thin circular diaphragm attached to an outer annulus. Hydraulic cells consist of two plates welded around the periphery of the plates. The region between the plates is filled with a fluid. Several different types of cell construction are shown in Figures 4.1 through 4.5 with detailed discussions given by Dunnicliff [1] and Hvorslev [21].

There are various systems that are used to measure the response of a pressure cell to an applied external pressure. The most common means of measuring the response of diaphragm cells is through the use of resistive or vibrating wire strain gages. The gages can be bonded to the interior of the diaphragm and are sensitive to deflections of the cell face. A cell face that is instrumented or sensitive to applied loads is termed the active face, and one or two faces may be instrumented. Hydraulic cells are basically closed fluid chambers with a pressure transducer used to measure the internal pressure of the fluid in the cell. Each of these sensing methods has its own advantages and disadvantages [2,21]. Resistance type strain gages provide linear response to changing stress conditions and are also suitable for determining dynamic stresses. However, they are susceptible to environmental effects such as moisture infiltration at the gage. Vibrating wire sensing units have proven to be quite durable in the field [4] but possess a

nonlinear response and are not recommended for dynamic stress determination applications. Pressure cells of the hydraulic type are generally large and bulky, especially those having an external pressure transducer mounted on the cell face, and are commonly used to determine stresses surrounding large-scale structures such as dams and retaining walls [1,2].

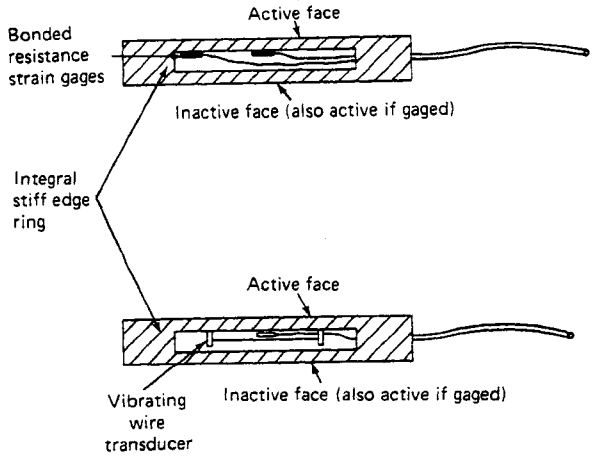

Figure 4.1. Typical diaphragm stress cells [2].

FACTORS AFFECTING STRESS DETERMINATION IN SOIL

This section will briefly discuss the various factors that influence the determination of total stresses in a soil. Detailed discussions are given by Selig [22], Dunnicliff [2], Hvorslev [21], and Weiler and Kulhawy [23]. The primary factors affecting stress measurements are stress cell geometry, its physical properties (e. g., flexibility, stiffness, thermal coefficient, etc.), as well as environmental conditions. These factors, which should be carefully considered when selecting a cell, are discussed in detail in the paragraphs that follow.

Cell Properties and Geometry

Cell geometry is a factor that is essentially out of the control of the user unless a special design is developed and produced for a particular application. When purchasing commercially

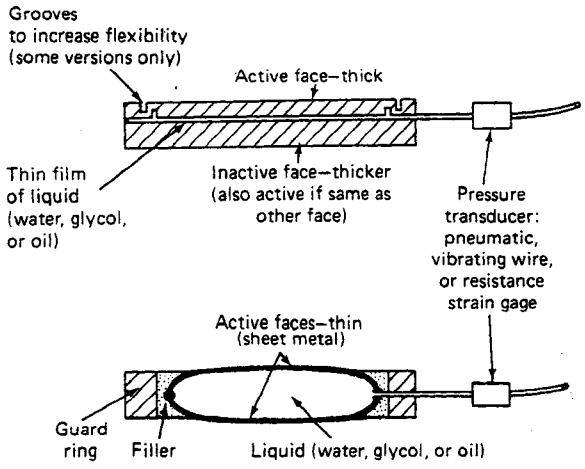

Figure 4.2. Typical hydraulic stress cells [2].

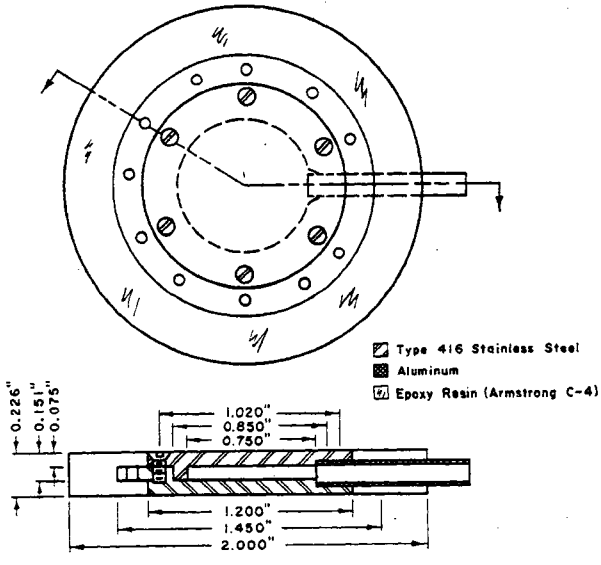

Figure 4.3. Corps of Engineers SE type stress cell [24].

Range PSI	Overpressure
0-15	2 Times Rated Pressure Range
0-50	
0-100	

Deflection	.0001" (0.0025mm) at Rated Pressure
Natural Frequency (KHz)	2
Operational Mode	Compression
Pressure Media	Any Liquid, Solid or Gas Compatible With 17-4 SS (H 900 Condition)
Rated Electrical Excitation	7.5VDC (Nom.)
Maximum Electrical Excitation	10VDC (Max.)
Input Impedance	750 Ohms (Nom.)
Output Impedance	350 Ohms (Nom.)
Full Scale Output	100mV (Nom.)
Residual Unbalance	±5mV (Max.)
Combined Non-Linearity, Hysteresis and Repeatability	Less Than ±1%
Resolution	Infinite
Operating Temperature Range	0°F to 100°F (−15°C to +40°C)
Compensated Temperature Range	32°F to 84°F (0°C to 30°C)
Thermal Zero Shift	±0.01% FRO/°F
Thermal Sensitivity Shift	±0.01% FRO/°F
Acceleration Sensitivity	NA
Humidity	100% Relative Humidity
Response Time (To Step Input)	NA
Active/Total Area Ratio	43%
Electrical Connection	Sealed Cable Assembly in Lengths Up to 33' (10 Meters) 10 Foot Length Standard
Insulation Resistance	100 Megohms @ 50VDC
Case Material	17-4 PH (H 900) Stainless Steel
Weight	250 Grams
Sensing Principle	4 Arm Strain Gage Bridge

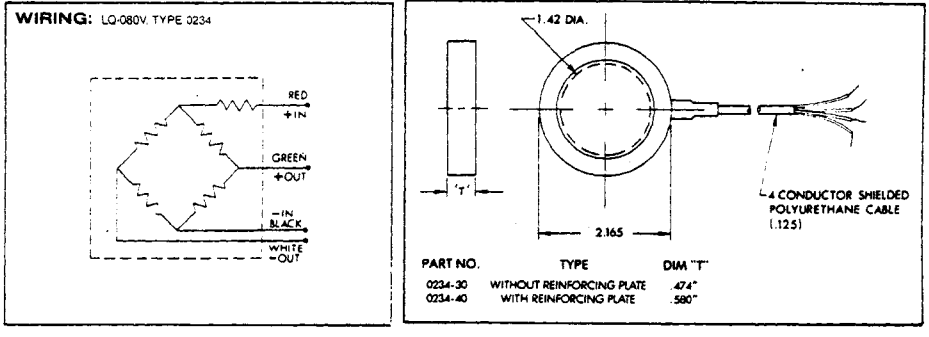

Figure 4.4. Kulite Model 0234 stress cell [25].

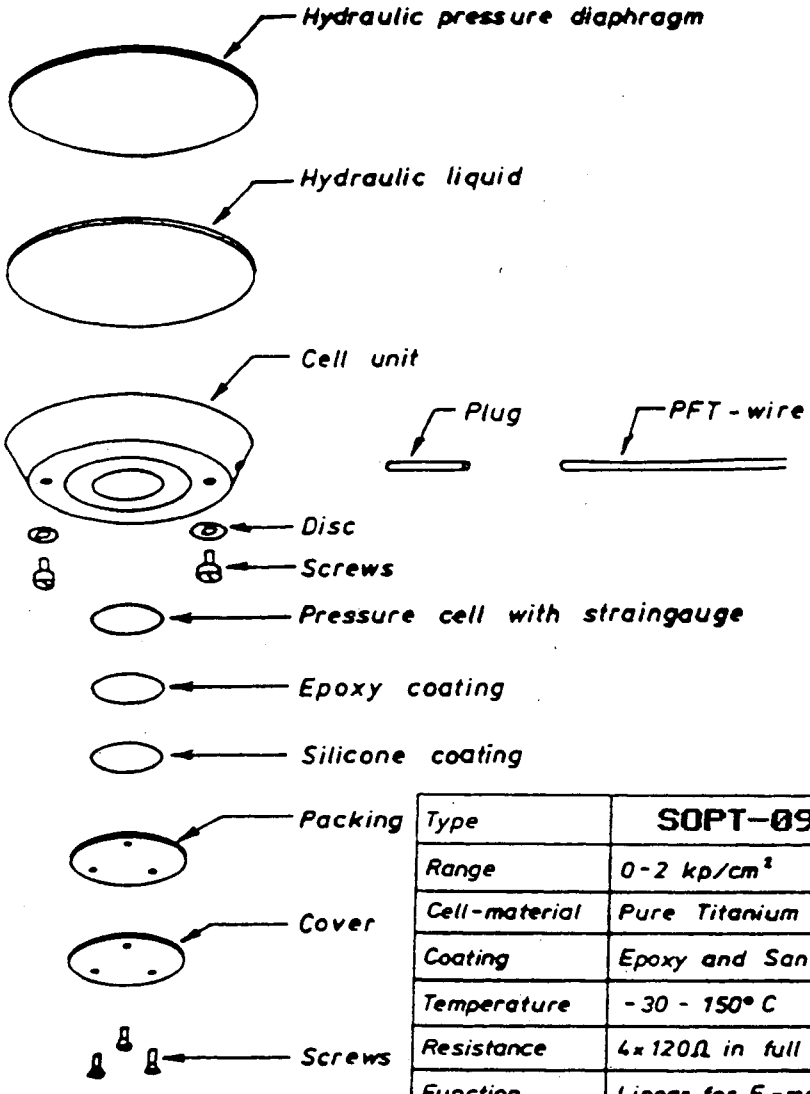

Type	SOPT-098	SOPT-298
Range	0-2 kp/cm²	2 - 8 kp/cm²
Cell-material	Pure Titanium	
Coating	Epoxy and Sand	
Temperature	-30 - 150° C	
Resistance	4 x 120Ω in full Weston Bridge	
Function	Linear for E-modulus < 5000 kp/cm²	
Output	Reff. Calibration Card	
Exiting Voltage	up to 12V	
Fatique-life	More than 3×10^6 cycles	
Service-life	> 36 months	

Figure 4.5. Dynatest SOPT stress cell [6].

available cells it is up to the user to select the proper cell for the application and then apply the necessary corrections and adjustments to any subsequent data. An important geometrical property of a stress cell is the aspect ratio. The aspect ratio is defined as the ratio of cell thickness to diameter, t/D. Collins et al. [26] performed theoretical analyses based on results due to Eshelby [27]. These results indicate that the registration ratio (C_N) is highly dependent on the aspect ratio (see Figure 4.6). The registration ratio is defined as the ratio of normal stress measured by the cell to the free field normal stress that would exist if the cell were not present. The results also show that minimizing the aspect ratio decreases the change in registration that may be caused by changes in Poisson's ratio (ν) of the soil. The aspect ratio also affects the relative percentage of horizontal stresses sensed normal to the cell [23]. This effect is known as "lateral stress rotation" [23] and will be discussed in detail shortly.

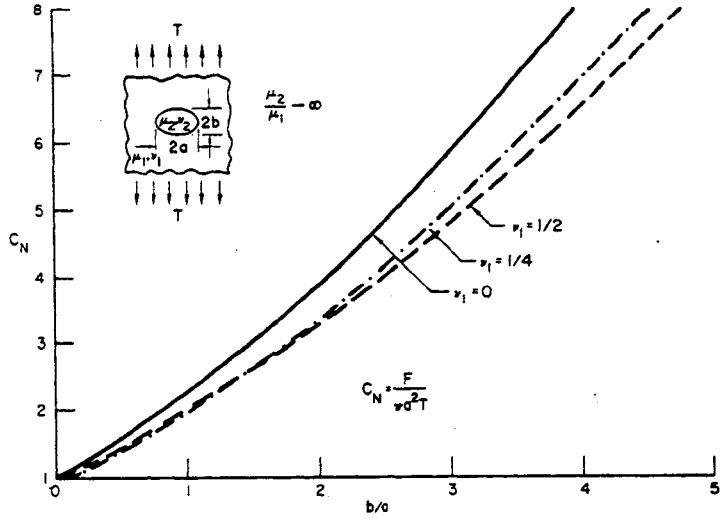

Figure 4.6. Influence of cell geometry on registration [26].

Another factor is the soil-cell stiffness ratio, or modular ratio. Because the stress field is distorted by the presence of the gage the stress measured by the cell will in general not be equal to the free-field stress. If the cell is soft compared to the surrounding soil it will tend to under-register, whereas, if the cell is rigid the opposite will be true (see Figure 4.7). Theoretical analyses have shown that the change in registration ratio is negligible as long as the cell is sufficiently rigid with respect to the soil [26,28]. This point is well demonstrated by the plot shown in Figure 4.8. These curves are from an analysis performed by Collins et al. [26],

based upon the theoretical work of Eshelby [27] and Edwards [29]. The results are based upon an analysis of a spheroidal inclusion loaded uniaxially in an elastic medium. Note that for each aspect ratio (b/a) C_N reaches a limiting value for increasing modular ratios. The modular ratio is defined as the ratio of the Young's modulus of the surrounding medium divided by the Young's modulus of the inclusion. This figure also shows that for increasing aspect ratios the ratio C_N is also increasing. Thus it is desirable to maintain a relatively high gage to soil modular ratio as well to minimize the aspect ratio. The modular ratio is difficult to determine, but Selig [22] suggests maintaining a ratio greater than 5.

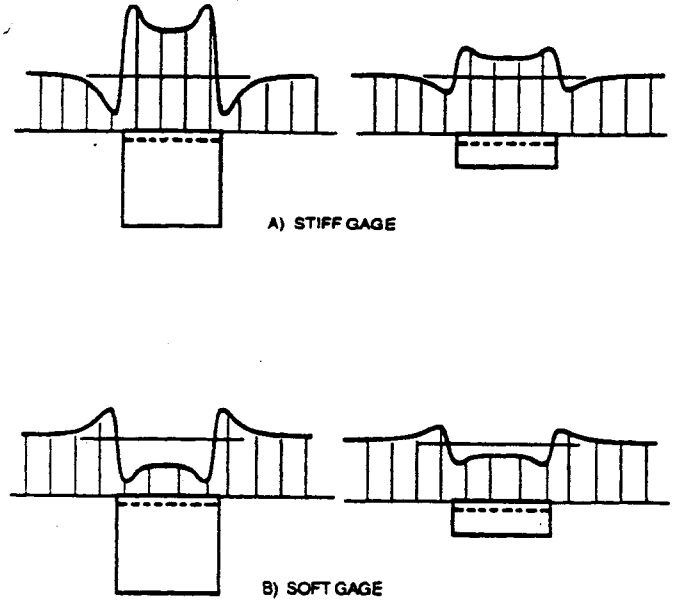

Figure 4.7. Illustration of the effects of stress cell geometry and stiffness on the in situ vertical stress distribution [22].

The theoretical results discussed thus far have dealt primarily with the stress cell represented as an infinitely rigid inclusion. This assumption simplifies the mathematics involved, however, in reality the active face of a stress cell will deflect under the applied stress. This deflection will cause some degree of arching in the soil surrounding the cell. Based on experiments conducted at the U.S. Army Engineer Waterways Experiment Station (WES) it is suggested that the central deflection of the cell be no greater than 1/2,000 of the diameter [21].

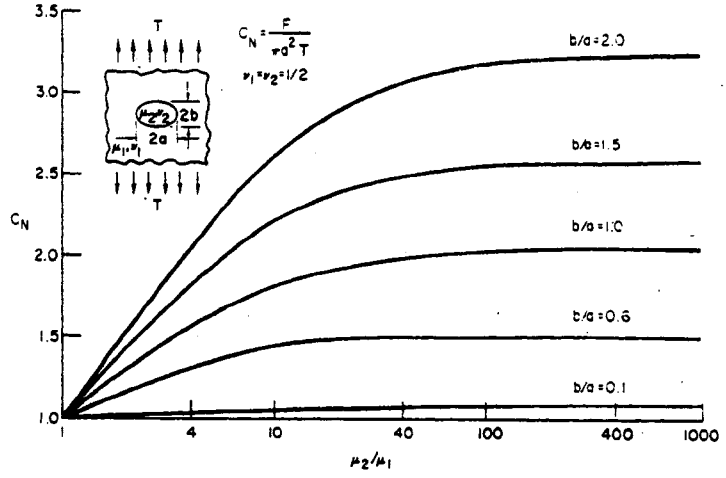

Figure 4.8. The relationship between registration ratio and modular ratio for a spheroidal inclusion under uniaxial load [26].

Weiler and Kulhawy suggest that this fraction be limited to 1/5,000 [26].

The stress distribution on the cell face is another important factor influencing stress determinations. Theoretical work performed by Monfore [21] predicted the development of stress concentrations at the corners of the cell. Experimental investigations on stress cells embedded in a pressurized soil chamber performed by Peattie and Sparrow [28] verified this result. These tests were conducted on cells with varying ratios of active area to total facial area. The results indicated that the active portion of the cell face should be limited to less about 40 percent for diaphragm cells and 25 percent for cells of the hydraulic variety. Nonuniform stress distributions also arise from point loading due to large pieces of aggregate adjacent to the active cell face. Selig suggests that the diameter of the active face be 10 to 50 times larger than the mean soil particle size [22].

As mentioned above, lateral stress rotation is an effect due to the presence of the cell in the soil. The presence of the cell disrupts the stress field and causes a percentage of the lateral free field stress to act normal to the cell [23]. This effect cannot be eliminated from the measurement and Collins et al. [26] suggest that knowledge of the (soil) Poisson's ratio and the cell aspect ratio can be used to derive theoretical correction factors. Weiler and Kulhawy adopted a technique, originally developed by Bates [23], that involved the placing of two cells

at each measurement location. By installing two cells, one horizontally and the second in a vertical orientation, measurements from each cell could be used to estimate the necessary correction factor [23].

Another influence of lateral stresses is the relative sensitivity of the sensing device to lateral compression. With stress cells employing strain gage circuits as the sensing device there may be some degree of lateral stress cross-sensitivity. Researchers at the University of Nottingham developed a stress cell that employed a sensing device having 4 active strain gages [30]. The advantages of this type of arrangement are the increased cell output and insensitivity to in-plane stresses. Weiler et al. [23] developed a cell possessing a system of two outer rings to isolate the cell from lateral stresses. The cell is surrounded by a flexible silicone ring and an outer ring. The silicone annulus allows the outer steel ring to deform without affecting the action of the sensing diaphragm. Special circular strain gages especially designed for use in flexible diaphragm stress cells are commercially available. Although these types of transducers do not completely remove the effects of cross-sensitivity they have an advantage in that only one gage is needed for each cell.

Environmental Considerations

Among the factors affecting stress determination that will be discussed in this section are stress cell durability and the effects of temperature. As discussed above, sensing devices that utilize strain gage circuits are susceptible to degradation due to moisture infiltration. For this reason, the cell should be completely sealed, especially where lead wires exit from the cell housing. Also, due to the presence of moisture in the layers of a pavement structure, the cell housing should be constructed of materials that are not susceptible to corrosion, e.g., stainless steel or titanium. Temperature changes will affect the performance of stress gages in several ways [21]:

1. Strain gages are sensitive to changes in temperature; if the cell utilizes strain gage circuitry as its sensing element, then the gages should be arranged in such a manner that compensates for temperature effects.
2. The metals used in stress cell construction possess thermal

properties far different from that of soil. Temperature changes will induce relative displacements of the cell surfaces with respect to the surrounding material. These displacements of may be considered as an extraneous deformation and incorporated into any subsequent theoretical correction factors [21].

3. In cells utilizing diaphragms filled with liquids such as oil or mercury, the effect of temperature dependent volume changes of the liquid must be taken into consideration. These effects cannot be eliminated even with cells possessing temperature compensated strain gage arrangements and correction factors should be derived during cell calibration.

There exist various configurations for arranging strain gages in a stress cell such that temperature effects are negated. The most common method is to employ a full bridge of strain gages. Early attempts at instrumenting flexible diaphragms with single strain gages for use in stress cells were futile due to the fact that large errors were introduce into the readings because of temperature effects [30].

In hydraulic type cells the presence of a large mass of fluid may effect the dynamic response of the cell. External pressure transducers can only exacerbate this problem since the back-pressure in the fluid (due to an applied load across the face of the cell) must travel through a conduit to reach the external transducer. Problems may be encountered if special efforts are not maintained to fully de-air the fluid.

CALIBRATION PROCEDURES

In order to derive a correlation between the voltage output of a stress cell to an in situ applied stress, it is necessary to calibrate the cell. Consulting the literature, one finds that many different procedures and recommendations have been proposed for calibration of stress cells. Dunnicliff [2], Hvorslev [21], Selig [22], and others recommend that the cell be calibrated in soil. Laboratory calibrations in soil can be accomplished by means of a large triaxial chamber or a rigid wall chamber. The soil and cell placement technique should duplicate the field conditions as closely as possible [21]. Such laboratory procedures should attempt to estimate

correction factors that will be applied to any subsequent field results. The development of an in situ calibration procedure would be a significant contribution to the field [2,22].

In planning a laboratory calibration program, the primary objective is to design a chamber such that the distribution of stresses within the chamber can be assumed to be uniform. Knowledge of the exact stress distributions within the testing chamber is important. That is, it is important to know what the stress should be at the location of the cell so that output from the cell may be evaluated properly. In the past, calibration chambers have taken the shape of right circular cylinders with some sort of means to eliminate sidewall friction [21,31,32,33].

Calibration of stress cells in soil can often be expensive and time consuming. An alternative method is to calibrate the cell in a fluid such as air or water. Correction factors based upon laboratory calibrations in soil are preferred but in many cases this may be impractical. Jackura [34] suggests that correction factors estimated by theory may be applied to fluid calibration data.

In large-scale laboratory tests with cells embedded in soil, experimenters at the WES discovered that constructing a jacket around the soil specimen with a large rubber membrane, and applying a layer of grease between the outside of the jacket and the inner wall of the chamber, was an effective means of obtaining tractable stress distributions (see Figure 4.9) [31]. Measurement of applied vertical stresses (using a gas) and back-pressure at the bottom of the soil specimen indicate that nearly 97 percent of the applied pressure was transmitted to the bottom of the specimen. This particular vessel was used by Hadala [31] at the WES in experiments dealing with effects of placement methods on the performance of pressure cells in laboratory tests.

The ultimate goal of laboratory calibration studies is to gain a detailed understanding of the performance of a particular stress cell relative to a specific type of soil. The soil should preferably be the same type of soil with which the cell will be used in the field and boundary conditions imposed by the vessel should duplicate stress conditions that may be expected in the field. Thus, if the researcher is forced to use a chamber in which sidewall friction is present an attempt must be made to account for the distribution of stresses. Interpretation of static calibration tests of a stress cell embedded in sand in such a chamber is the subject of Chapter 5.

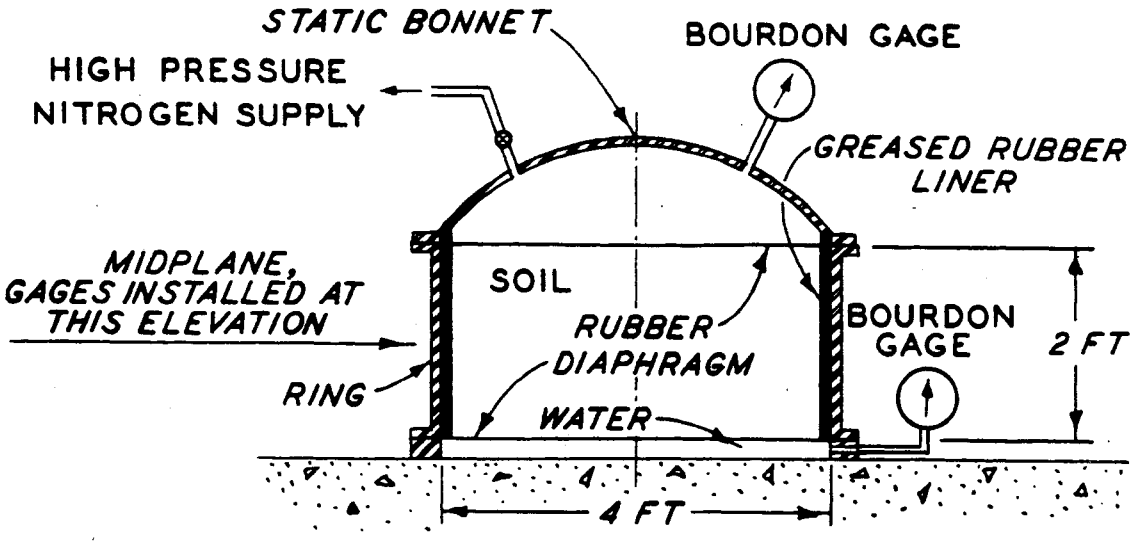

Figure 4.9. The WES stress cell calibration vessel [31].

INSTALLATION CONSIDERATIONS

The general procedure followed for the installation of a stress cell in an unbound material consists of excavating a hole for the cell, placing the cell, and then back-filling over the cell. The degree of compaction of the back-fill relative to that of the undisturbed material directly influences the stress indicated by the cell. Over-compaction of the fill may cause the cell to over-register, while under-compaction has the opposite effect. It is generally unknown, however, if these effects may dissipate over the course of the installation. It may be hypothesized that as the material relaxes, these initial soil density differences may dissipate. This may be especially true with fine-grained soils [31].

In soils having large particles, such as stones or gravel, the cell will yield erroneous results due to nonuniform loading if the cell and particles are in direct contact. Of course, the installation method selected for a particular application should depend on the type of soil in which the cell is being placed. If the soil contains stones, they should be removed and a layer of fine sand placed at the bottom of the excavation. The thickness of the sand layer should be just large enough to provide a smooth contact surface. A seating pressure should be applied to the installation when the cover has reached a depth sufficient to prevent damage to the cell [2].

Another important point for consideration are compaction procedures. Dunnicliff states that a method of compaction that pre-stresses the back-fill to the same degree as the surrounding material may provide better conformance [2]. The simplest placement procedures are usually the most easily reproducible and thus can be expected to reduce inconsistencies in data due to placement errors [31].

MECHANICS OF SOIL-CELL INTERACTION

Results from analytical solutions such as the ones presented above can provide useful insight into the response of a stress cell embedded within a soil. The solutions developed by Edwards and Eshelby are rather general and the solution to a problem with practical applications is intractable. Although the simplifications and assumptions involved in the simplified theory are rather drastic, the expressions obtained can provide qualitative answers to problems associated with soil-cell interaction. As will be discussed in Chapter 5, quantitative predictions from models derived from the simplified theory may not be feasible.

Consider the simple case of a stress cell (disk) situated horizontally in a soil mass as shown in Figure 4.10. The disk is located away from any boundaries so that the vertical stress acting on the plane occupied by the disk can be considered to be the vertical free-field stress (σ_s) that would exist if the disk were not there. Assuming that there is no change in the pore water pressure the change in total stress will be equal to the change in effective stress.
If the stress indicated by the disk (cell) is σ_c then the relative over or under-registration of the cell (σ_e) is

$$\sigma_e = \sigma_c - \sigma_s \tag{4.1}$$

If the Young's moduli of the soil and disk materials are E_s and E_c, respectively, then the total vertical displacement ($2\delta_c$) of the disk is

$$2\delta_c = \left(\frac{\sigma_c}{E_c}\right)t \tag{4.2}$$

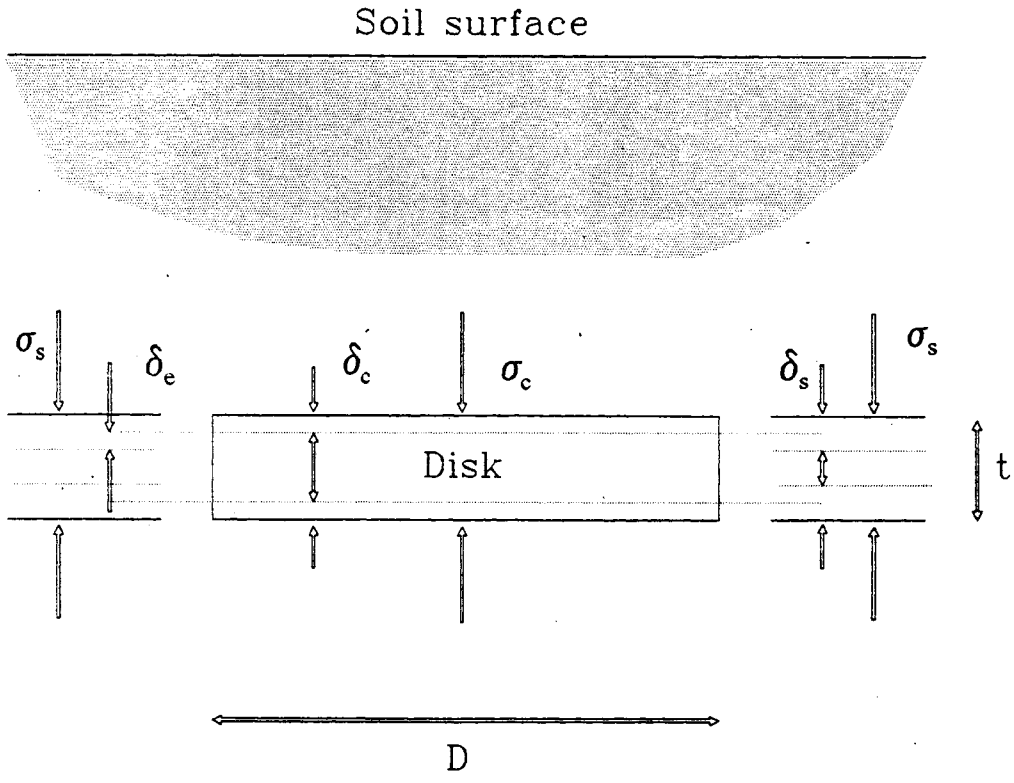

Figure 4.10. Simplified model of a stress cell in a uniform vertical stress field, after [21].

and the deformation of a soil layer ($2\delta_s$) having thickness t is

$$2\delta_s = (\frac{\sigma_s}{E_s})t \tag{4.3}$$

The difference between the displacements of the disk and soil

$$2\delta_e = 2\delta_s - 2\delta_c \tag{4.4}$$

$$\delta_e = \delta_s - \delta_c \tag{4.5}$$

Substituting the individual displacement expressions into the above yields

$$\delta_e = \frac{t}{2}\left(\frac{\sigma_s}{E_s} - \frac{\sigma_c}{E_c}\right) \tag{4.6}$$

The displacement δ_e is analogous to the indentation of an elastic solid due to a distributed load $\sigma_e = \sigma_c - \sigma_s$ acting on a circular plate. Taylor indicates that this assumption applies to both saturated clays and confined sand provided that the stress change σ_s does not approach that of failure [35]. The indentation δ_e can now be expressed as

$$\delta_e = \frac{D\sigma_e}{N_s} \tag{4.7}$$

where D is the diameter of the disk (cell) and N_s is an indentation coefficient. The coefficient N_s is a function of the material deformation properties; theoretical values discussed by Hvorslev [21] have been presented by Timoshenko and Goodier [36] and will be discussed shortly. Combining equations (4.1), (4.6), and (4.7) gives

$$\frac{D(\sigma_c - \sigma_s)}{N_s} = \frac{t}{2}\left(\frac{\sigma_s}{E_s} - \frac{\sigma_c}{E_c}\right) \tag{4.8}$$

and thus

$$\sigma_c\left(\frac{D}{N_s} + \frac{t}{2E_c}\right) = \sigma_s\left(\frac{D}{N_s} + \frac{t}{2E_s}\right) \tag{4.9}$$

The registration ratio can finally be expressed as

$$\frac{\sigma_c}{\sigma_s} = \frac{\frac{2D}{t} + R_s}{\frac{2D}{t} + R_s \frac{E_s}{E_c}} \tag{4.10}$$

where $R_s = N_s/E_s$ is called the soil indentation ratio. Equation (4.10) indicates that the registration ratio increases with increasing cell stiffness (E_c). In the limiting case of an infinitely stiff cell the ratio E_s/E_c tends to zero and equation (4.10) becomes

$$\frac{\sigma_c}{\sigma_s} = 1 + \frac{1}{2} R_s \frac{t}{D} \tag{4.11}$$

which indicates that the registration ratio reaches a limiting value that is linearly proportional to the aspect ratio.

Values for the indentation parameter N_s can be obtained from the theoretical solutions for the problem of distributed loads at the surface of an elastic half-space [21,36]. Using notation from the above analysis, the indentation δ_e of a rigid plate at the surface of the half-space δ_e is

$$\delta_e = \frac{D\sigma_e}{E_s} \frac{\pi(1-\nu^2)}{4} \tag{4.12}$$

Using equation (4.7) the indentation ratio can be expressed as

$$R_s = \frac{N_s}{E_s} = \frac{4}{\pi(1-\nu^2)} \tag{4.13}$$

Registration ratios computed using the above equation may be suitable for pressure cells having rigid surface plates. Analyses performed by Hvorslev [21] treated the case of a cell having thin (flexible) face plates. The objective was to determine the effects of various stress distributions across the cell surface with the average surface deflection. It was found that the stress distribution had little influence on the average plate deflection. Theoretical registration ratio values computed from equation (4.10) are shown in Figure 4.11 for constant $R_s = 1.5$ and t/D

equal to 0.01, 0.1, 0.25, 0.5, and 1. Figure 4.12 shows the same curves for constant t/D=0.25. and R_s equal to 1.0, 2.0, 5.0, 10.0, and 25.0.

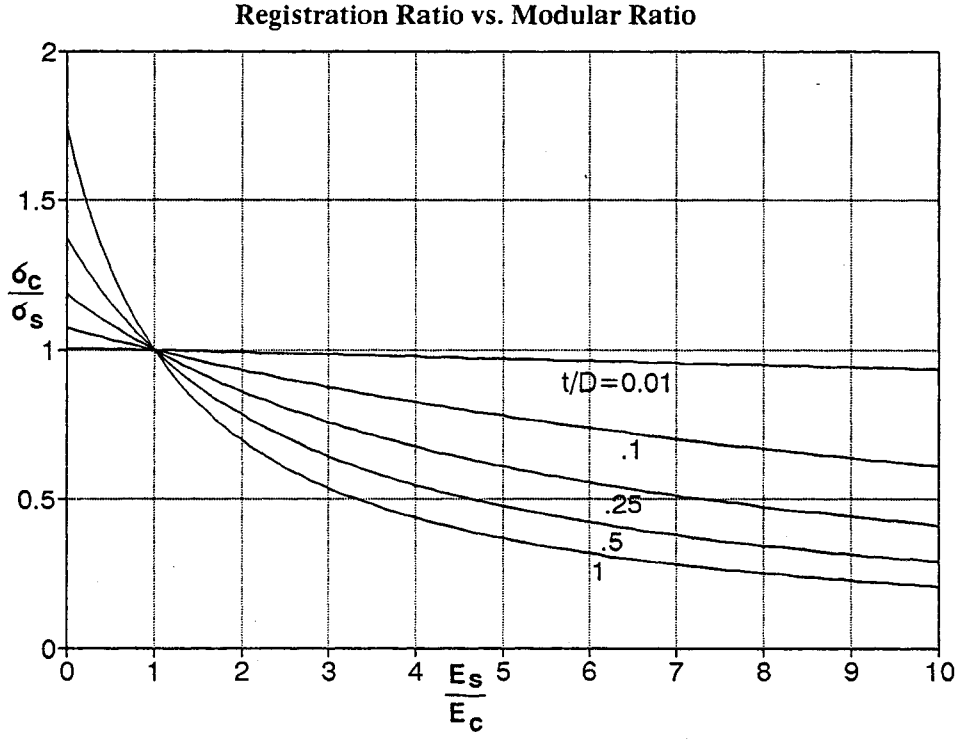

Figure 4.11. Theoretical cell registration as a function of the modular ratio for constant R_s=1.5.

This section expands on the solution presented above for more realistic cases. These solutions, based upon work originally performed by Taylor [35], and further developed by Hvorslev [21], will later be applied to laboratory and field data. Consider the same case as discussed in above, but with the addition of the effects of confinement. Equations (4.1), (4.2), and (4.4) still apply, however, the displacement of the surrounding material (δ_s) is now obtained from Hooke's law

$$2\delta_s = [\frac{\sigma_z - 2\nu(\sigma_x + \sigma_y)}{E_s}]t \qquad (4.14)$$

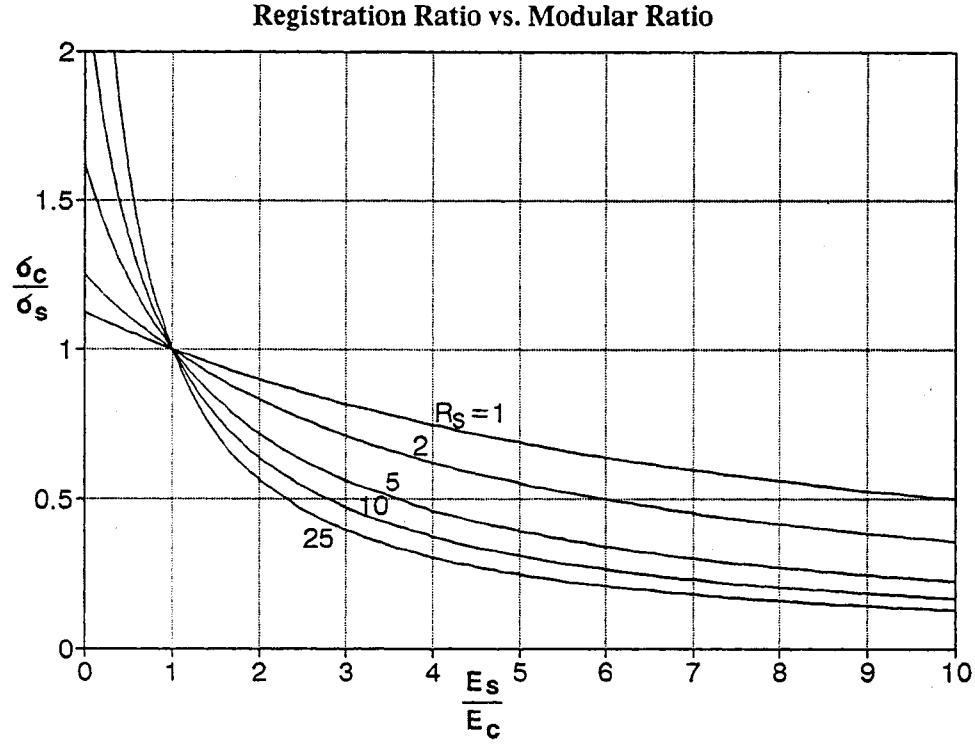

Figure 4.12. Theoretical cell registration ratio for various values of the indentation ratio (R_s) and constant t/D=0.25.

The over or under-registration σ_c and indentation δ_c are given as before by equations (4.1) and (4.5), respectively. With equation (4.14) we now have

$$\frac{\sigma_s}{N_s} = \frac{2D}{t}\left[\frac{\sigma_z}{E_s} - \nu\left(\frac{\sigma_x+\sigma_y}{E_s}\right) - \frac{\sigma_c}{E_c}\right] \tag{4.15}$$

Using equations (4.1) and (4.13) and assuming that $\sigma_s=\sigma_z$ and $\sigma_x=\sigma_y$ the registration ratio can then be expressed as

$$\frac{\sigma_c}{\sigma_s} = \frac{\frac{2D}{t} + R_s(1-2\nu K)}{\frac{2D}{t} + R_s \frac{E_s}{E_c}} \tag{4.16}$$

where K equals the ratio of lateral to vertical stresses, σ_x/σ_z. Plots of the registration ratio as a function of the modular ratio computed from equation (4.16) are shown in Figure 4.13. Curves are shown for constant R_s=1.5, K=0.5, and t/D=0.25 and values of ν equal to 0, 0.2, 0.3, 0.4, and 0.5. It can be seen that the effect of confinement, i.e., ν different from zero, is to reduce the registration ratio slightly.

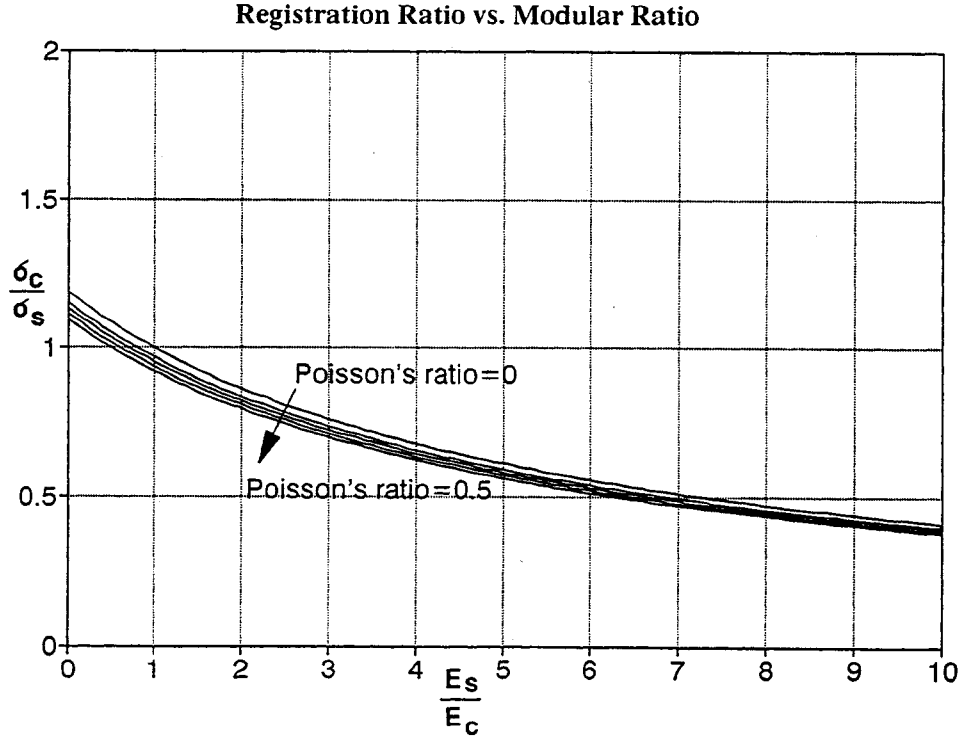

Figure 4.13. Registration ratios for varying Poisson's ratio (ν).

Taylor's solution (equation 4.10) can be modified to account for the effect of frictional shearing at the vertical soil/disk interfaces as follows (see Figure 4.14). It is assumed that such a shear stress is created due to relative displacements between the disk and adjacent material. Consider the same case as shown in Figure 4.10 but with the presence of a shear stress τ acting

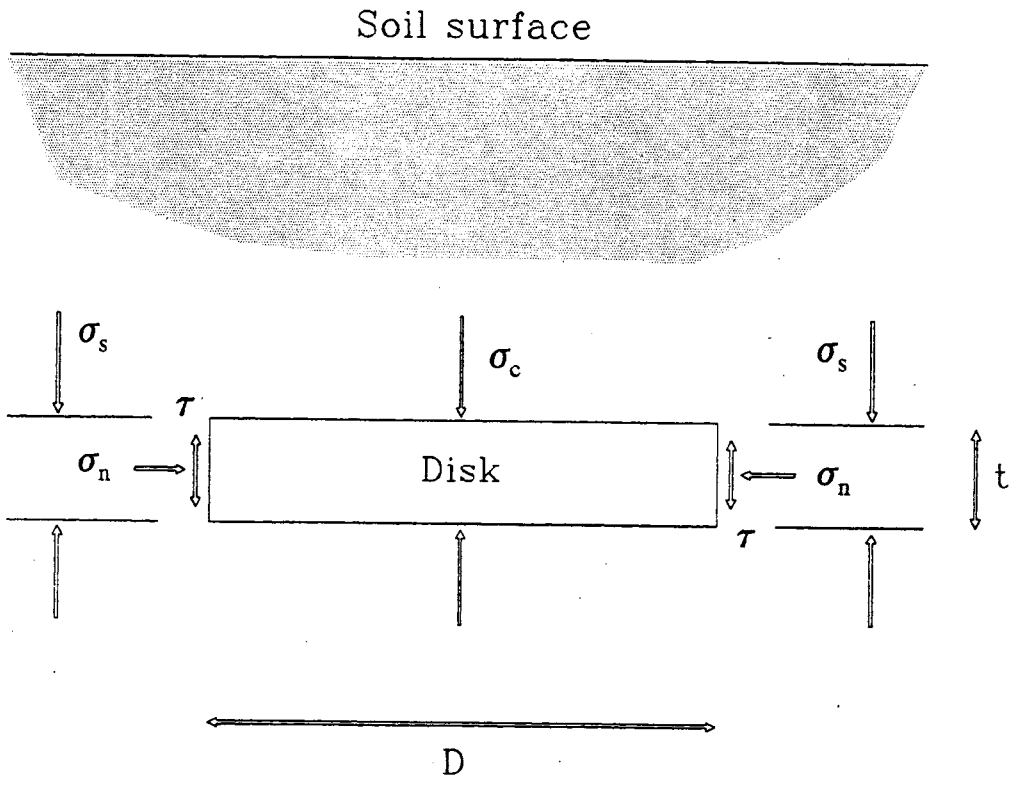

Figure 4.14. Disk inclusion subjected to frictional shearing.

parallel to the vertical disk surfaces. The relative over or under-registration is now given by

$$\sigma_e=(\sigma_c-\tau)-\sigma_s \tag{4.17}$$

The shear stress τ is assumed to be proportional to the stress acting normal to the side of the disk ($\sigma_n=\sigma_x$) and to the angle of friction for the disk/material contact

$$\tau=\sigma_n\tan\phi \tag{4.18}$$

Also, the normal stress σ_n is assumed to be proportional to the vertical free-field stress σ_s, i.e.,

$$\sigma_n=K\sigma_s \tag{4.19}$$

Where K is equal to the ratio σ_x/σ_z as in equation (4.16). The error in registration σ_e can now be expressed as

$$\sigma_e=(\sigma_c-K\tan\phi\sigma_s)-\sigma_s \tag{4.20}$$

or

$$\sigma_e=\sigma_c-\sigma_s(1+K\tan\phi) \tag{4.21}$$

The total vertical displacement of the disk δ_c is equal to

$$\delta_c=\frac{t}{2}[\frac{\sigma_c}{E_c}+\frac{K\tan\phi\sigma_s}{E_c}] \tag{4.22}$$

Using equations (4.5) and (4.7) and combining with (4.22) gives

$$\frac{D(\sigma_c-[1+K\tan\phi]\sigma_s)}{N_s}=\frac{t}{2}(\frac{\sigma_s}{E_s}-\frac{\sigma_c+K\tan\phi\sigma_s}{E_c}) \tag{4.23}$$

Rearranging the above expression yields the registration ratio

$$\frac{\sigma_c}{\sigma_s}=\frac{\frac{2D}{t}[1+K\tan\phi]+R_s[1-K\tan\phi\frac{E_s}{E_c}]}{\frac{2D}{t}+R_s\frac{E_s}{E_c}} \tag{4.24}$$

The registration ratio curves shown in Figure 4.15 were obtained from equation 4.24 with t/D=0.25, K=0.5, R_s=1.5, and values for the contact friction angle ϕ equal to 0°, 5°, 10°, and 20°, and 25°. The curve labelled "no friction" is identical to the curve shown in Figure 4.11 for t/D=0.25. From Figure 4.15 it is seen that the effect of friction at the vertical soil/disk interface is to increase the registration of the cell at low modular ratios (E_s/E_c).

For the case of an elastic disk located at an interface of two materials with different compressibility (see Figure 4.16) the formulation of an expression for the registration ratio is

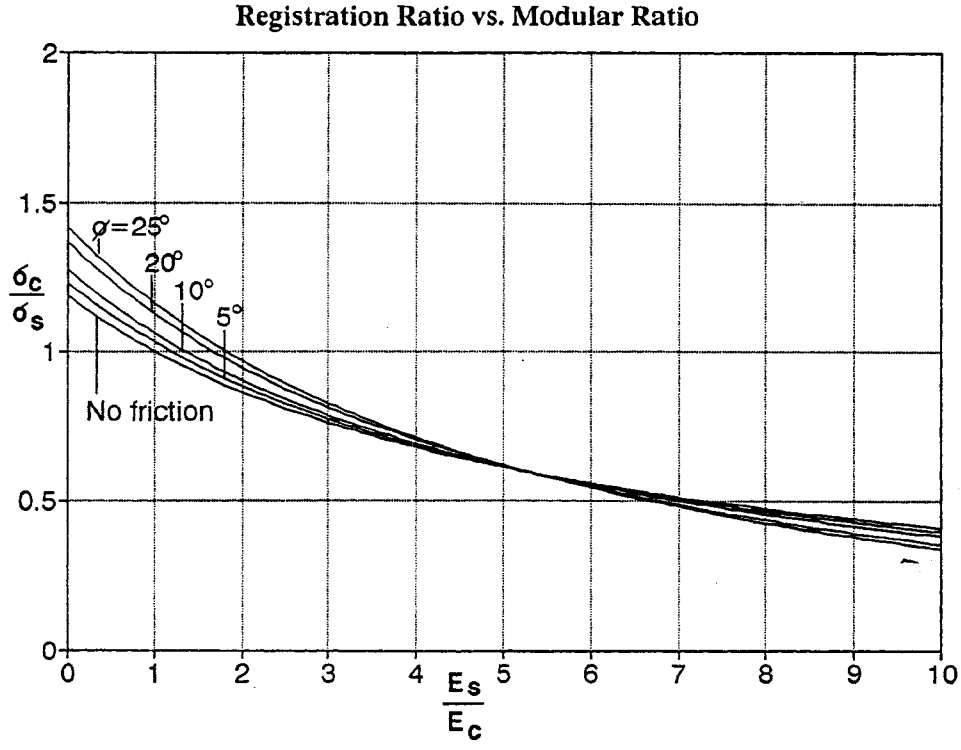

Figure 4.15. Registration ratio curves for various values of ϕ (constant t/D and R_s).

as follows. Let H_s and H_r be the embedment of the disk into the upper and lower materials, respectively. The symbols E_s, E_r, and E_c denote the Young's moduli of the upper and lower strata, and disk, respectively. The sum of the embedments must be equal to the thickness of the disk, i.e.,

$$H_s+H_r=t \tag{4.25}$$

The displacement of the disk caused by the stress σ_c corresponding to a stress change σ_s in the surrounding material is

$$2\delta_c=(\frac{\sigma_c}{E_c})t \tag{4.26}$$

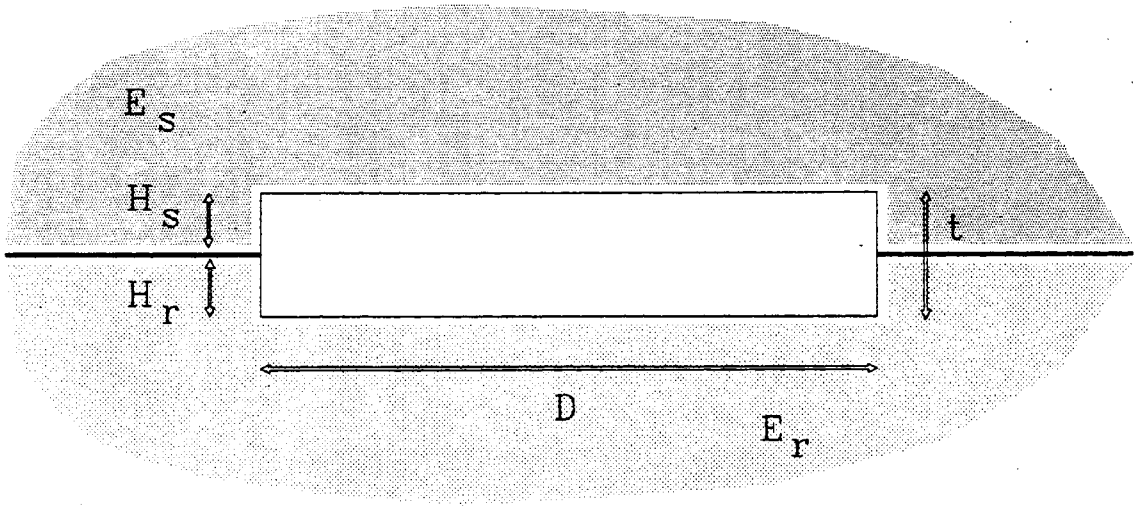

Figure 4.16. Disk-shaped inclusion situated at the interface of two different materials.

The displacement of a layer of material having thickness t is given by

$$2\delta_s = \sigma_z(1-2\nu\frac{\sigma_h}{\sigma_z})(\frac{H_s}{E_s}+\frac{H_r}{E_r}) \tag{4.27}$$

where σ_h equals the magnitude of lateral stress and σ_z is assumed to be equal to the vertical stress σ_s. The average penetration into surrounding material by the faces of the disk, δ_e, and the corresponding over or under-registration, σ_e, are given by equations (4.1) and (4.7). The net change in displacement can be expressed as

$$2\delta_e = (\frac{\sigma_e}{N_s})D+(\frac{\sigma_e}{N_r})D = \sigma_e\ D(\frac{1}{N_s}+\frac{1}{N_r}) \tag{4.28}$$

The coefficients N_s and N_r are material properties and are related to the indentation coefficient as follows

$$\frac{N_s}{E_s} = \frac{N_r}{E_r} = R_s \tag{4.29}$$

It is assumed that the above ratios are constant and equal to the indentation coefficient, R_s. Equations (4.1), (4.2), (4.5), (4.19), and (4.21) yield

$$(\sigma_c-\sigma_s)D(\frac{1}{N_s}+\frac{1}{N_r})=\sigma_s(1-2\nu\frac{\sigma_h}{\sigma_z})(\frac{H_s}{E_s}+\frac{H_r}{E_r})-\frac{\sigma_c}{E_c}\,t \tag{4.30}$$

Rearranging the above expression yields

$$\frac{\sigma_c}{\sigma_s}=\frac{\frac{1}{N_s}D(1+\frac{E_s}{E_r})+(1-2\nu\frac{\sigma_h}{\sigma_z})(H_s+\frac{E_s}{E_r}H_r)}{\frac{1}{N_s}D(1+\frac{E_s}{E_r})+tR_s\frac{E_s}{E_c}} \tag{4.31}$$

Multiplying by N_s and R_s from equation (4.21) yields the registration ratio

$$\frac{\sigma_c}{\sigma_s}=\frac{D(1+\frac{E_s}{E_r})+R_s(1-2\nu\frac{\sigma_h}{\sigma_z})(H_s+\frac{E_s}{E_r}H_r)}{D(1+\frac{E_s}{E_r})+tR_s\frac{E_s}{E_c}} \tag{4.32}$$

Plots of the registration ratio as a function of the modular ratio computed from equation (4.32) are shown in Figures 4.17 and 4.18. In Figure 4.17 curves are shown for constant $R_s=1.5$, $t/D=0.25$, $\sigma_h/\sigma_s=0.5$, $H_s/H_r=1$, and ν equal to 1/3. The modular ratio E_s/E_r is varied from 0.01 to 100. It can be seen from this Figure that the effect of a soft upper layer is to reduce the registration substantially. In Figure 4.18 curves are shown for constant $R_s=1.5$, $t/D=0.25$, $\sigma_h/\sigma_s=0.5$, $E_s/E_r=10$, and ν equal to 1/3. The embedment ratio H_s/t is varied from 0 to 1. It is apparent from these curves that, as the depth of embedment of the disk into a rigid upper layer increases from 0 to t, the registration ratio is reduced by about 25 percent and is fairly independent of the modular ratio, E_s/E_c.

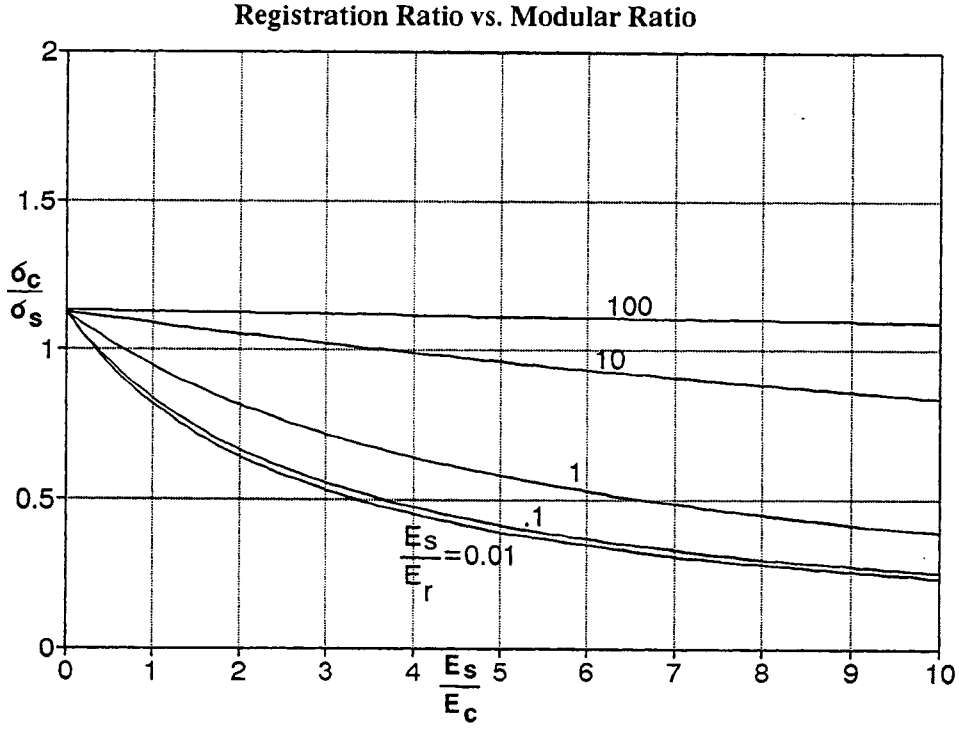

Figure 4.17. Registration ratios for varying modular ratio (E_s/E_r).

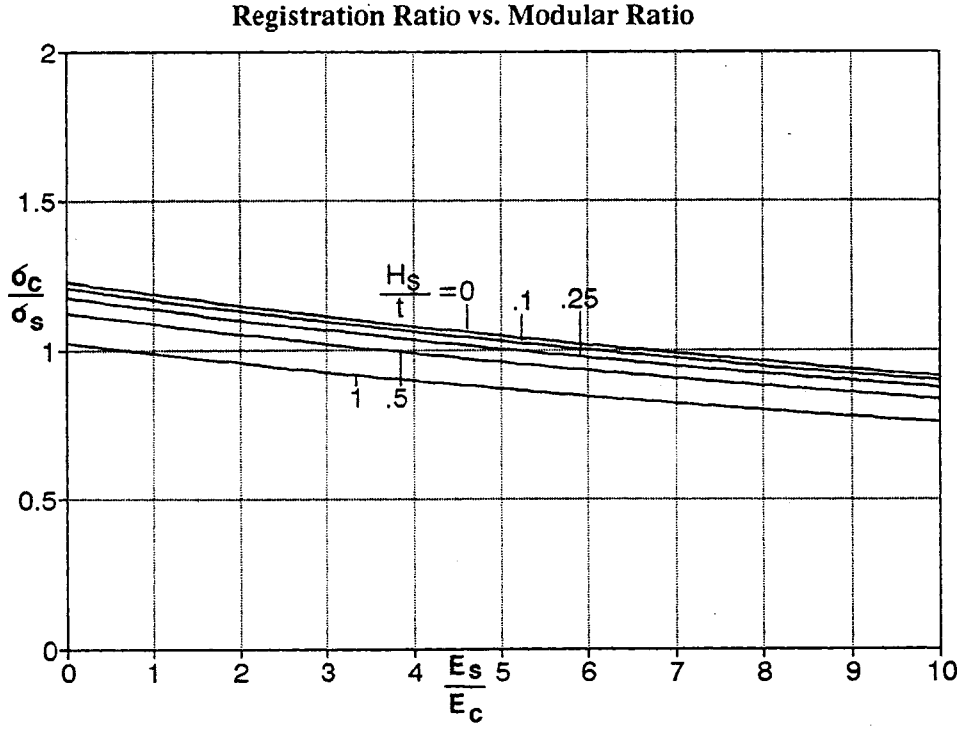

Figure 4.18. Registration ratios for varying embeddment ratio (H_s/t).

CHAPTER 5
EXPERIMENTAL RESEARCH

INTRODUCTION

The instrumentation systems at the Mn/ROAD test facility will be monitoring environmental conditions as well as pavement responses under live traffic conditions. It is important to ascertain the effects of construction, environment, and extended service periods on the transducers. Many of the transducers that may conceivably be employed at the Mn/ROAD test facility are relatively sensitive as they must respond to dynamic stresses and strains as well as small displacements. The instrumentation is critical in that the transducers must be sensitive enough to provide the desired information on pavement responses, yet possess the durability to withstand construction, climatic extremes and extended service periods under repeated heavy vehicle loads.

OBJECTIVES

This chapter of the report discusses research conducted on pavement response transducers. The investigations and research have been oriented toward the final recommendation of which types of transducers would best serve the purposes of Mn/ROAD. The objectives of this study are (1) to examine current pavement instrumentation methodologies, (2) procure a limited number of transducers and test them under various loading and environmental conditions in the laboratory, and (3) to provide a set of final recommendations of which types of transducers would best serve the purposes of Mn/ROAD. The focus is on transducers intended for determination of stress, strain, and displacement responses in a pavement system. This chapter deals with strain and displacement while the following chapter covers stress instrumentation in detail. Each section begins with a brief explanation of the reasons for monitoring a particular pavement response as well as key instrumentation issues. The transducers procured for laboratory testing are described; selection criteria and the experimental procedures that were followed in the performance evaluations are given. Detailed analysis of all laboratory test results along with recommendations are also presented.

STRAIN RESPONSE INSTRUMENTATION

In the general context of experimental stress analysis the strain gage selected for a particular application is dependent upon factors such as long-term serviceability, accuracy of the measurements, and repeatability of the results. Among the various factors that should be carefully considered in the selection of a strain gage for pavement instrumentation are the required accuracy and precision, fatigue resistance, strain magnitude, gage length, and environmental stability. The majority of commercially available strain gages are not suitable for direct embedment into bound pavement layers. There are three common methods for preparing strain transducers for installation in a pavement structure: (1) H-gages, (2) gages bonded to laboratory prepared specimens, and (3) gages bonded to material taken from the pavement. Types (1) and (2) are generally installed during construction while type (3) installations are retrofitted into the pavement system.

This section discusses laboratory testing procedures addressing the issues of accuracy and precision, gage length, and environmental stability of several different types of strain gages. Experiments were designed to test strain gage configurations intended for installation both during and after construction.

Dynatest

The Dynatest PAST 2AC is a strain transducer that is commercially available from Dynatest Consulting, Inc. These gages have been designed for the specific purpose of measuring in situ strain in pavements and as such are capable of enduring extreme environments for extended periods of time.

The active transducer is embedded in a fiberglass epoxy extrusion. This material has a relatively low stiffness, and thus, it does not interfere with, or impose constraints upon, the deformation of the pavement material. The transducer is also protected by a series of coatings and layers. These layers provide protection from failure due to mechanical and water infiltration effects as well as chemical deterioration. Fatigue life of the transducer is estimated at over 10^8 cycles. Connections to the gage are completely sealed and the provided lead-wires are Teflon insulated [6].

Kyowa

This particular strain gage is of the electrical resistance type and the active gage is situated between two acrylic resin wafers that are bonded together. The gage is most appropriate for embedment within concrete. However, a slight modification through the attachment of anchor bars at either end of the gage may make it suitable for installation in asphalt concrete layers. The complete assembly measures 120×15×4.5 mm (4.72×0.59×0.18 inches), has a gage resistance of 120 Ω, a gage factor of 2.0, and a 60 mm (2.36 inch) gage length. Its temperature range is -10°C to 70°C (15°F to 160°F). It is believed that normal temperatures experienced during the placement of asphalt lifts (280°F to 300°F) may cause failure of the gage due to its relatively lower operating temperature range. Also, at temperatures below freezing the acryl crystallizes and this may cause debonding between the acrylic wafers and gage, leaving the active gage open to moisture infiltration. The manufacturer also indicates that the heat dissipation characteristics of the Kyowa KM series gage are not as efficient as other gages and they suggest that excitation levels be kept below 3 VDC.

Tokyo Sokki

Another strain gage designed for the purposes of measuring strains in a portland cement concrete slab is the Tokyo Sokki PML-60. The gage construction and overall dimensions are similar to that of the Kyowa with the exception that the TML gage is coated with a layer of sand for the purpose of adhesion. No long-term performance data are available on this particular gage. It is to be expected that this gage can respond quite well to dynamic loads. However, the long-term reliability and performance of the transducer are under question [2].

Geokon

The Geokon VCE-4200 is a vibrating wire type strain gage designed for direct embedment in concrete. Vibrating wire strain gages have proven to be quite durable in field instrumentation programs but, they are not suitable for determination of dynamic strains [4]. This particular gage has been identified as a possible means of monitoring strains induced by volumetric changes in rigid pavement slabs.

The gage is 6 inches long and has anchor plates on either end of the housing tube to provide anchorage in the embedment material. A readout box (Geokon GK-401) must be used in conjunction with the VCE-4200 to obtain readings. The GK-401 provides the necessary voltages to "pluck" the wire; the resulting frequency is converted directly into strain units by means of an internal microprocessor. The VCE-4200 has a strain range of 3,000 microstrain, a sensitivity of ± 0.4 microstrain, and an operating temperature range of -20°C to +80°C (-4°F to 176°F). The gage also contains an internal thermistor to facilitate determination of the temperature at the gage location for the purposes of temperature correction.

Micro-Measurements

Two different Micro-Measurements strain gages were used in several of the experiments. One of the gages has a relatively long gage length (2 inches) for strain averaging in nonhomogeneous materials while the other gage has a 0.25 inch gage length. These particular strain gages are intended for general laboratory stress analysis and are not suitable for direct installation into pavement materials. The shorter length strain gage was used primarily for means of comparison of results obtained from the longer gage.

The 2-inch long strain gage is designed for applications where strain measurements are to be made on nonhomogeneous materials. With materials such as portland cement concrete or asphalt concrete a longer grid pattern is usually required to minimize the influence of localized strain fluctuations between the aggregate particles and cement. A longer strain gage averages the strains that exist over its length. This particular gage has been identified as a potential strain gage for bonding to asphalt concrete cylinders for the retrofit installation method.

LABORATORY EVALUATIONS

Stiffness tests

The relative stiffness of H-gages with respect to asphalt concrete is of primary importance in the accuracy of such installations. The Dynatest PAST transducer is designed for a longitudinal stiffness such that the gage will not overstress the surrounding material. The manufacturer specified stiffness is 24 lbf/1000 microstrain.

Two of the Dynatest strain gages procured for the lab studies were tested to determine the accuracy of the specified figure. The gages were loaded in uniaxial tension while simultaneously measuring the strain. The experimental stiffness can be determined by computing the slope of the load-strain curve, as shown in Figures 5.1 and 5.2. Results from two different

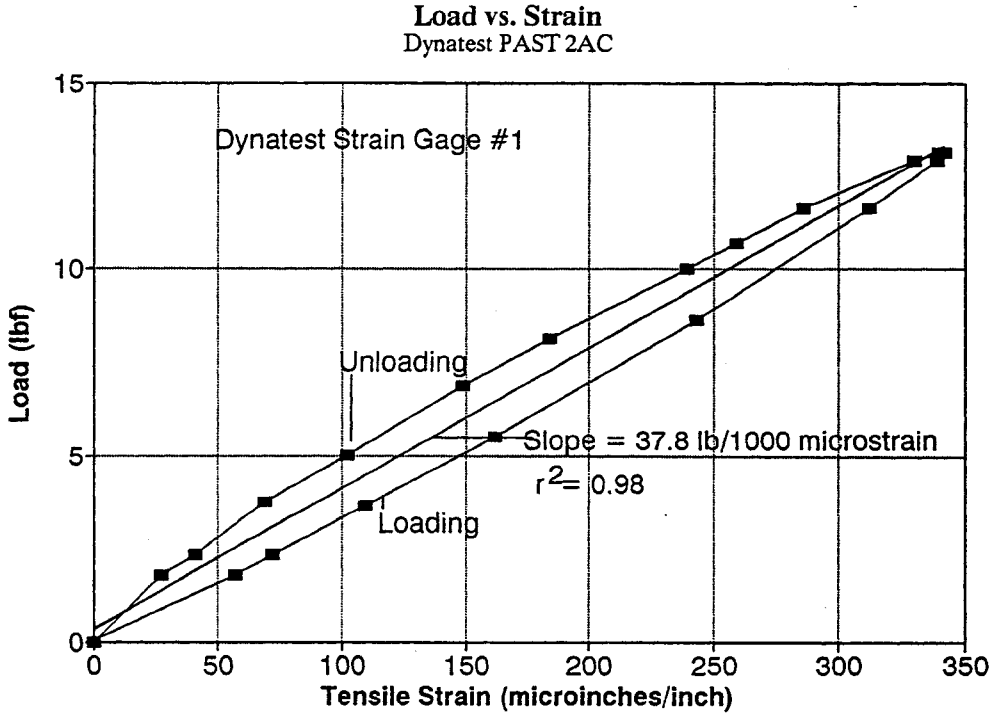

Figure 5.1. Load vs. strain relationship for Dynatest strain gage 1.

strain gages show good agreement with one another but yield stiffnesses (37.8 lbf/1000 microstrain) that are considerably higher than the manufacturer specified value. The reason for this discrepancy has not been resolved.

Steel Beam tests

Three different types of gages were adhered to the bottom of a steel I-beam for the purpose of comparing of measured strains. Dynatest, Kyowa, and Micro-Measurements strain gages were bonded to the bottom of the beam near the center. The beam is 40 inches in length, has a support of 36 inches, a span a depth of 6 inches, and a web of 4 inches. A four-point load configuration was used (see Figure 5.3). For the geometry shown, the bending moment M_b at

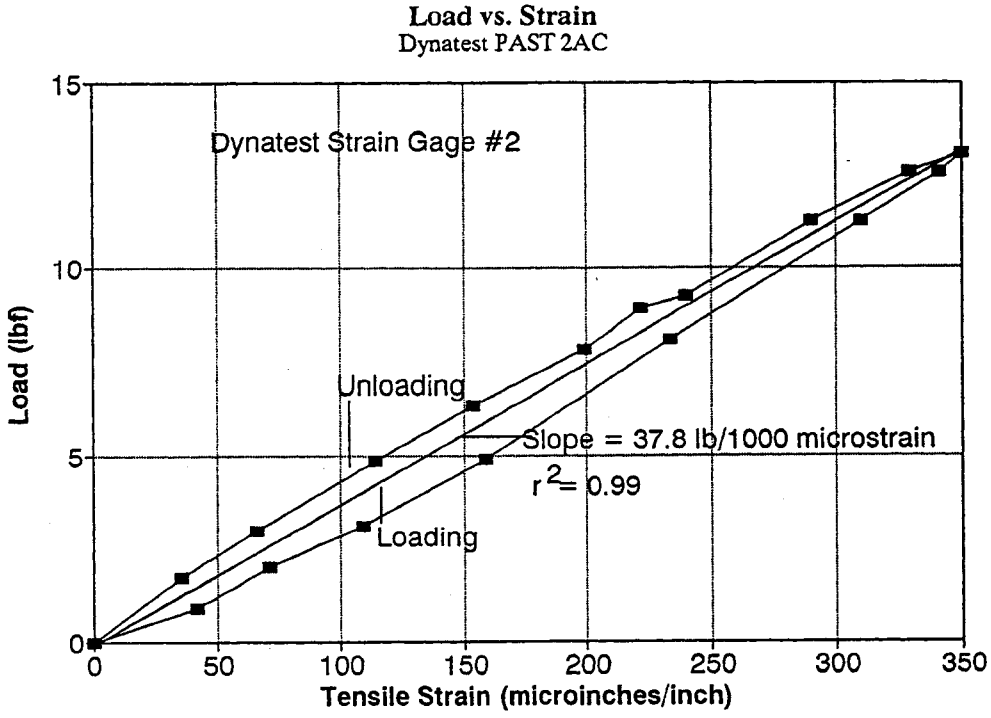

Figure 5.2. Load vs. strain relationship for Dynatest strain gage 2.

the midspan of the beam is

$$M_b = \frac{PL}{8} \tag{5.1}$$

where P and L are the applied load and span length, respectively. At the center of the beam the deflection δ is

$$\delta = \frac{11}{384}\frac{PL^3}{EI} \tag{5.2}$$

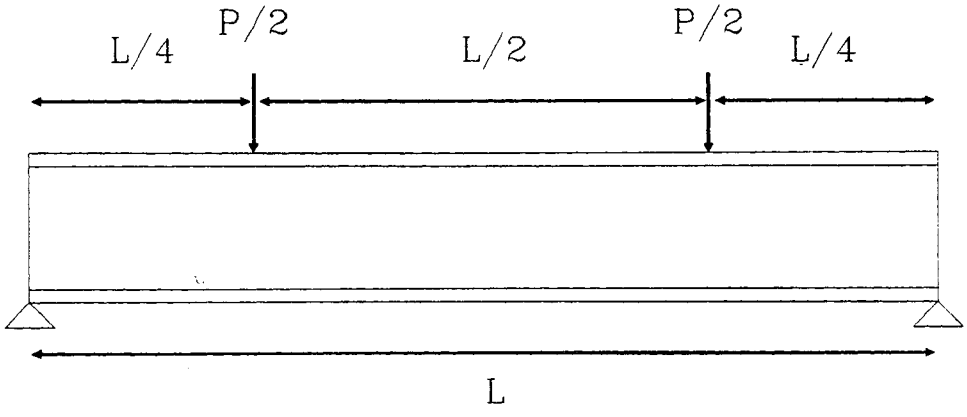

Figure 5.3. Loading configuration used for all beam tests.

where E and I are Young's modulus and the second moment of the area, respectively. Incremental loads of approximately 200 lbf were applied and strain readings were recorded using a Vishay strain indicator. Stresses in the extreme bottom fiber were computed from the load readings and measured strains were compared to strains computed from elastic beam theory. In all cases the measured strains compared well with strains computed from elasticity theory, as shown in Figure 5.4.

Concrete beam tests

For these tests concrete beams measuring $40 \times 6 \times 6$ inches were fabricated. The purpose of these tests was to examine the accuracy of the gages under static loading in the elastic range of the beam.

Concrete embedment gages were placed in the form during placement of the mix; in each instrumented beam the gage was placed at the center of the form approximately 1.5 inches above the bottom. A total of six beams were fabricated, four of which were instrumented with embedment strain gages. The remaining beams were used as preliminary tests to determine the

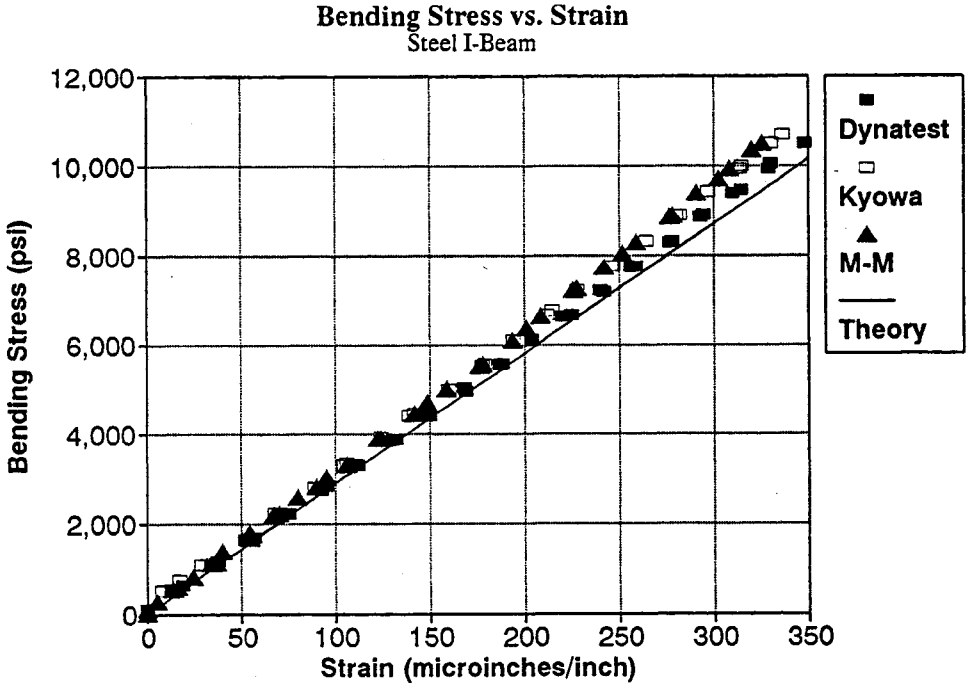

Figure 5.4. Comparison of theoretical and measured strains for steel beam tests.

flexural strength and load-deformation response of the specimens. These were used to specify loading ranges for the instrumented beams. The beams were loaded using the same test configuration as in the steel beam tests (see Figure 5.3). Two of the instrumented beams were equipped with Kyowa strain gages while Tokyo Sokki gages were placed in the others.

In addition to the embedment gages, one of the beams was prepared with a Micro-Measurements precision gage bonded to the bottom exterior of the beam. The purpose of this is to measure the strains with a gage whose performance is known and to compare the measurements with strains obtained from the embedded gage.

A typical load-displacement response from one of the plain beams is shown in Figure 5.5. The beam was loaded at a constant load rate of 40 lbf/s. Maximum loads for each of the three plain beams was approximately 4000 lbf. The center-point displacement was measured using an LVDT (Figure 5.5).

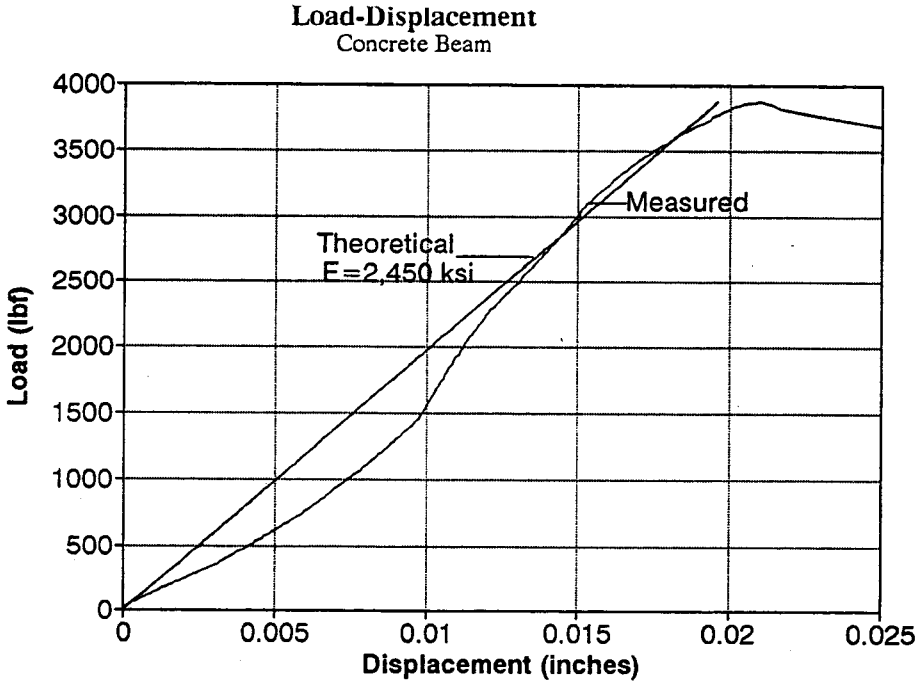

Figure 5.5. Typical load-displacement curve for concrete beams.

Each of the four instrumented beams was loaded in an manner identical to that described above. For each beam five cycles of load-unload were performed for preconditioning, three successive cycles were then performed in order to observe the stability of the gage response, and finally, the beam was loaded to failure. Typical load-displacement data for three of the four beams are shown in Figures 5.6-5.8. Applied load vs. measured strain curves for the same set of tests are shown in Figures 5.9-5.11. In these Figures strains calculated from elasticity theory are compared with the measured ones. To calculate the strain, Young's modulus was determined from the slope of the load-displacement curve, e.g., by rearranging equation (5.2). The strain gage embedded in Beam 4 exhibited large drift in the output and it was impossible to balance the strain gage bridge. Output from this strain gage was fluctuating drastically over the period of each of the load cycles. This may indicate that the gage sustained some mechanical damage during installation. For the remainder of the test beams it is seen that the measured and

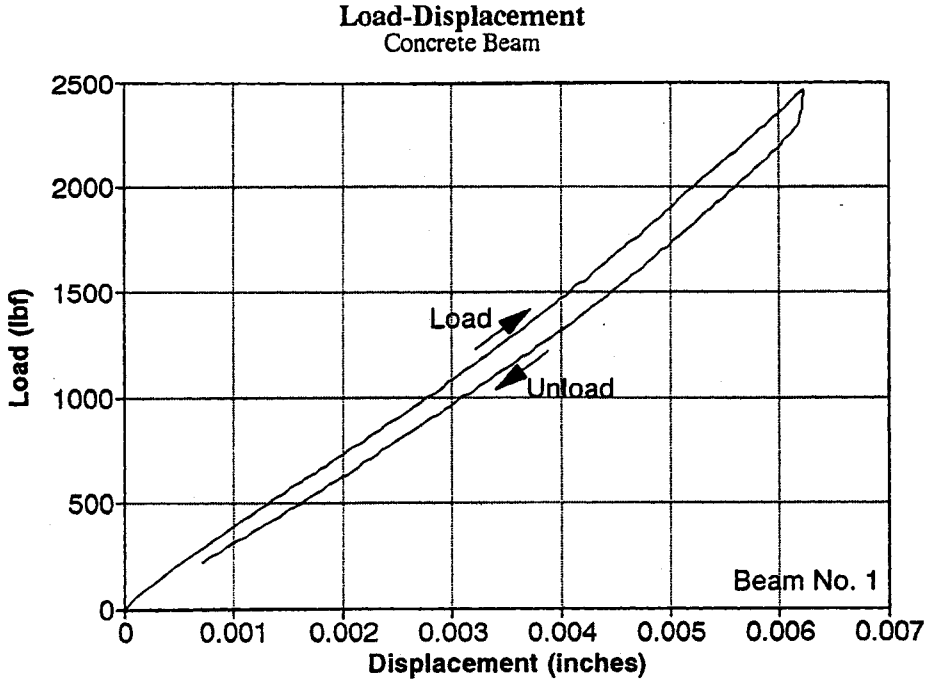

Figure 5.6. Typical load-displacement curve for concrete beams instrumented with strain gage.

theoretical strains compare well within the elastic range of the beams.

Loading tests

During the mixing operations for the concrete beams discussed above, three 6×12 inch cylinders were made from the excess mix used in casting each beam. The primary purpose of these cylinders is for unconfined compression tests to determine the compressive strength of the mix. These data were used to estimate the flexural strength and elastic modulus of the mix. In addition, one cylinder was instrumented with a Tokyo Sokki PML-60 strain gage. This cylinder was used to evaluate the accuracy of the gages under a different type of loading configuration, i.e. uniaxial compression. Two axially mounted LVDTs were used during the

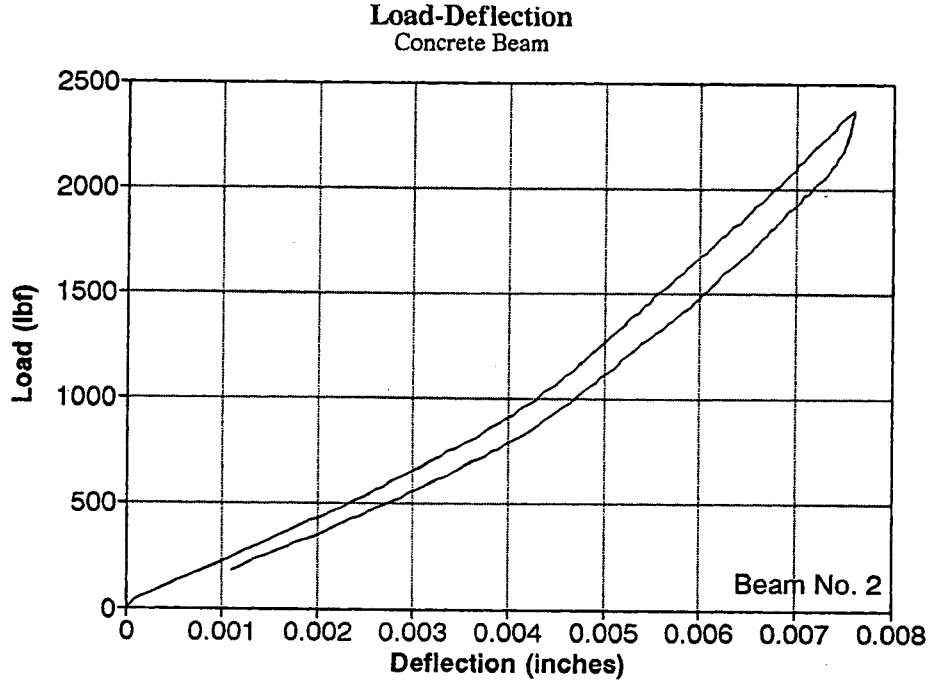

Figure 5.7. Typical load-displacement curve for concrete beams instrumented with strain gage.

experiment to facilitate computation of axial strain to compare with those measured using the strain gage. Data from one load-unload cycle is shown in Figure 5.12. It is apparent that both methods of determining the strains compare well with one another. The difference between the strain gage and LVDT-based strains is most likely due to non-uniform stress distributions within the cylinder. Note that a Young's modulus of 4×10^6 psi was assumed to calculate the theoretical strain.

Environmental effects

An experiment designed to investigate the effect of the environment (e.g., short/long-term exposure to water, etc.) on the performance of an electrical resistance strain gages was performed. A Kyowa KM-120 strain gage was immersed in a water bath and subsequently subjected to alternating cycles of freezing and thawing for approximately three months. During

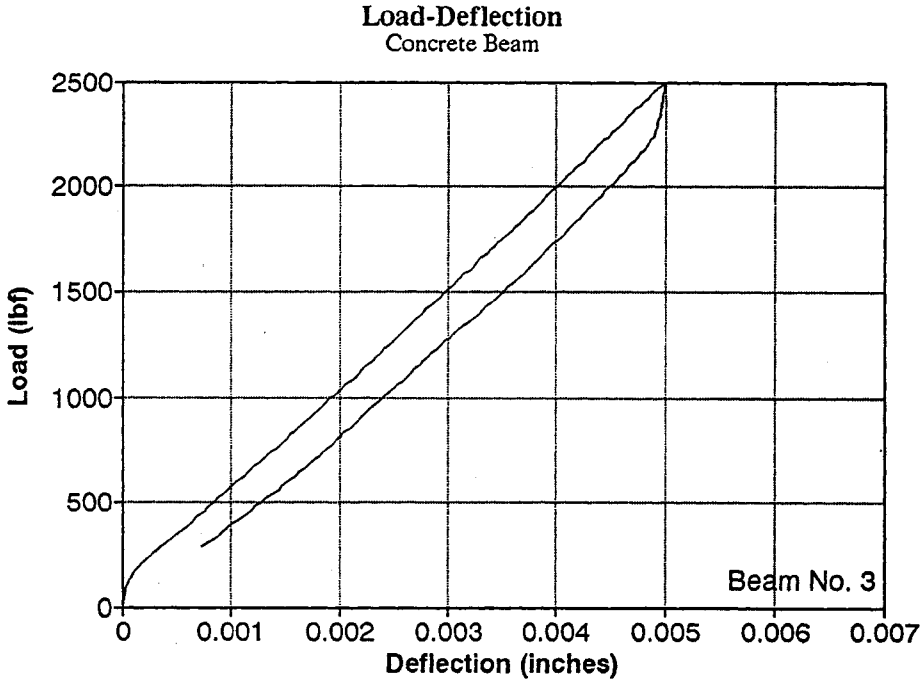

Figure 5.8. Typical load-displacement curve for concrete beams instrumented with strain gage.

this period the transducer was frozen approximately four times for periods no longer than 48 hours. The primary purpose of this experiment was to determine if long-term exposure to moisture and thermal distress have any effect on the integrity (e.g., grid resistance) of the strain gage. After the temperature cycling it was noted that the acrylic wafers had become discolored and distorted. However, no noticeable change was observed in the gage resistance. It is thought that the distortion was due to the effects of the extreme thermal distress on the acrylic material. This would not likely have had an effect on the transducer had it been embedded since the surrounding material would have constrained it.

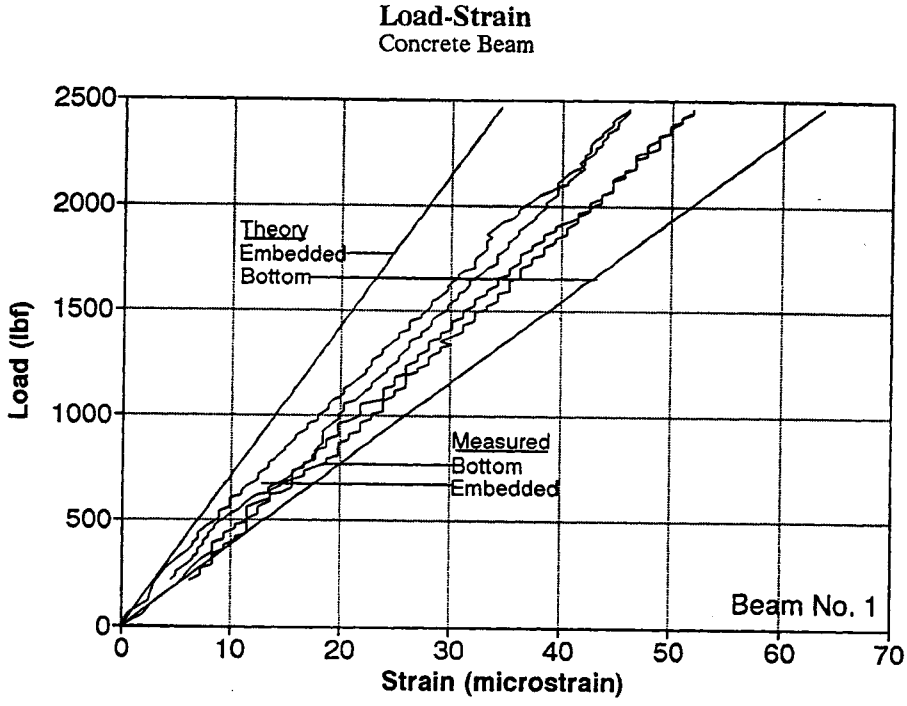

Figure 5.9. Typical stress-strain curve for concrete beams instrumented with strain gage.

DISPLACEMENT INSTRUMENTATION

LVDTs

The primary concerns in the selection of a displacement transducer are the linear displacement range and stability under environmental conditions. Hermetically sealed LVDTs are commercially available from Schaevitz Engineering. The particular LVDT selected for evaluation was the Schaevitz HPA-250. The HPA-250 is a hermetically sealed AC LVDT and is housed in a stainless steel casing. It has a linear range of ± 0.250 inches, and has shock and vibration tolerances that are presumably sufficient for long-term pavement performance monitoring. The cost of this particular transducer is warranted from the standpoint that other researchers have experienced problems with premature failure with less durable LVDTs.

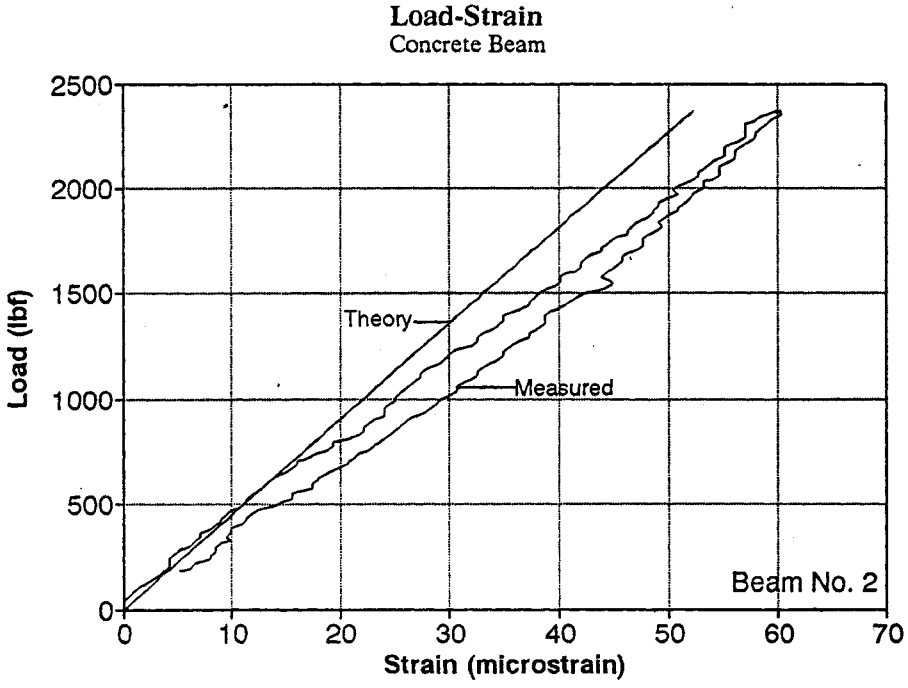

Figure 5.10. Typical stress-strain curve for concrete beams instrumented with strain gage.

LABORATORY EVALUATIONS

Calibration

Before an LVDT can be used in an application it must be calibrated. The calibration procedure is simple and involves the displacement of the core with a micrometer that has been calibrated against a known standard; the voltage output from the LVDT is correlated with the displacement obtained from the micrometer. Calibration is usually facilitated by mounting the LVDT and micrometer in a test stand. Prior to any testing all four of the LVDTs were calibrated. A typical calibration curve for an LVDT is shown below in Figure 5.13. The theoretical sensitivity of this LVDT is 1/40 inch/VDC while the sensitivity determined from a linear fit of the curve in Figure 5.13 is 1/40.035 inch/VDC. This is within the manufacturer variance of 0.25 percent.

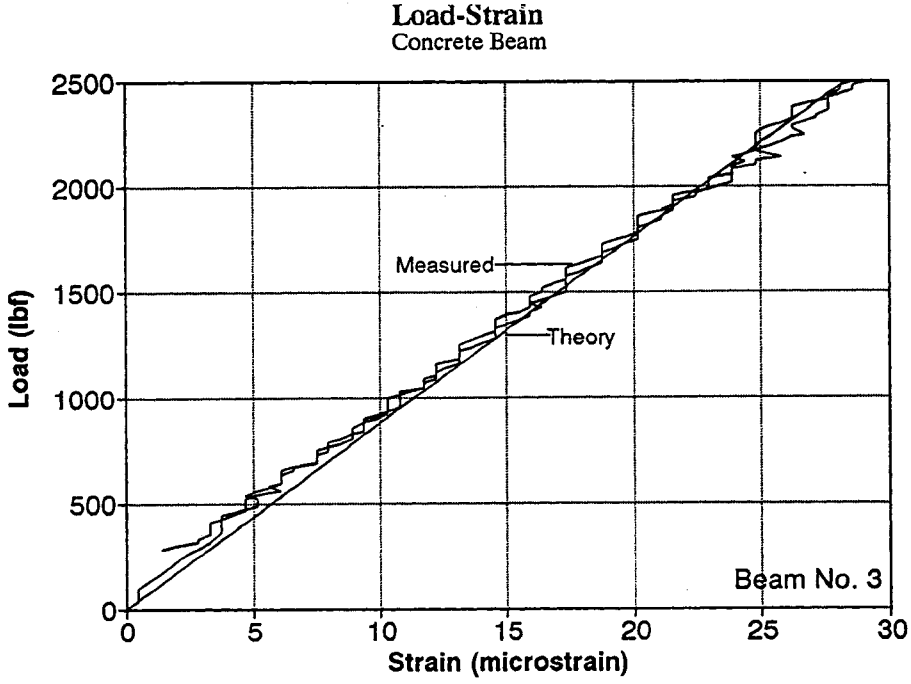

Figure 5.11. Typical stress-strain curve for concrete beams instrumented with strain gage.

Freezing tests

In this test, two of the calibrated LVDTs were immersed in a water bath and exposed to freezing temperatures for a period of about 48 hours. After this time the ice was thawed and the LVDTs were removed from the water bath and allowed to dry. Both LVDTs were immediately calibrated using a procedure identical to the initial calibrations. No differences were observed in the sensitivities, i.e. they were well within tolerance and had not changed notably since the pre-freezing calibration.

It is believed that DC operated units will better serve the purposes of Mn/ROAD primarily because no external signal conditioning is required. However, since all of the necessary circuitry for demodulation and amplification of the LVDT output are housed within the unit itself, there is concern about the effect of temperature and moisture on the sensitive circuitry of these types of LVDTs. This concern warrants the procurement of hermetically

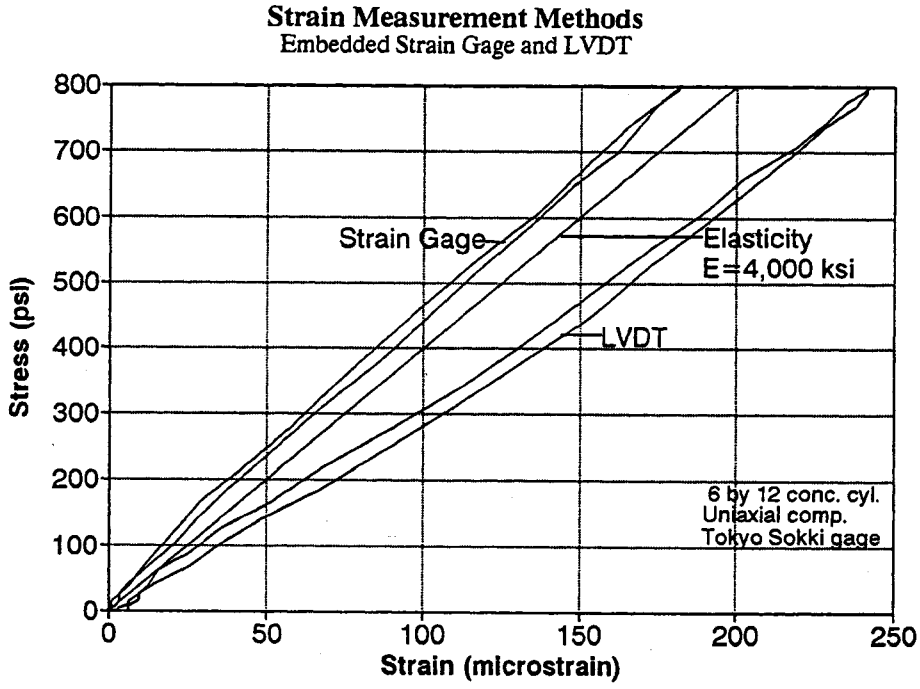

Figure 5.12. Comparison of measured strains from a uniaxial compression loading test on a concrete cylinder.

sealed DC LVDTs for use at Mn/ROAD. A test similar to that mentioned above was performed on a Schaevitz HCD-250, the DC counterpart to the HPA-250. Sensitivities determined from calibrations before and after were 1/41.576 inch/VDC and 1/41.525 inch/VDC, respectively. This particular LVDT has a manufacturer specified sensitivity of 41.675 VDC/inch. The result indicates that the DC unit is as robust as its AC counterpart for at least one freeze-thaw cycle.

Discussion

Tests conducted with various types of strain gages and strain transducers adhered to a steel beam have shown that the types of instruments to be installed within a pavement appear to have the desired levels of accuracy. The accuracy of a strain gage embedded in a heterogeneous material such as concrete, however, is difficult to assess. This is primarily due the nature of the interaction between the material and the sensor but also to the small number of replications

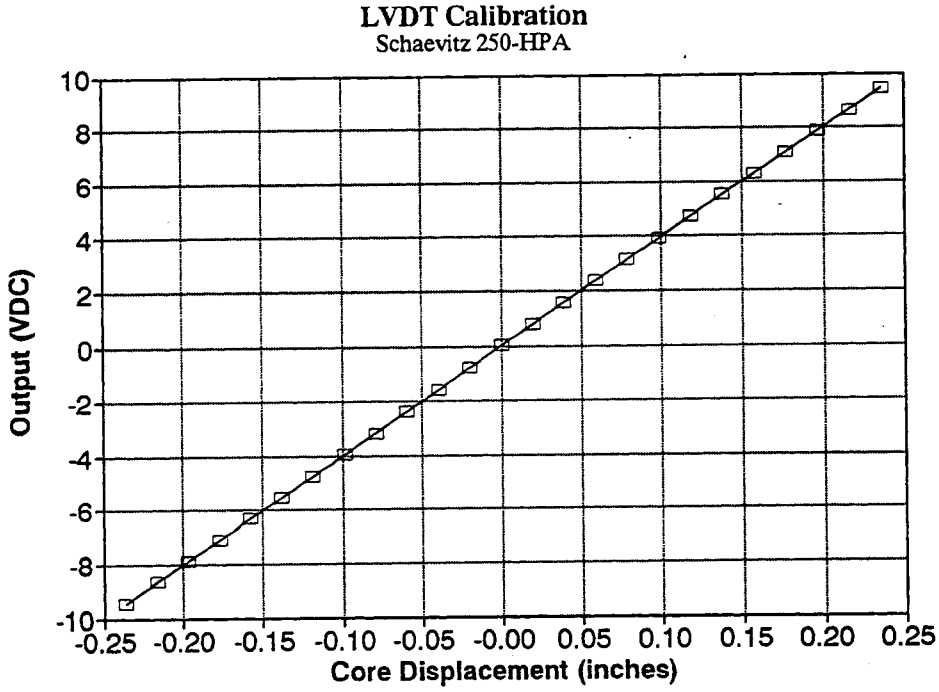

Figure 5.13. Typical calibration curve for an LVDT.

performed in this particular study. The results from beam tests appear to be satisfactory.

Environmental effects on strain gages and displacement transducers are also difficult to assess through laboratory tests. And in fact, extended field durability for certain types of susceptible transducers (e.g., strain gage based instruments) has been well documented by other researchers, as discussed in Chapters 2 through 4. The goal of these laboratory tests has not been to estimate the life of the sensors when employed in the field, but rather to screen unsuitable transducers by performing simple laboratory tests on them. From this standpoint the instruments selected for these tests appear to be satisfactory.

CHAPTER 6
STRESS CELL EXPERIMENTAL RESEARCH

STRESS CELL INSTRUMENTATION

If measurements obtained from a stress cell are to be assigned any validity, the transducer should be calibrated in a vessel, in the type of soil that it will be embedded [2,21,22]. Cell placement and installation techniques should duplicate those that will be used in the field. The goal of such laboratory procedures is to estimate correction factors that will be applied to any subsequent field results.

This chapter is divided into two sections. In the first section, results from static and dynamic loading experiments conducted on stress cells embedded in a sand are presented. Stress cell performance was evaluated by comparing the indicated stress against the expected stress in uniaxial static loading tests. The second section discusses results from dynamic loading experiments.

OBJECTIVES

The results from the static loading tests were analyzed using the indentation analogy solutions described in Chapter 4. The primary objective was to characterize the response of the stress cell as a function of the load-dependent stiffness of the soil in which it was embedded. In addition, several experiments were conducted to investigate the effects of cell location on the performance. Results indicated that (1) cell registration is a function of the geometry of the cell and the stiffness of the soil in which it is embedded, (2) the testing vessel has a substantial effect on the cell performance, and (3) the existing linear elastic indentation analogy may need to be modified to account for non-linear soil stiffness and the frictional nature of sands.

Much of the theoretical basis for pavement stress analysis and design is based upon static solutions for layered elastic systems. Since the type of loads induced in an actual pavement are dynamic, the investigation of stress cell performance under dynamic loading laboratory tests is desirable and important. The objective of the dynamic laboratory testing was to determine the nature of the stress cell response to a dynamic applied load. Results were compared to two different dynamic numerical models.

DESCRIPTION OF STRESS CELLS

Two types of stress cells were selected for laboratory testing. The Kulite 0234 (see Figure 4.4) is a commercially available diaphragm type stress cell manufactured by Kulite Semiconductor Products, Inc., Leonia, New Jersey. This transducer was selected primarily on the basis of the prohibitive costs of other commercially available stress cells. However, other researchers have had success with field instrumentation of buried pipelines using the same transducer [33]. The other cell is a Geokon Model 3500 Total Pressure Cell hydraulic type cell manufactured by Geokon Incorporated, Lebanon, New Hampshire.

The Kulite stress cell has a diameter of 2.165 inches, a thickness equal to 0.58 inches, and utilizes a solid state silicon strain gage bridge mounted on a flexible diaphragm as its sensing element. The diaphragm is situated at the center of the transducer housing behind a rigid stainless steel plate; silicone fluid fills the cavity between the diaphragm and plate. When the stainless steel plate deflects due to an applied pressure, load is transferred to the diaphragm via the silicone fluid. A rigid annulus surrounds the interior of the cell and serves to isolate the transducer from lateral stresses. All external surfaces are constructed of stainless steel. These transducers have a compensated temperature range of 0°F to +100°F and a natural frequency of 2 kHz. Kulite cells having full-scale outputs of 50 psi and 100 psi were used in the tests.

The Geokon stress cell (see Figure 6.1) is a hydraulic type stress cell. The cell has a diameter of 6 inches and a thickness equal to 0.24 inches. The sensing element, a Series PX302 pressure transducer manufactured by Omega Engineering, Inc., is housed externally at the end of a 9-inch, 0.25-inch diameter tube. As with the Kulite cell, this particular stress cell utilizes a semiconductor strain gage instrumented diaphragm. The 6-inch diaphragm is constructed by welding two stainless steel plates together. These plates are separated by a thin fluid film, which serves to transmit fluid pressures (due to applied loads on the diaphragm) to the external pressure transducer. The transducer has a range of 0 to 100 psi, a compensated temperature range of +30°F to +130°F, and a natural frequency of approximately 8 kHz. The primary advantage of this stress cell is its low aspect ratio, $t/D=0.04$, as compared to 0.28 for the Kulite cell. One disadvantage may be the fact that the rise time of the internal pressure transducer, as quoted by the manufacturer, is about 2 ms. This deficiency in the response time may make the transducer unsuitable for dynamic stress determination.

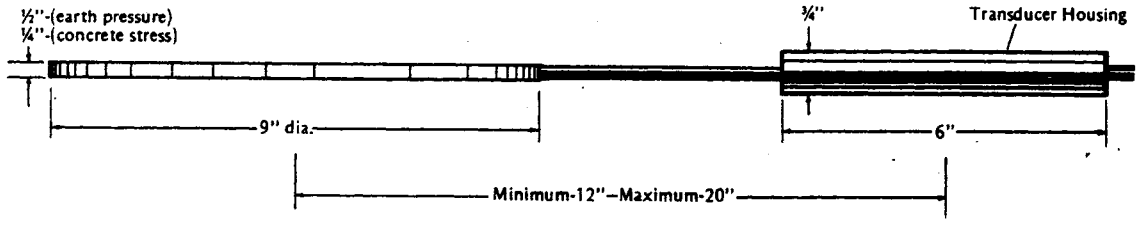

Figure 6.1. Geokon Model 3500 hydraulic soil-stress cell.

HYDROSTATIC CALIBRATION

The Kulite cells used in the investigations were calibrated under hydrostatic fluid pressure conditions. A large triaxial cell filled with silicone oil was used for the calibration procedures. The cell was placed on a plate inside the chamber with the flexible diaphragm side pointing upwards. Pressure in the chamber was initially increased to a level equal to the maximum rated pressure of the stress cell (50 psi and 100 psi) and then reduced to zero. This was performed to expel any air from the system. The procedure was repeated and cell output readings were taken at increments of 5 psi to the maximum rated pressure of the stress cell. As expected, the relation between the cell output and applied hydrostatic stress level was linear. This relationship was used in all subsequent tests with the cell embedded in soil to determine the stress indicated by the cell. Due to size constraints of the hydraulic fluid chamber, the Geokon cells could not be calibrated under hydrostatic fluid conditions. In determining the output from the cell in all subsequent tests it was assumed that (1) the sensitivity of the transducer was linear, and (2) was within the tolerances quoted by the manufacturer.

LABORATORY EXPERIMENTS

Static Loading Tests

Two types of tests have been conducted with the stress cells to evaluate performance relative to the material properties, and type of loading (static and dynamic). For the static tests a rigid cylindrical steel vessel containing soil was used as a test chamber. The sand used in the static tests was a uniformly graded sand normally used as fine aggregate in portland cement

concrete.

Experimental Setup

The tests were conducted with both one and two cells embedded in a dry sand. The testing vessel was a 3/8-inch thick wall, steel cylinder. The inner dimensions of the vessel was 14 inches in diameter and 11.5 inches deep. A cross-sectional schematic diagram and photograph of the testing vessel are shown in Figures 6.2 and 6.3. Due to the size constraints of the static testing vessel, only the Kulite cells have been tested in it. The vessel is comparable in size to calibration vessels used by other researchers [33], with the exception that no measures were taken to reduce sidewall friction. A load frame was used as the testing apparatus. The hydraulic actuator is servo-controlled and all specimen loading and data acquisition were controlled using a micro-computer. A 13.5 inch diameter, 1.5-inch thick steel platen was mounted on the cross-head of the load frame and served to provide the loading reaction; the vessel rests on a 15-inch diameter, 1.5-inch thick steel platen which was in turn mounted on the

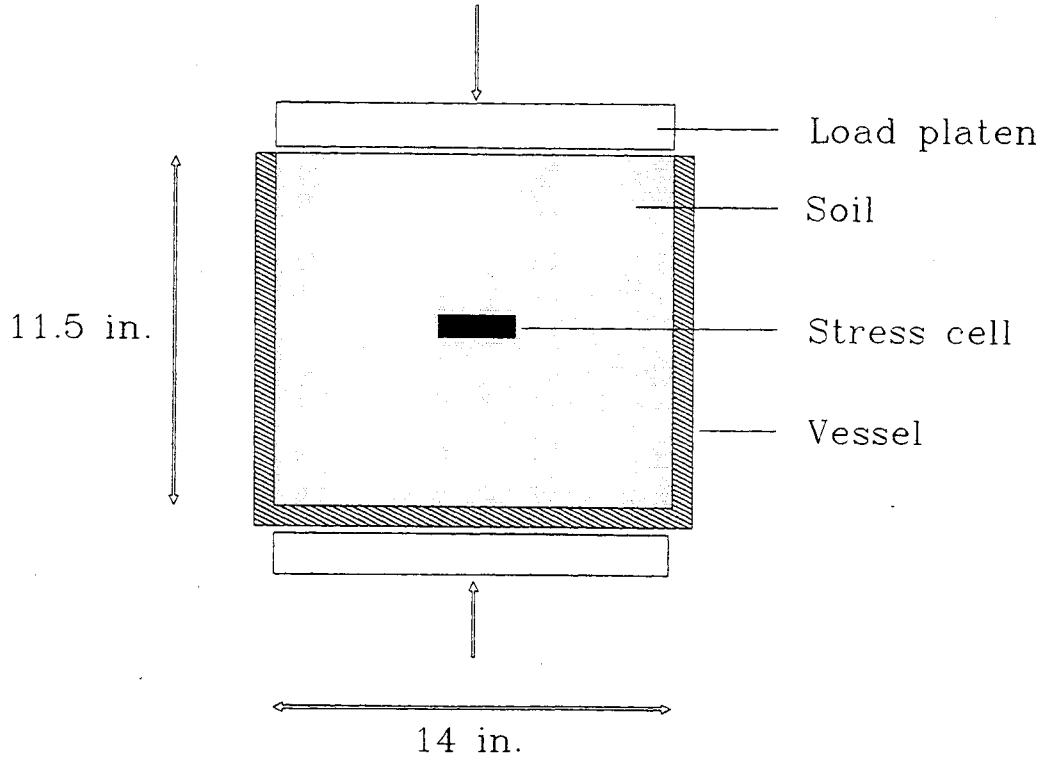

Figure 6.2. Schematic diagram of stress cell testing chamber used in static tests.

hydraulic actuator (see Figure 6.3). In all tests the specimen was loaded at a constant rate of about 500 lbf/sec. Data collected included load, vertical displacement, and stress cell output.

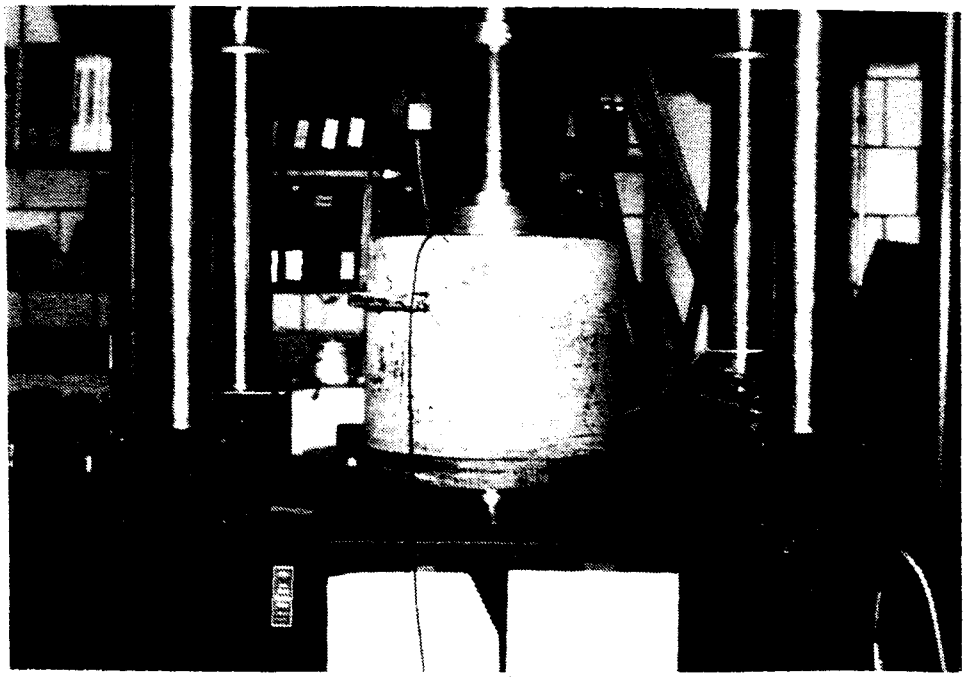

Figure 6.3. Testing system used in the static loading tests.

Procedures

Two different compaction techniques were used during the tests. A total of 8 separate specimens were prepared and tested. In all cases the set-on-surface installation method was used, as discussed in Chapter 2. The first 4 specimens were compacted using a manual technique while the remaining specimens were compacted using the load-frame.

Specimens prepared using the first method were prepared by placing lifts approximately 2-inches thick with subsequent compaction. Compaction was performed by supplying a pseudo-vibratory impulse: a large rubber mallet was used to strike the vessel at equally spaced intervals around the circumference. The lifts were placed up to the height of the desired cell depth. After 2 lifts, any pieces of aggregate larger than about 0.10 inches in diameter were removed from the area where the cell would be placed. Then, the cell was placed on a blanket of U.S. No. 40 sieved material approximately 1/4-inch thick and the stress cell output zeroed. Tests were conducted with the active face of the cell facing both upwards and downwards. In tests

where the diaphragm was facing upwards, a 0.25-inch thick layer of sieved sand was placed over the cell. After this, the remaining material was backfilled over the cell in 2 inch lifts and compacted using the same procedure as before. The remainder of the vessel was filled to the top using 2 inch lifts with compaction. The dry unit weight of the sand determined using this method was about 108 lbf/ft^3 as determined from the weight of soil and volume of the container.

The second set of specimens were prepared by filling the vessel with soil in lifts of about 2 inches. Between lifts the material was compacted by placing the vessel and soil in the load frame and applying a 10 Hz sine-shaped dynamic loading pulse for a period of approximately 1 minute. The amplitude of the load pulse used was approximately 5,000 lbf. This procedure was repeated until the soil was at a level of about 5 to 5.5 inches beneath the top of the vessel. A thin layer of sand sifted through a U.S. No. 40 sieve was placed on the surface. The cell was placed on top with the flexible diaphragm side facing upwards. Another layer of the loose sieved material was then placed around the sides and on the top of the cell. After this, the remaining material was backfilled over the cell in 2 inch lifts and compacted. The depth of cell placement was about 5 to 5.5 inches for most tests. No determination of density was made using this procedure, however, the dry unit weight using this procedure is presumably at least the same as that obtained using the first compaction procedure.

Results

The basic procedures described above were repeated a total of 8 times using the sand. A typical load-displacement (P-δ) curve for the sand is shown in Figure 6.4. These data are from a test conducted after the specimen had been conditioned by approximately 5 loading cycles. Results from all static tests are given in Appendix A.

The cell registration curve for the experiment discussed above is shown in Figure 6.5. The applied vertical stress (σ_s) and stresses indicated by the stress cell (σ_c) are plotted on the horizontal and vertical axes, respectively. The applied vertical stress values in Figure 6.5 reflect the assumption of a uniform stress distribution, i.e., σ_s=P/A, where σ_s, P, and A are the applied vertical stress, load, and cross-sectional area of the specimen, respectively. In the following analysis of these data the validity of this assumption will be discussed.

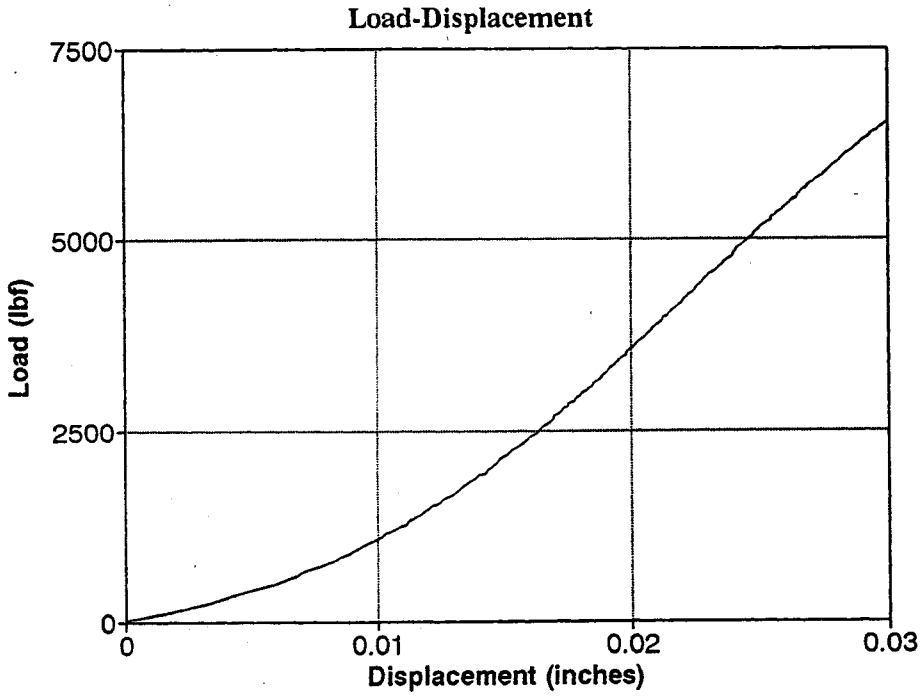

Figure 6.4. Load-displacement data for the sand: specimen S7, load cycle 5.

Several things are to be noted from Figure 6.5. While the stresses indicated by the cell correspond well with the applied vertical stress levels, the registration of the cell is decidedly nonlinear. The lower and upper branches of the curve represent loading and unloading, respectively. The degree of hysteresis for all tests was most severe for the initial loading cycle and decreased for all cycles thereafter. The hysteresis is presumably due to the fact that the material is frictional. In fact, the P-δ curve shown in Figure 6.4 resembles the curve that may be obtained by theoretical consideration of one-dimensional compression of an assemblage of equally-sized elastic spheres [21]. Observed stiffening with load cycles can be attributed to a decrease in overall voids ratio with load cycling. The effects of repeated load cycling on the specimen stress-strain response can be seen in Figure 6.6. The curves represent stress-strain data for several loading cycles on a single specimen and are obtained directly from P-δ data. Calculation of experimental stresses and strains will be discussed shortly.

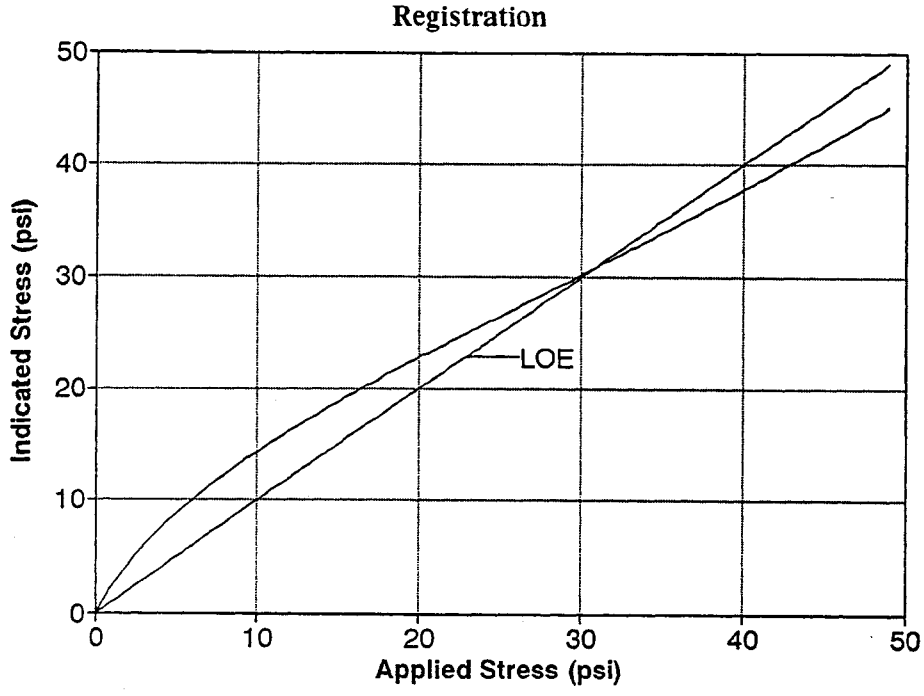

Figure 6.5. Stress cell registration data for the sand: specimen S7, load cycle 5.

The registration curves for specimen S5 are shown in Figure 6.7. It is seen that the registration at the maximum applied stress level decreased with load cycling. This effect was consistenly observed for all tests. Note also that the overall hysteresis in the cell registration decreased with the number of load cycles.

As mentioned above, the P-δ response of the specimen stabilized after several cycles of loading and unloading. In the subsequent analysis of these data, only the loading portion of the data for a given specimen and loading cycle will be considered. It is difficult to define the registration ratio, i.e., the registration ratio is not constant and changes as load levels are increased. A subsequent analysis will be performed to see whether or not this decrease in the registration is due to the increasing soil specimen stiffness response. Taylor's hypothesis as discussed in Chapter 2 will be used to analyze data from several tests.

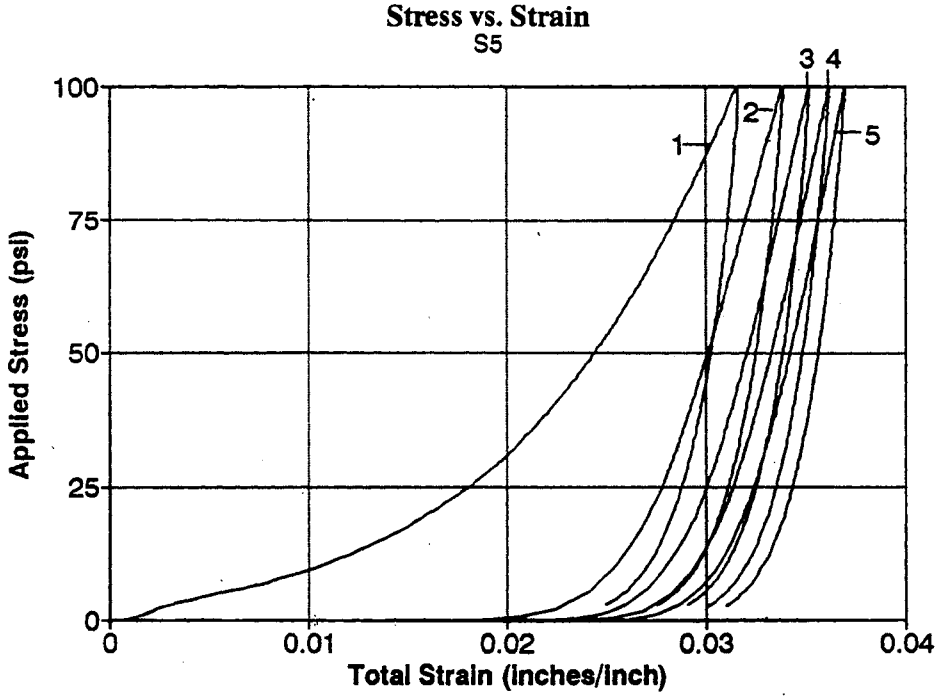

Figure 6.6. Stress-strain curves for specimen S5 during the first five loading cycles.

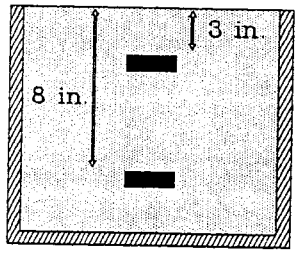

Figure 6.8. Placement locations of upper and lower cells.

In addition to the loading experiments discussed above, tests were performed to investigate the effects of the testing apparatus on the vertical stress distribution. The cell placement depths are shown in Figure 6.8. The upper cell is located 3 inches below the surface while the depth of the lower cell is 8 inches. The average registration ratio, σ_c/σ_s, for the upper

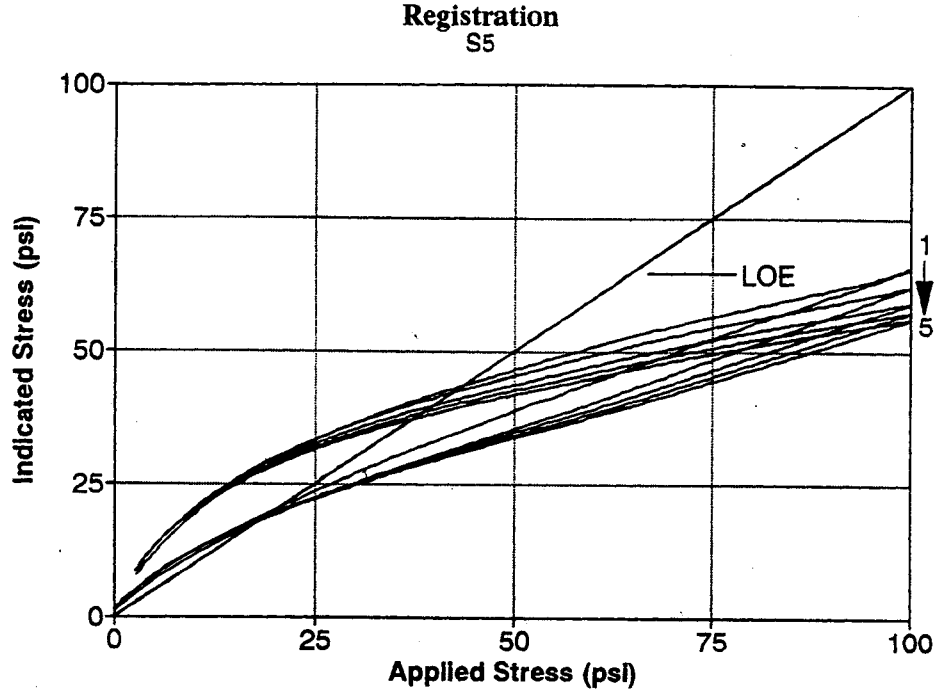

Figure 6.7. Registration curves for specimen S5 during five loading cycles.

and lower cells was 1.43 and 0.72, respectively. One possible explanation for the over-registration of the upper cell is the relatively close proximity of the loading platen. In usual geotechnical instrumentation practice it is advised to maintain a reasonable distance between the cell and any surrounding rigid boundaries [21]. Lateral displacements of the soil directly beneath the loading platen and subsequent shearing stress may cause unknown disturbances in the vertical stress distribution beneath the platen. The under-registration of the lower cell is believed to be due to a soil arching effect. This can be seen from the fact that relative vertical displacements between the soil and cylinder wall will inevitably give rise to frictional shear stresses at the soil/wall interface. Due to the development of these shear stresses the vertical stress distribution will, in general vary across the diameter of the chamber and also with depth. Thus, it can be seen that the testing apparatus has the potential of severely affecting the experimental results.

To investigate the variation of vertical stresses across the diameter and with depth, the cell placement configurations shown in Figures 6.9 and 6.10 were used. Two cells were placed horizontally beneath the surface at depths of 3 inches (Figure 6.9) and 8 inches (Figure 6.10): one cell near the chamber wall and the other at the center. The cell located near the side of the test apparatus was placed such that its edge was approximately 1 inch from the side of the chamber. The cell registration curves obtained during these two tests were quite similar to those presented thus far. Results from the tests indicate, however, that the stress directly adjacent to the cylinder wall increases with depth while the stress at the center decreases. At a depth of 3 inches the stresses determined at the side and center of the chamber were 14.4 and 51.9 psi, respectively; these measurements correspond to an applied vertical stress level of 48.6 psi. For the cells located at a depth equal to 8 inches and an applied vertical stress of 48.8 psi, the vertical stresses indicated at the side and center of the test apparatus were 31.0 and 36.8 psi. Thus, it is apparent that the indicated vertical stresses decrease with depth in the vessel. This may simply be due to increased amounts of load shifted onto the sidewall due to friction, i.e., arching. It should be noted that the above analysis does not take into account the effects of cells within close proximity of one another. It is difficult to predict the nature of these effects and in practice it is wise to maintain a considerable distance (on the order of 4 cell diameters) between two adjacent cells [2,21,22].

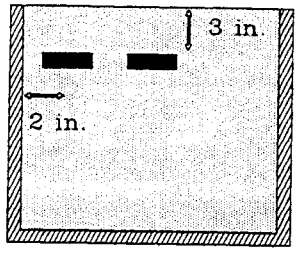

Figure 6.9. Placement locations of cells near top of vessel for stress distribution study.

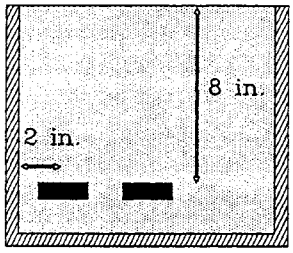

Figure 6.10. Placement locations of cells near bottom of vessel for stress distribution study.

Analysis

The primary factor affecting stress cell response that will be considered in this discussion is soil stiffness. On the basis of stiffness differences between the soil and stress cell, the stress cell output will be analyzed using indentation analogy discussed in a previous section. The particular approach used is based upon work performed by Taylor [35] and will be compared with experimental cell performance.

The stress cell response must be analyzed on the basis of expected stress at the location of cell embeddment in the testing vessel. The vertical stress distribution within the vessel may not be uniform due to the imposed boundary conditions (e.g., sidewall and platen friction) and will be attenuated with depth. For these analyses it will be assumed that the applied stresses and stress distributions within the vessel are uniform.

Experimental stress cell registration will be analyzed using an indentation analogy. The theory, originally developed by Taylor [35] and discussed in Chapter 2, is formulated on the basis of stiffness differences between the soil and stress cell. This analysis considers only vertical stresses acting normal to an elastic disk embedded in a linear elastic, isotropic body, as in Chapter 2. The assumptions discussed in Chapter 2 are applicable in the following analysis. Obviously, there exist differences between the assumed situation and the actual experimental conditions. However, this simplified approach may yield a reasonable first approximation to the problem.

To perform this analysis it is necessary to arrive at some estimate for the modulus of the material. A procedure for computing the incremental modulus directly from the experimental

data is as follows. The total soil specimen strain was computed from the displacement data, i.e.,

$$\epsilon_s = \frac{\delta H}{H_0} \tag{6.1}$$

where δH and H_0 are the incremental displacement and initial height of the soil specimen, respectively. To facilitate computation of the modulus E_s the stress-strain curve was fitted with a power curve, i.e.,

$$\sigma_s = A\epsilon_s^{\,B} \tag{6.2}$$

where A and B are regression coefficients. Assuming that the vertical stress σ_s acting on horizontal planes is the major principal stress (σ_1) and that the lateral stress σ_h is the minor principal stress (σ_3), it may be shown using Hooke's law for plane strain that the relationship between strain and stress for one-dimensional, laterally constrained compression is

$$\sigma_1 = 2G[\epsilon_1 + \frac{\nu}{1-2\nu}(\epsilon_1+\epsilon_2+\epsilon_3)]$$

where G is the shear modulus of the material and is defined as

$$G = \frac{E}{2(1+\nu)} \tag{6.4}$$

Assuming that the radial strains are zero ($\epsilon_2=\epsilon_3=0$) and that the major principal strain ϵ_1 is equal to the material specimen strain ϵ_s, equation (6.3) becomes

$$\sigma_s = E_s \frac{1-\nu}{(1+\nu)(1-2\nu)}\epsilon_s \tag{6.5}$$

For an incremental stress change and a corresponding strain increment an expression for the modulus E_s is

$$E_s = \frac{(1+\nu)(1-2\nu)}{1-\nu}\frac{\Delta\sigma_s}{\Delta\epsilon_s} \tag{6.6}$$

Using equation (6.2) an expression for the incremental slope of the experimental stress-strain curve is

$$\frac{\Delta\sigma_s}{\Delta\epsilon_s} = AB\epsilon_s^{B-1} \tag{6.7}$$

Equations (6.6) and (6.7) can then be used to compute the experimentally determined modulus of the soil specimen response.

The stress-strain and registration curves for three different specimens are shown in Figures 6.11 and 6.12. Plots of the registration ratio as a function of modular ratio (E_c/E_s) are shown in Figure 6.13. The modulus of the stress cell, based upon the average deflection of the active diaphragm (0.0001 inch) at the maximum rated pressure of the cell (50 psi), is estimated to be about 2.9×10^5 psi. The experimental curves were obtained by correlating stress cell registrations with the computed incremental soil modulus values normalized by the constant cell modulus. Theoretical curves were obtained by computing registration ratios from equations (2.10), (3.3), and (3.11) for the curves labelled "Taylor," "w/confinement," and "w/friction," respectively, using the same normalized incremental soil modulus values, E_s/E_c.

Discussion

There are several key points to mention concerning the indentation analysis used in interpreting the data. In the initial stages of loading the soil specimen response is fairly soft with increasing stiffness as load levels are increased. The cell response reflects this by over-registering in the initial loading stages with subsequent under-registration as the system stiffens.

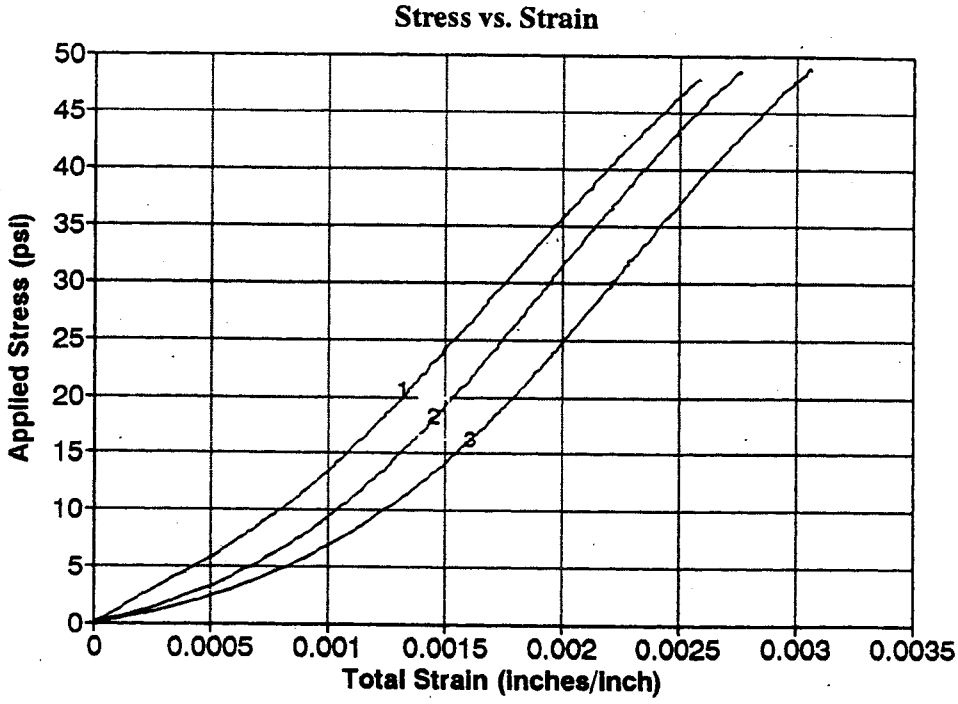

Figure 6.11. Stress-strain curves for three different sand specimens.

Registration ratios predicted from the theory do not appear to reflect the observed behavior, especially the prediction from the solution containing friction effects. The theory is, in reality, appropriate only for materials consistent with the assumptions that are implicit in linear elastic theory, but soils are not necessarily linear elastic nor homogeneous. There are many factors that the theory does not take into account such as the frictional characteristics of soil, and lateral stresses. Discrepancies between experimental and theoretical results may indicate that application of the simplified elastic analysis is inappropriate [21].

The indentation theory assumes that the faces of the disk displace uniformly. Displacements and stresses are obviously nonuniform across the face of the diaphragm-type cell used in these experiments and localized failure may occur near the edges of the cell due to the rigid annulus surrounding the active diaphragm. The effect may be to shift load either onto or away from the sensing diaphragm, but there is no way of accounting for this in the simplified

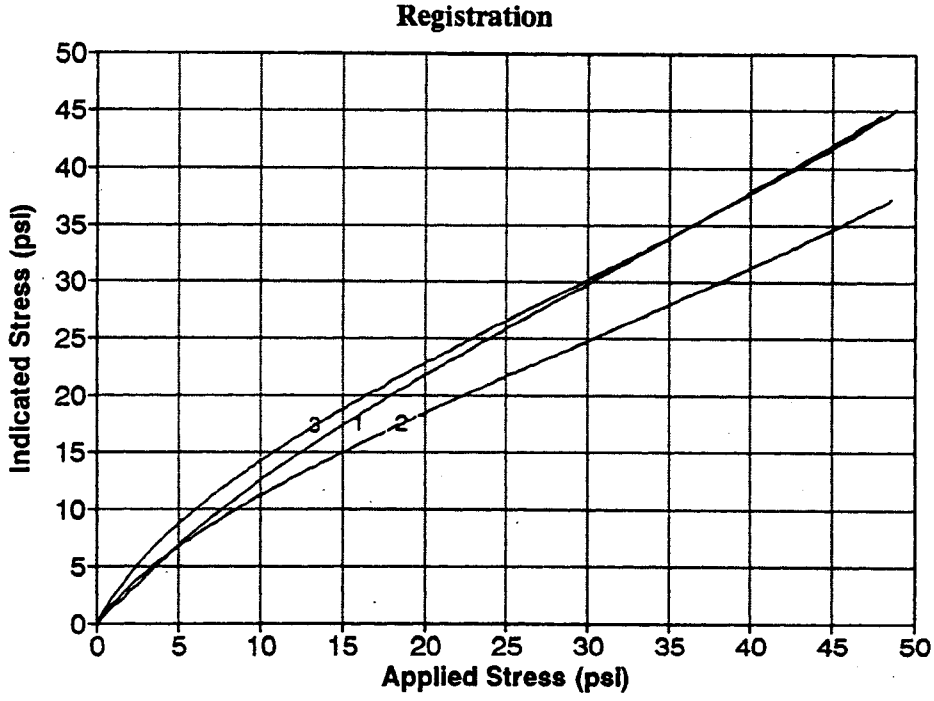

Figure 6.12. Registration curves for the three sand specimens.

analysis.

In the above analysis it was assumed that sidewall friction is not developed in the vessel. The vertical stress distribution within the vessel is most likely non-uniform due to the imposed boundary conditions (e.g., constrained radial strain and friction between the soil and vessel) and will be attenuated with depth. It is also quite likely that, due to sidewall friction, some level of arching occurs. In light of this, it may be concluded that the results shown in Figure 6.13 show that the effect of increased stress levels within the vessel is a disproportionate increase in the confining stress. The result is a decrease in the registration of the cell.

The assumption of uniform stress and strain may not be entirely valid. Displacements measured during the tests represent the overall displacement. The entire system of soil, vessel, and load-frame constitute a structural system, and there is no way to distinguish between the material response and soil-vessel-frame structural response.

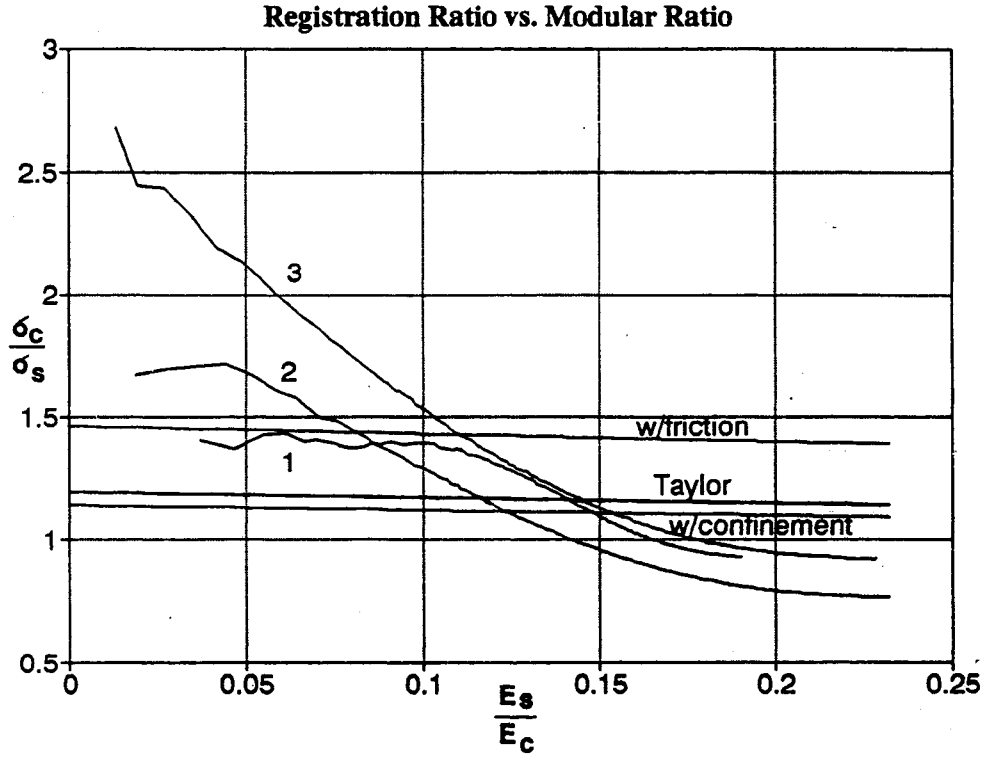

Figure 6.13. Experimental and theoretical registration ratios as a function of the soil-cell modular ratio.

In laboratory tests conducted on stress cells identical to the Kulite cell used in these experiments, Kohl noted similar hysteresis in the cell response [33]. Kohl found that the effect could be reduced substantially by using a test apparatus with slightly larger dimensions (15.3-inch diameter, 15.9-inch height) and providing a means for reducing sidewall friction.

Dynamic Loading Tests

The Kulite stress cell was also tested under dynamic conditions. In these tests, a cell was embedded in the same material in a large aggregate stock bin at various depths. A dynamic load was applied at the surface by means of a specially developed falling weight apparatus. This setup enabled the simultaneous determination of dynamic surface load and corresponding stress at the depth of the stress cell. A subsequent test used instrumentation to facilitate determination of the transient displacement of the loading platen.

Experimental Setup

As mentioned earlier, a specially designed dynamic loading apparatus was developed for the purposes of evaluating the stress cells under dynamic loading conditions. The test setup, shown in Figure 6.14, consists of an annular mass and spring. The spring is located at the base of a guide tube along which the mass travels. The entire apparatus rests on a load cell which in turn is placed on a rigid steel plate. The plate rests on the surface of the prepared soil in the large bin. Impact with the spring provides a sine-shaped impact load P(t) and can be described by the expression

$$P(t)=\sqrt{2Mghk}\ \sin\left(\sqrt{\frac{k}{m}}\,t\right) \tag{6.8}$$

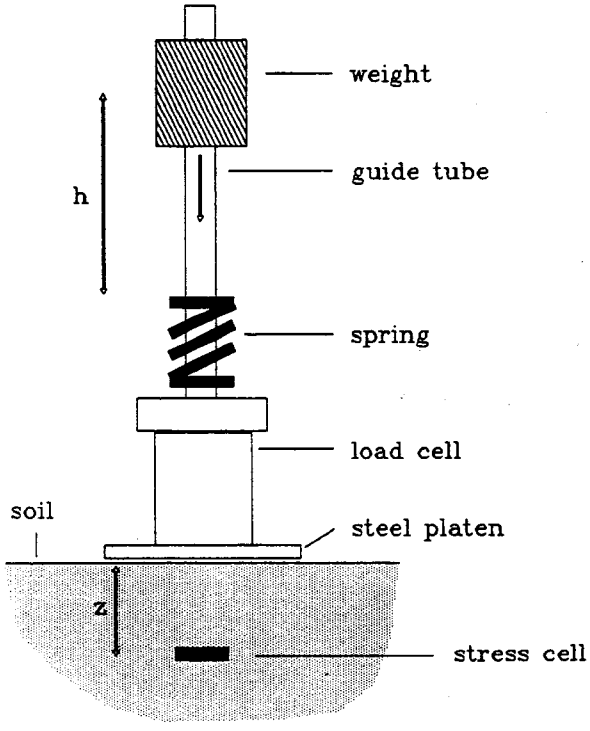

Figure 6.14. Apparatus used for dynamic loading experiments.

where M, h, k, and g are the mass of the weight, height of drop, spring stiffness, and acceleration due to gravity, respectively. Dropping the mass from various heights creates maximum load amplitudes (P_{max}) that are proportional to the square root of the drop height, mass, and spring stiffness, i.e.,

$$P_{max} = \sqrt{2Mghk} \tag{6.9}$$

Any load developed in the system must be transferred to the plate and subsequently the soil. The applied stress at the surface is taken as the load divided by the cross-sectional area of the plate. For these tests a 25 lb weight and spring having a stiffness of 1200 lb/in. were used. With these values the theoretical load frequency and loading period should be about 20 Hz and 50 ms, respectively. It should be noted that the above equations are for a spring-mass system resting on a rigid foundation. Obviously, for the actual system, there will be interaction between the loading system and soil; the observed load frequency will be different from that predicted by the equations depending on the dynamic material properties of the soil.

Procedures

The aggregate stock bin used in the tests measured approximately 46×36×36 inches and was selected so as to minimize the effects of boundaries. As mentioned earlier, compression tests in the steel cylinder were influenced by soil arching attributed to sidewall friction.

The installation method used for the dynamic tests was the set-on-surface method used in the static tests. The sand was prepared by excavating soil to approximately 5 inches below the depth of desired embeddment. Since no special compaction equipment was available the soil was compacted by placing a flexible steel plate over the soil surface and pounding on the plate with a rubber mallet. The steel plate was moved around the surface to provide uniform coverage. Prior to placement of the cell, all large pieces of aggregate were removed from the area in which the cell was to be installed. The cell was placed on top of a thin layer of No. 40 sieved material to provide uniform contact between the cell and soil. After placement of the cell, sand was backfilled in 2 inch lifts to the level of the top of the bin. After each lift the soil was compacted using the procedure described above.

The instrumentation system for the test setup in the first series of tests enabled the simultaneous measurement of output from the load and stress cells. Measuring systems in both the load and stress cells employ full Wheatstone bridges. A two channel DC conditioner was used to supply excitation to the transducers as well as amplification of the output signals. Output signals were monitored on a digital oscilloscope.

Another experiment was performed in which instrumentation was used to determine the displacement of the loading platen, as well as output from the load and stress cells. The test setup for this experiment was identical to the previous experiments with the exception of the displacement instrumentation and also data acquisition was facilitated using a portable PC equipped with a multi-channel analog/digital conversion card. For the displacement instrumentation, two LVDTs were situated at the perimeter of the loading platen 180° apart from one another. The core rod for each LVDT was fastened to the loading platen while the LVDT housings were clamped to fixtures which in turn rested on the floor near the testing bin.

As mentioned above, the dynamic experimental program consisted of two different phases. In the first series of dynamic experiments the objectives were primarily oriented towards the analysis of peak stress indicated by the cell in comparison to the peak applied stress. Five separate tests were conducted using the same cell: two tests each at two different depths. The magnitude of the applied maximum load can be varied by dropping the mass from different heights; the weight was dropped from heights ranging from 6 to 42 inches.

Results

Plots showing the typical output responses from the load, stress, and displacement transducers are shown in Figures 6.15 through 6.17. As mentioned above, for the first five tests only the maximum applied and indicated stresses were recorded. The height of drop was increased by an increment of 6 inches for drop heights ranging from 6 to 42 inches and the weight was dropped a total of five times from each height. The results from one of the five tests conducted with the cell located at a 6.5-inch depth is presented in Figure 6.18. Maximum indicated stresses for each drop have been plotted against the corresponding maximum applied stresses. Maximum applied stresses were computed by assuming a uniform distribution of load. Referring to Figure 6.18, there appears to be a linear relationship between applied stress level and indicated stress levels for each depth.

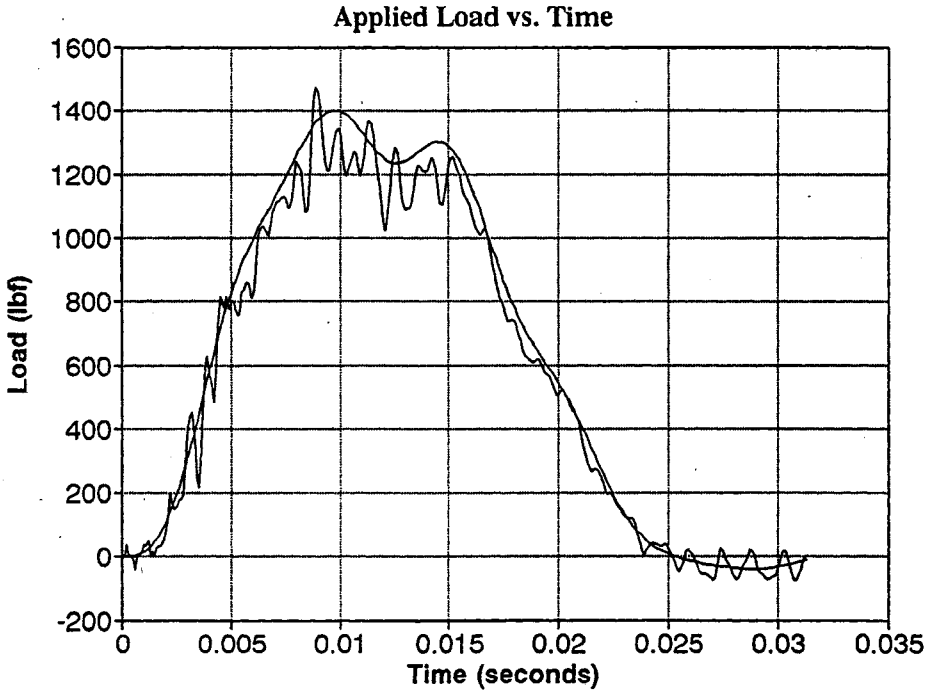

Figure 6.15. Typical response from the load cell during dynamic loading tests.

Analysis

The solid line in Figure 6.18 represents a best fit linear regression line, i.e.,

$$\sigma_{c,\max} = m\sigma_{s,\max} + b \tag{6.10}$$

where m and b are regression coefficients. Table 6.1 summarizes the results of these analyses for all five tests. The r^2 coefficient from these fitted lines ranged between 0.75 and 0.97 indicating a relatively satisfactory degree of fit.

Strictly speaking, the results should be analyzed using a dynamic analysis. Lamb's classical solution [37] describes the propagation of dynamic disturbances due to a concentrated point load within an elastic half-space and Stam [38] has obtained a solution to the dynamic distributed surface load problem. However, these solutions, even though they are closed-form

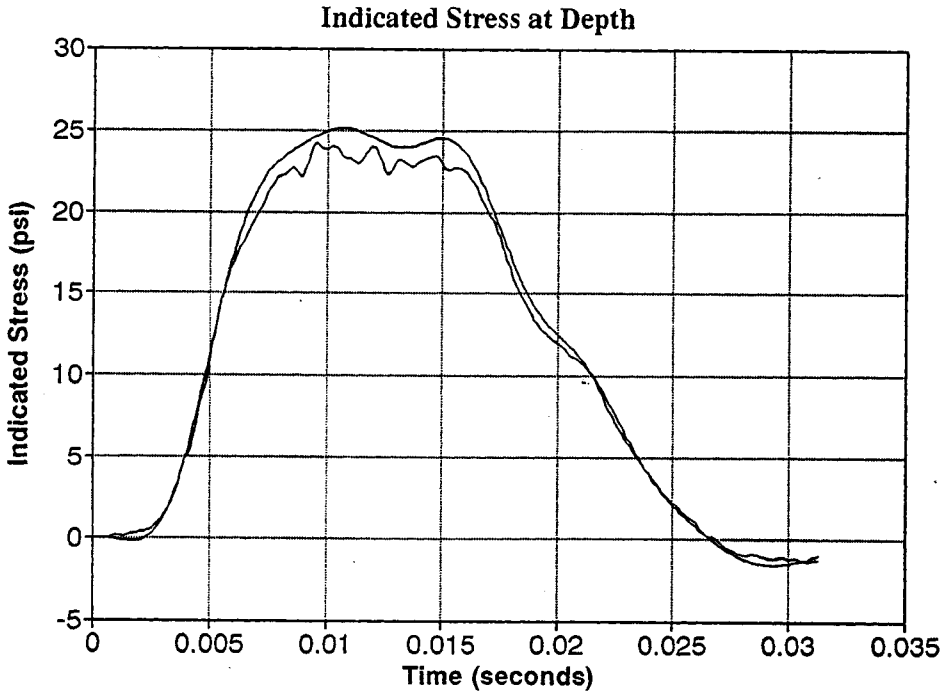

Figure 6.16. Typical output response from the stress cell during dynamic loading tests.

Table 6.1. Regression results for dynamic loading experiments.

Test	Depth (in.)	Slope	Y-intercept
1	6.5	0.54	-1.22
2	3.5	0.74	-0.17
3	6.5	0.41	-0.44
4	3.5	1.20	-3.15
5	6.3	0.43	0.22

solutions, require extensive numerical analysis. For this reason a dynamic finite element method (FEM) analysis of this problem was undertaken.

A three-dimensional dynamic (FEM) solution has been developed for the purposes of

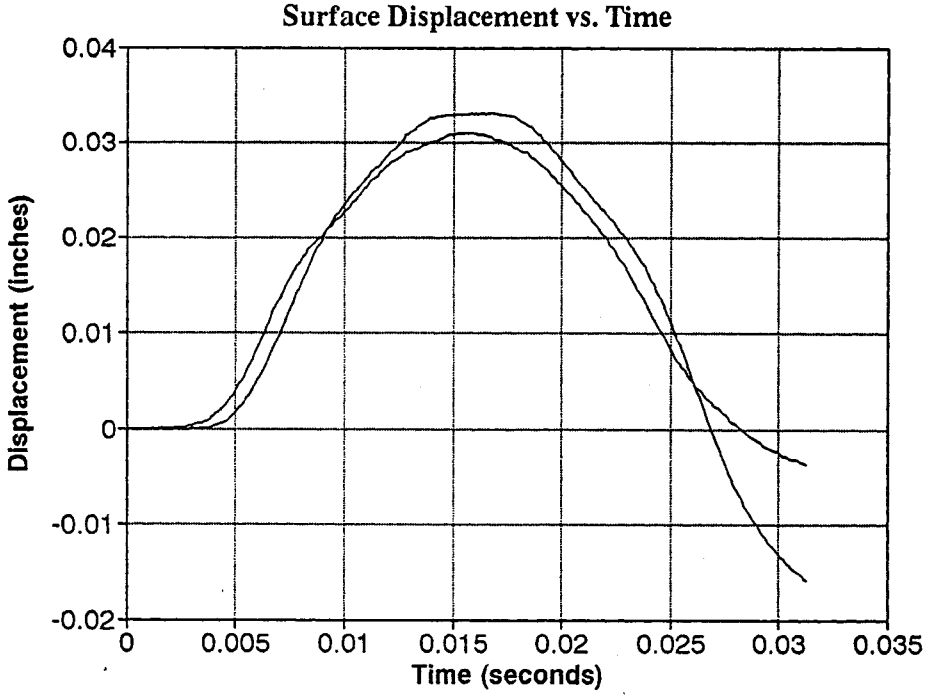

Figure 6.17. Typical output response from the displacement transducers (LVDTs) during the dynamic loading tests.

modelling pavement responses under realistic loading cases [24]. The program, **MNROAD**, is a three-dimensional, linear elastic, dynamic FEM code. **MNROAD** was used to provide an estimate of the stresses induced within the domain due to the application of a transient surface load.

A schematic diagram of the domain modelled using **MNROAD** is shown in Figure 6.19. Utilizing symmetry, only a quarter of the domain was discretized to obtain the solution. Two different runs were made using this analysis model in which results from two different experiments were used for the surface loading conditions; these applied load curves are taken from Tests 2 and 21 of the second series of dynamic loading experiments. To save computational time, the boundary loading conditions for each case were modelled using a tri-linear loading ramp. For the case of Test 2 this curve is shown as a solid line labelled "z=0"

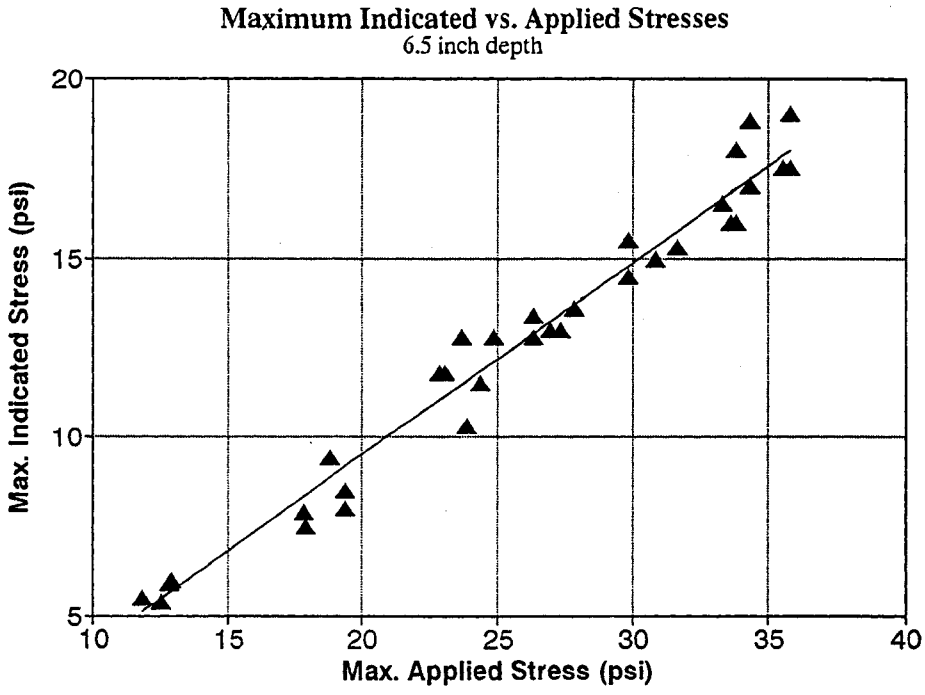

Figure 6.18. Plot of max. indicated stresses vs. max. applied stresses for test with cell buried at 6.5 inches.

in Figure 6.21.

As shown in Figure 6.19 the loaded area was represented by a square area. The dimensions of this square were such that the area is equal to the area of the 8-inch diameter platen used in the experiments. A comparison was made of the difference between the vertical stress distribution due to a circular or square loaded area. The solution for a circular load is given by the theory of Boussinesq [36]:

$$\sigma_z = q\left[1-\frac{z^3}{(a^2+z^2)^{3/2}}\right] \tag{6.11}$$

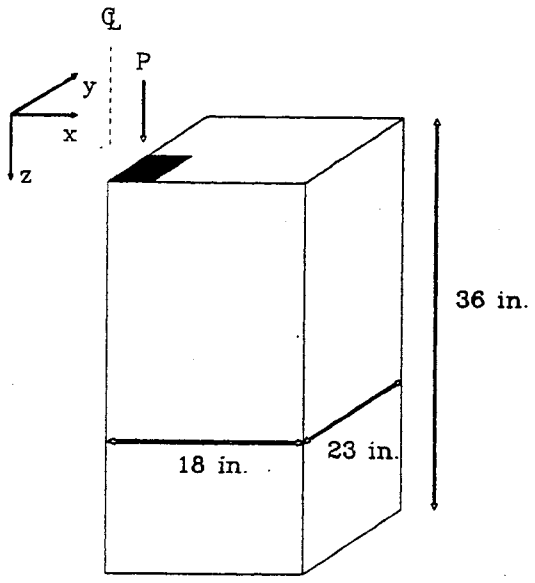

Figure 6.19. Domain used for discretization in dynamic FEM analysis.

and the solution for a square loaded area is [40]

$$\sigma_z = \frac{q}{2\pi}\left[\tan^{-1}\left(\frac{4a^2}{zR_2}\right) + \frac{8a^2 z}{R_2 R_1^2}\right]$$
$$R_1 = \sqrt{4a^2+z^2} \qquad (6.12)$$
$$R_2 = \sqrt{8a^2+z^2}$$

A comparison of the circular Boussinesq distribution of vertical stresses and the distribution due to a square load is shown in Figure 6.21. For shallow depths the difference between the two solutions is small. Input values for Young's modulus, Poisson's ratio, and the unit weight of the material were specified to be 7,500 psi, 0.4, and 100 lb/ft^3, respectively. With these input parameters the velocity of the longitudinal (V_p) and transverse waves (V_s) are 7,080 in./sec and 4,230 in./sec. Rigid boundaries were used to model the boundary conditions although the effect of the boundaries in the experimental apparatus may be in question.

Results from the FEM analysis of tests 2 and 21 are shown in Figures 6.21 through 6.23. These plots show the vertical stress increases (σ_{zz}) as a function of time at depths of 3.5 and 9.3

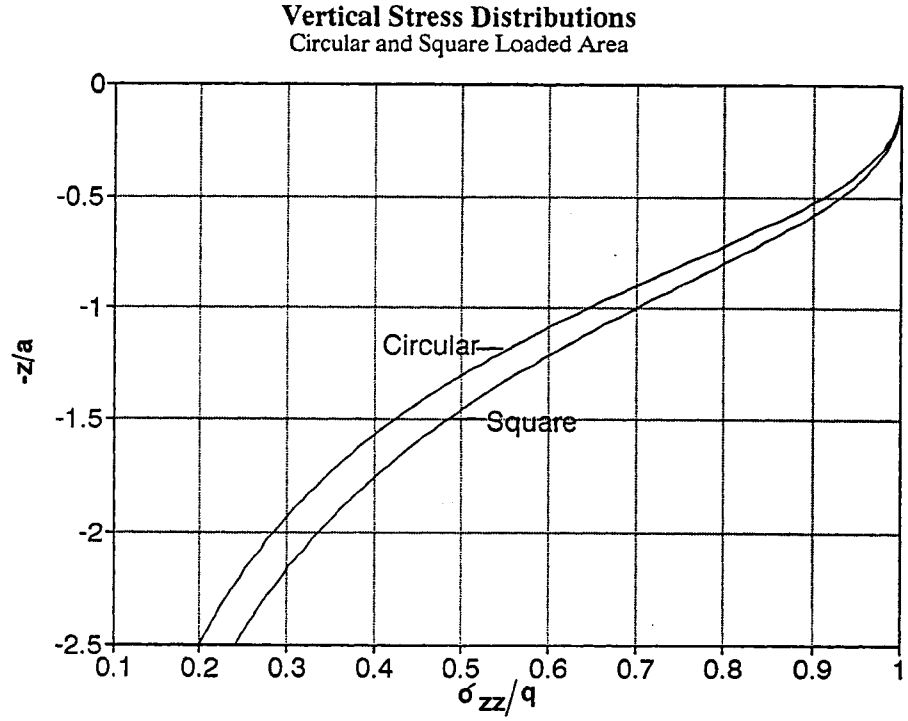

Figure 6.20. Comparison of stress distributions for circular and square distributed loads.

inches. These points represent depths at elemental numerical integration points directly beneath the center of the loaded area. Direct comparisons of experimental and numerical results for the two tests are given in Figures 6.22 for stress and Figure 6.23 for displacement. Unfortunately, for these series of tests the stress cell was embedded at a depth of about 6.3 inches and stresses in the FEM analysis were computed at depths of 3.5 and 9.3 inches. It can be seen from Figure 6.22 that stresses indicated at a 6.3-inch depth were substantially higher than stresses compute numerically at a depth of 3.5 inches.

A comparison of surface displacements is given in Figure 6.23. During the experiments it was noted that for consistent drop heights (maximum loads) it was difficult to obtain consistent displacements. Due to eccentricity in the loading displacements obtained from each LVDT were not equal indicating that some rotation of the apparatus was taking place during impact.

For comparative purposes, an analysis has been performed using a dynamic BEM

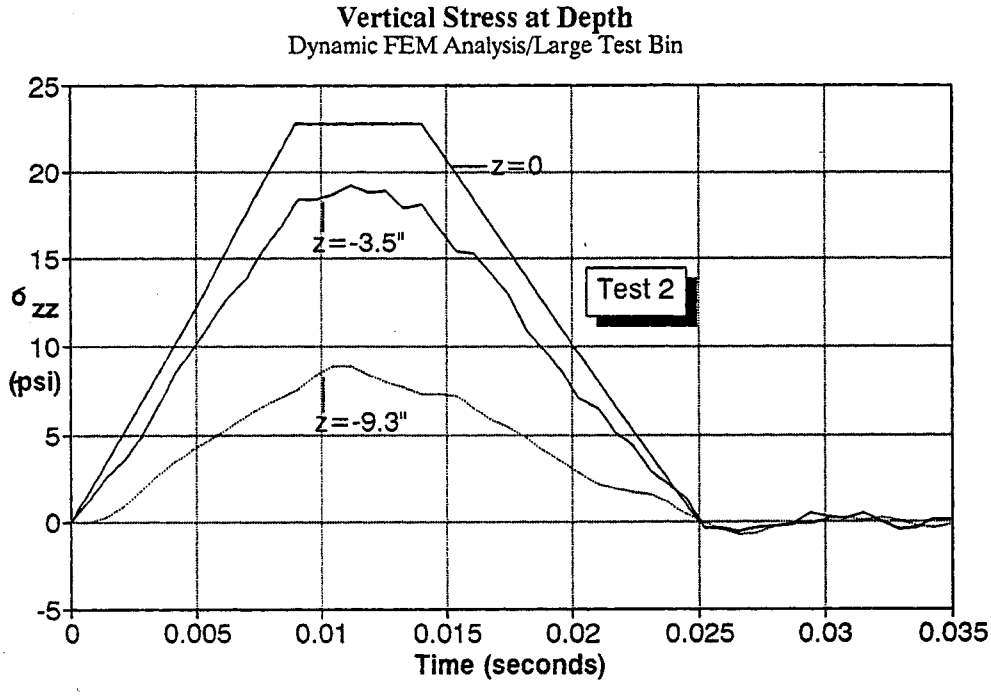

Figure 6.21. Results from FEM analysis of Test 2.

solution. The code utilized in this analysis was actually developed for the purposes of modelling stability of underground mining stopes under dynamic loads, such as seismic events or blast-induced disturbances [41]. The primary difference between the methods is that only the boundary of the domain of interest need be discretized using boundary elements. Thus, boundary conditions at infinity are more realistically represented as there is no need for viscous damping to model them. The primary disadvantage of this approach is that the rigid boundaries of the testing apparatus cannot be modelled.

The problem under question is shown in Figure 6.24. Note that the BEM solution is a two-dimensional representation and conditions of plane-strain are assumed. A transient, half-sine shaped boundary loading condition, p(t), was specified along the surface $y=0$, $-4 \leq x \leq 4$, i.e.,

$$p(t) = p_0 \sin(\omega t) \tag{6.13}$$

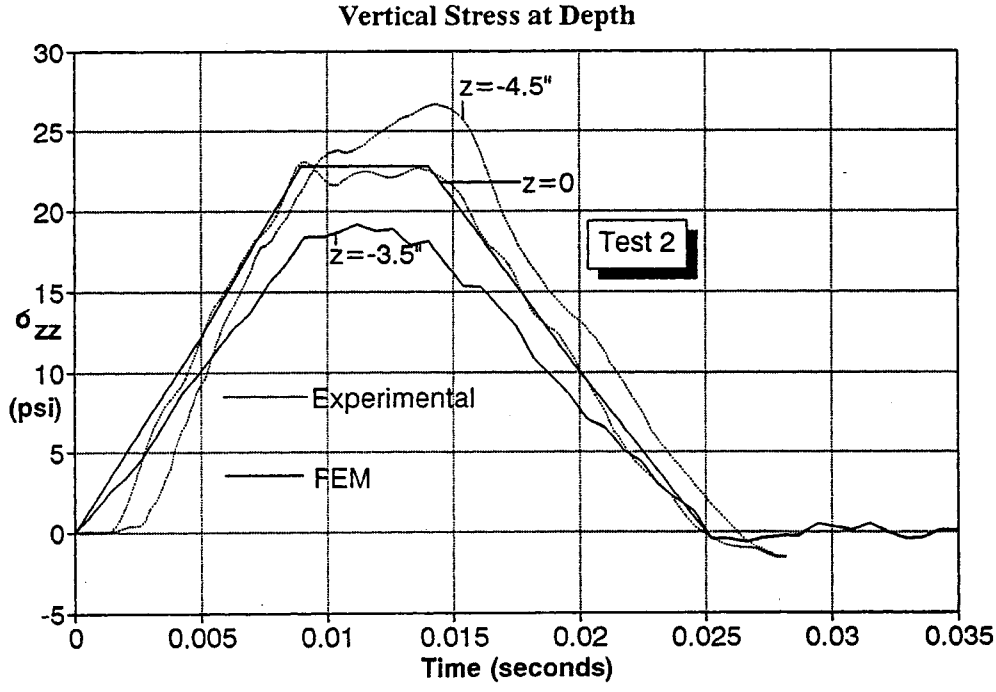

Figure 6.22. Comparison of vertical stresses for Test 2.

The frequency of the loading pulse was 25 Hz and material constants were identical to those specified in the FEM analysis. Although this algorithm is formulated for a full-space, it is possible to model a half-space by extending traction-free elements out past the loaded portion of the boundary, as indicated in Figure 6.24.

Results from the BEM analysis are shown below in Figure 6.25. Vertical stresses (σ_{zz}) were computed at a depth of 6 inches below the center of the loaded strip. The vertical stress components, as a ratio of the maximum applied stress, is shown as a function of time. From Figure 6.25 it can be seen that the maximum stress at a depth of 6 inches is about 70 percent of the peak applied stress.

A summary of results from the dynamic experiments and related analyses are given in Table 6.2: registration ratios in terms of the peak applied stresses for the experimental data and

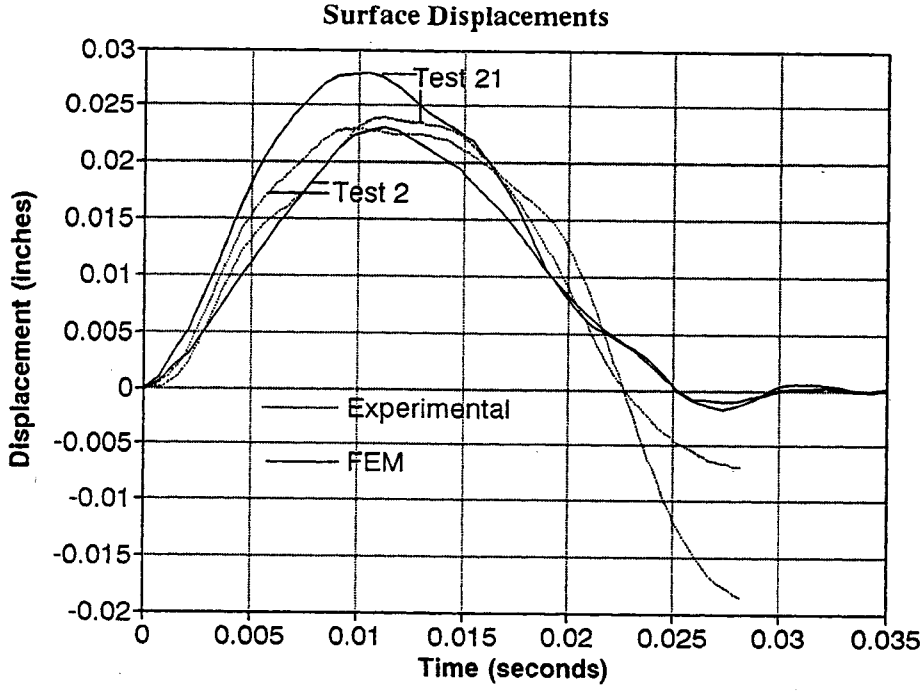

Figure 6.23. Comparison of experimental and numerical surface displacements for Tests 2 and 21.

FEM results are listed for each depth. For the sake of comparison a static Boussinesq distribution is given also. These results are plotted in Figure 6.26 along with the result from the BEM computation.

Table 6.2. Summary of dynamic registration results from dynamic experiments and analyses.

Depth (in.)	Experimental Dynamic Registration	FEM Dynamic Registration	Bouss. Static Registration
3.5	0.97	0.81	0.72
6.3	0.46	-	0.40
9.3	-	0.36	0.23

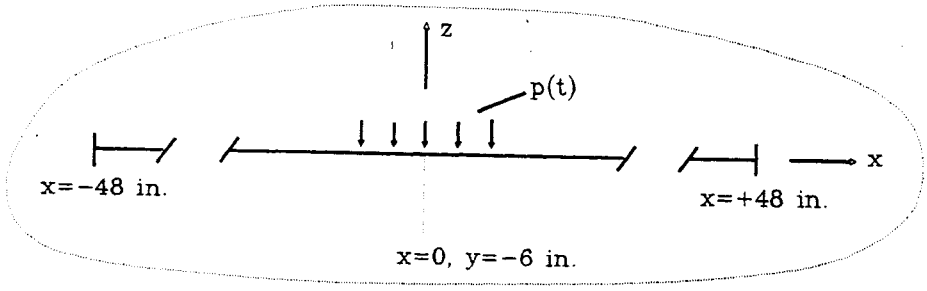

Figure 6.24. Problem geometry for dynamic BEM analysis.

Discussion

Results from the series of dynamic loading tests, when compared to the results of the numerical analyses, have appeared to yield satisfactory results. Referring to Figure 6.26, it appears that the same variability in cell performance observed in the static tests is present in the dynamic results. The primary difference between the static and dynamic testing conditions lies in the effect of the boundary conditions imposed by the testing system. However, random errors due to installation are presumably still present.

Several things need to be considered. With any dynamic FEM model it is usually necessary to calibrate the model and select the proper damping coefficients for boundary conditions. Such an analysis has not been performed for this case but **MNROAD** has been shown to provide reasonable results when applied to an actual pavement structure in modelling dynamic FWD loading [39] when viscous boundaries are specified. The actual damping coefficients used in this analysis were obtained through an optimization process in research

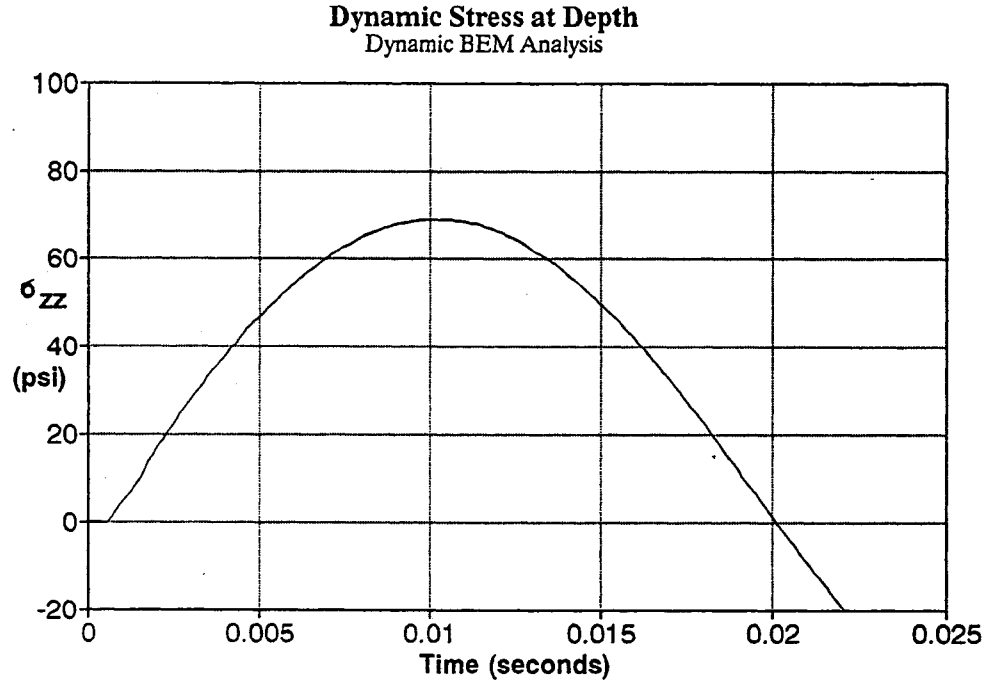

Figure 6.25. Vertical stress σ_{zz} as a function of time at a 6 inch depth: dynamic BEM solution.

performed elsewhere [42]. Another problem may be the finite domain modelled in the analysis. Even with the viscous boundaries all of the energy will not be absorbed and may lead to errors. Another consideration is that the FEM analysis is an approximation to the solution. The primary factor that may affect the experimental results is installation procedures. Results from the static loading experiments presented in this chapter and results given by Hadala [31] indicate that installation procedures alone can account for much of the variability in the results. The experiment compared with the FEM analysis is only one experiment and had other experiments been compared better agreement may have been obtained.

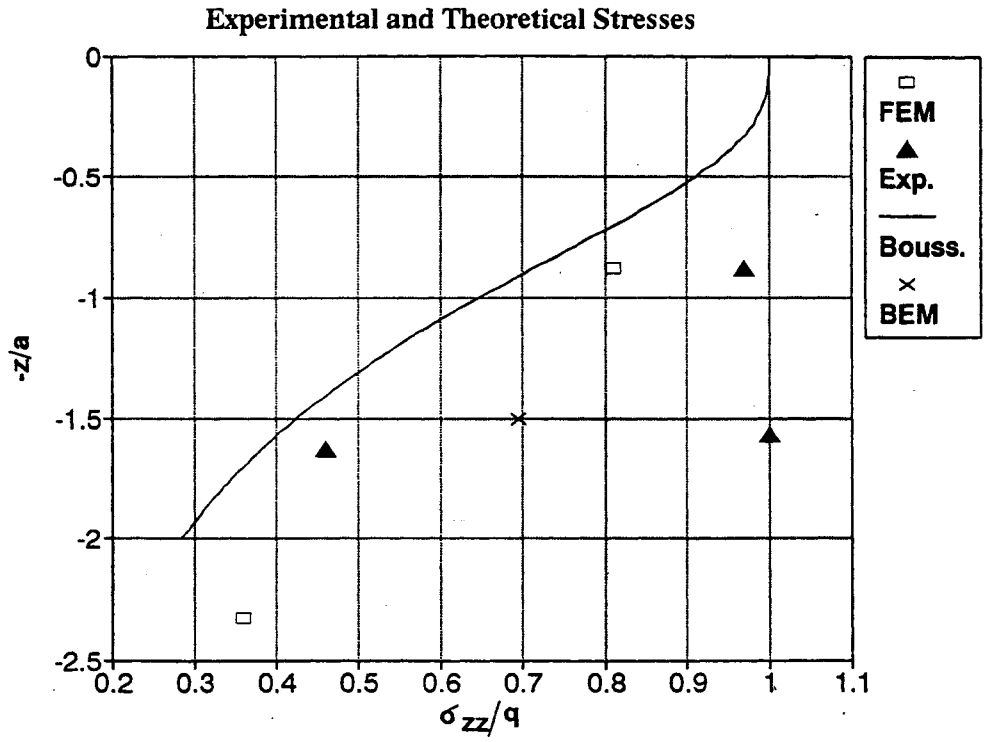

Figure 6.26. Distribution of dynamic experimental and numerical analysis registration ratios.

CHAPTER 7
CONCLUSIONS AND RECOMMENDATIONS

CONCLUSIONS

The following conclusions are based upon information found in the literature and the results of the laboratory evaluation of selected instruments.

Strain Gages

- Factors which affect the general performance of strain gages are the long-term serviceability, the measurement accuracy and the repeatability.
- Strain gages may be applied directly in the field prior to paving, embedded in laboratory prepared material for field placement, or retrofitted in the pavement after construction.
- The design of a pavement strain gage must balance compliance and measurement sensitivity with the need for durability.
- Strain gages should be installed during pavement construction, rather than being retrofitted in order provide better conformance to the surrounding material.
- Dynatest strain gages installed by Mn/DOT in 1987 on T.H. 36 were still functioning and producing reasonable results after three years.
- Dynatest strain gages tested in this study showed considerably greater stiffness than the manufacturer's data.
- Strain gage measurements on steel and concrete beams using Kyowa, Dynatest, and Micro-Measurements strain gages compared favorably to the strain computed from elastic theory.
- The Tokyo Sokki PML-60 gage accurately monitored strain in an uniaxial compression test of a concrete cylinder.
- The Kyowa KM-120 strain gage maintained its gage resistance after three months of freeze-thaw cycling.

Displacement Measurement

o Displacement measurements can be obtained using linear variable differential transformers, velocity transducers, or accelerometers.

o AC LVDTs should be more durable and smaller than DC LVDTs, however they require signal conditioning external to the sensor.

o In-situ pavement deflectometers may be either single-layer or multi-depth in configuration.

o Single-layer deflectometers are simpler to design and install than MDDs, but the measurement is constrained to a single reference point.

o Geophones are practical for deflection measurement only at or near the pavement surface. Furthermore, they do not allow for the measurement of permanent deformation.

o Care must be taken in the design of MDDs to ensure that the material is compliant with the surrounding soil while being rigid enough to prevent cave-ins.

o A Schaevitz HPA-250 LVDT frozen in water for 24 hours showed no change in scale factor after calibration.

o Laboratory results show that the Schaevitz DC LVDT is as robust as its AC counterpart.

Stress Cells

o The two types of embedment stress cells are diaphragm and hydraulic cells.

o The registration ratio of a pressure cell is dependent upon its aspect ratio and the gage to soil modular ratio.

o The deflection at the center of a pressure cell should be no more than 1/5,000 of its diameter.

o The active face of a pressure cell should be 10 to 50 times greater than the mean soil particle size.

o Temperature compensation factors for hydraulic pressure cells should be developed during calibration.

o Great care must be taken during the compaction of soil around pressure gages.

Over-compaction will result in over-registration, while under-compaction will have the opposite result.

- Laboratory testing of stress cells showed that the current linear elastic indentation analogy on stress cell behavior is inadequate and needs to be modified to account for soil friction and non-linearity.
- Dynamic testing showed a linear relationship between applied stress and measured stress levels.
- Variability in pressure cell performance was present in both static and dynamic test results.
- Results from dynamic loading tests compared well with the results of finite element and boundary element analyses.
- The primary factor affecting the experimental results of the pressure cells was the installation procedure.

RECOMMENDATIONS

The following recommendations apply to pavement response sensors proposed for the Minnesota Road Research Project.

- The lead-wires on any sensor should not contain a splice at any point between the gage and the first connection point.
- When using quarter-bridge in and strain gage applications the three lead-wire arrangement should be used to compensate for temperature effects on changes in lead-wire resistance.
- The length of a pavement strain gage should be 4 to 5 times the maximum aggregate size.
- Retrofit strain gages should not be used except in instances of failure for large numbers of strain gages.
- Single-layer deflectometers should be used at Mn/ROAD because of the simplicity of installation and the ease of LVDT retrieval.
- Hermetically sealed DC LVDTs should be used in Mn/ROAD.
- It is desirable to maintain a high gage to soil modular ratio and to minimize the

aspect ratio of a pressure cell.

- The active face of any pressure cell used at Mn/ROAD should be 10 to 50 times greater than the mean soil particle size surrounding it.
- The simplest possible placement procedures should be used in the field in order to reduce inconsistencies in the results.

REFERENCES

1. Sebaaly, P., Tabatabaee, N., and Scullion, T., "Instrumentation for Flexible Pavements," Interim Report for FHWA Contract KTFH61-88-R00052, October, 1988.

2. Dunnicliff, J., Geotechnical Instrumentation for Monitoring Field Performance, John Wiley & Sons, New York, 1988.

3. Micro-Measurements Division, Catalog 500 Part B-Strain Gage Technical Data, Measurements Group, Micro-Measurements Division, 1988.

4. Bordes, J. L., and Debreuille, P. J., "Some Facts About Long-term Reliability of Vibrating Wire Instruments," Transportation Research Record, No. 1004, 1985.

5. Organisation for Economic Cooperation and Development, Strain Measurements in Bituminous Layers, Paris 1985.

6. Dynatest Consulting, Inc., Precision Transducers for Measuring Strain and Stress in Pavements, 1988.

7. Huhtala, M., Alkio, R., Pihlajamaki, J., Pienimaki, M, and Halonen, P., "Behavior of Bituminous Materials Under Moving Wheel Loads," Proceedings, Annual Meeting of the Association of Asphalt Paving Technologists, Albuquerque, New Mexico, 1990.

8. Christison, T. J., personal conversation, 1990.

9. Micro-Measurements Division, Shunt Calibration of Strain Gage Instrumentation, Measurements Group, Micro-Measurements Division, 1988.

10. Micro-Measurements Division, Optimizing Strain Gage Excitation Levels, Tech-Note TN-502, Measurements Group, Micro-Measurements Division, 1988.

11. Omega Engineering, Inc., Pressure Strain and Force Measurement Handbook and Encyclopedia, Stamford, Connecticut, Col. 26, 1988.

12. Bush, A. J., personal conversation, 1989.

13. Scullion, T., Uzan, J., Yazdani, J. I., and Chan, P., "Field Evaluation of the Multi-Depth Deflectometers," Texas Transportation Institute Report 1123-2, 1988.

14. Bush, A. J., "Dynamic Surface Deflection Measurements on Rigid Pavements Compared with the Model of an Infinite Plate on an Elastic Foundation," Transportation Research Record, No. 756.

15. Maree, J. H., Van Zyl, N. J. W., and Freeme, C. R., "Effective Moduli and Stress Dependence of Pavement Materials as Measured in Some Heavy-Vehicle Simulator Tests," Transportation Research Record, No. 852.

16. Nazarian, S., and Bush, A. J., "Determination of Deflection of Pavement Systems Using Velocity Transducers," Proceedings, Transportation Research Board, Paper No. 88-389, 1989.

17. Press, W. H., Flannery, B. P., Teukolsky, S. A., Vetterling, W. T., Numerical Recipes, Cambridge University Press, Cambridge, 1989.

18. Mark Products, Inc., Houston, Texas.

19. Horn, W. J., and Ledbetter, R. H., "Pavement Response to Aircraft Dynamic Loads," Technical Report S-75-11, Vol. 1, U.S. Army Corps of Engineers Waterways Experiment Station, Vicksburg, Mississippi, 1975.

20. Cable, J. K., Klaiber, F. W., and Lee, D. Y., "Pavement Instrumentation," Interim Report for FHWA Contract DTFH71-86-621-IA-19, 1988.

21. Hvorslev, M. J., "The Changeable Interaction Between Soils and Pressure Cells; Tests and Reviews at the Waterways Experiment Station," Technical Report S-767, U. S. Army Waterways Experiment Station, Vicksburg, Mississippi, 1976.

22. Selig, E. T., "In Situ Stress Measurements," Proceedings, Conference on State of the Art of Pavement Response Monitoring Systems for Roads and Airfields, U. S. Army Cold Regions Research and Engineering Laboratory, Hanover, New Hampshire, 1989.

23. Weiler, W. A., and Kulhawy, F. H., "Factors Affecting Stress Cell Measurements in Soil," Journal of the Geotechnical Engineering Division, American Society of Civil Engineers, Vol. 108, No. GT 12, 1982.

24. Ingram, J. K., "The Development of a Free-Field Soil Stress Gage for Static and Dynamic Measurements," Instruments for Soil and Rock Mechanics, STP 392, American Society for Testing and Materials, 1965.

25. Kulite Semiconductor Products, Inc., Bulletin No. KG-1000a, Kulite Semiconductor Products, Inc., Leonia, New Jersey, 1988.

26. Collins, R., Lee, K. J., Lilly, G. P., and Westmann, R. A., "Mechanics of Pressure Cells," Experimental Mechanics, Vol. 12, No. 11, 1972.

27. Eshelby, J. D., "The Determination of the Elastic Field of an Ellipsoidal Inclusion, and Related Problems," Philosophical Transactions of the Royal Society of London, Series A, Vol. 241, 1957.

28. Peattie, K. R., and Sparrow, R. W., "The Fundamental Action of Earth Pressure Cells," Journal of the Mechanics and Physics of Solids, Vol. 2, 1954.

29. Edwards, R. H., "Stress Concentrations Around Spheroidal Inclusions and Cavities," Journal of Applied Mechanics, Vol. 18, 1951.

30. Brown, S. F., "State-of-the-Art Report on Field Instrumentation for Pavement Experiments," Transportation Research Record, No. 640, 1977.

31. Hadala, P. F., "The Effect of Placement Method on the Response of Soil Stress Gages," Technical Report No. 3-803, U. S. Army Engineer Waterways Experiment Station, Vicksburg, Mississippi, 1967.

32. Ahlvin, R. G., "Waterways Experiment Station Large Triaxial Apparatus," Highway Research Board Bulletin 141, 1956.

33. Kohl, K. M., "A Study of the Laboratory and Field Performance of Semiconductor Soil Stress Cell," M.S. Thesis, Cornell University, Ithaca, New York, 1988.

34. Jackura, K. A., and Hannon, J. B., "Measurement of Earth Pressure," Transportation Research Record, No. 1004, 1985.

35. Taylor, D. W., "Review of Pressure Distribution Theories, Earth Pressure Cell Investigations and Pressure Distribution Data," Contract Report W22-053-Eng-185, U.S. Army Engineer Waterways Experiment Station, Vicksburg, Mississippi, 1945.

36. Timoshenko, S., and Goodier, J. N., Theory of Elasticity, 2nd Ed., McGraw-Hill, New York, 1951.

37. Lamb, H., "On the Propagation of Tremors over the Surface of an Elastic Solid," Philosophical Transactions of the Royal Society of London, Ser. A, Vol. 203, 1904.

38. Stam, H. J., "The Two-Dimensional Elastodynamic Distributed Surface Load Problem," Geophysics, Vol. 55, No. 8, 1990.

39. Kuppalli, P., "Development of Simulation Software for Finite Element Modelling of Flexible Pavement Responses," M.S. Thesis, University of Minnesota, Minneapolis, Minnesota, 1990.

40. Holl, D. L., "Stress Transmission in Earths," Proceedings, Highway Research Board, Vol. 20, 1940.

41. Tian, Y., "Boundary Element Methods in Elastodynamics," Ph.D. Dissertation, University of Minnesota, Minneapolis, Minnesota, 1990.

42. Weeks, W., Valliappan, S., Lee, I. C., "Unified Boundary for Finite Dynamic Models," Journal of the Engineering Mechanics Division, American Society of Civil Engineering, Vol. 103, No. 9, 1977.